Physics of Liquid Crystals Embedded in Silica Gels

by

Sungil Park

M.S. Physics
Korea Advanced Institute of Science and Technology (1995)

Submitted to the Department of Physics
in partial fulfillment of the requirements for the degree of

Doctor of Philosophy

at the

MASSACHUSETTS INSTITUTE OF TECHNOLOGY

September 2001

Author . . . .
Department of Physics
Aug 16, 2001

Certified by . . . .
Robert J. Birgeneau
Cecil and Ida Green Professor of Physics
Thesis Supervisor

Accepted by . . . .
Thomas J. Greytak
Professor, Associate Department Head for Education

Physics of Liquid Crystals Embedded in Silica Gels

by

Sungil Park

Submitted to the Department of Physics
on Aug 16, 2001, in partial fulfillment of the
requirements for the degree of
Doctor of Philosophy

Abstract

Octylcyanobiphenyl (8CB) embedded in silica aerosil gels have been studied by means of high resolution X-ray scattering experiments. The silica particles form a hydrogen-bonded fractal gel network that introduces quenched disorder. As a result, the nematic to smectic-A transition is replaced by the growth of static short range smectic correlations. The X-ray scattering profile has two contributions: a thermal fluctuation term which resembles that of the pure liquid crystal and a static fluctuation term due to the random field that becomes important at low temperatures. The decrease of the smectic correlations with increasing silica density is consistent with theory and other experiments.

Thesis Supervisor: Robert J. Birgeneau
Title: Cecil and Ida Green Professor of Physics

Acknowledgments

This thesis, like many other works in science, is a result of the collaboration of many talented scientists supported by devoted staffs, loving families, and sincere friends. It is also because of them, that I am who I am today. Thus, I want to express my gratitude for everything they have done for me.

Firstly, I thank Bob Birgeneau, my research supervisor for the past six years, for allowing me to be part of his wonderful group of scientists. Bob is one of the busiest persons in the world, but amazingly he still finds time to interact with his students. His quick thinking and passion for science allow him to make great contributions to science while he is also building a shining legacy from his administrative work. I learned a great deal from him, not only about science but also from his determination to do "the right thing" as a man. It has been a great pleasure and privilege to know and work with him.

I am greatly indebted to my mentor Carl Garland for his teaching and guidance. His diligence and relentless pursuit of knowledge amazes me. If I become a useful scientist one day, I can certainly say it will be partly because Carl showed me the way of a scientist. His presence was so essential in every aspect of my graduate life at MIT that it is hard to find words that can properly describe my gratitude toward him.

It is only after Bob Leheny joined the group that this research project really took off. His tireless energy shown during early Brookhaven runs is what made it possible to obtain useful data. I thank Bob for all those shared Brookhaven trips, discussions, and for being so patient with me.

Germano Iannacchione is one of the world's leading scientists on liquid crystals in confined geometries, and his knowledge has been crucial in allowing me to take this project to its current status. I thank him for the many discussions we had and for the kindness he showed whenever I visited Worcester Polytechnic Institute.

Jean-Louis Gallani initiated this research while he was a visiting scientist at MIT several years ago. It is only because of his experimental skills that the essential apparatur for the experiments was created. I am grateful for his involvment in the early stages of this research and for showing me a true French flavor in every aspect of life.

Although it has not been a long time since he joined the group and he did not have any previous background on liquid crystals, Paul Clegg impressed me with his rapid ability to learn and to generate new ideas. I thank Paul for sharing his valuable time with me during the final runs at Brookhaven.

Most of the experiments were conducted using samples that Aleksander Roshi of WPI kindly made for me. I thank him for providing such good quality samples year after year.

If there is someone who is closest to being a Vulcan as portrayed in Star Trek, it is Young Lee, my former officemate. He is *almost* always logical, careful, and modest. Although it is easy to be fooled by his stern-looking face, he is one of the nicest persons I have ever known. He answered so many questions I asked without showing any sign of exasperation. I thank him for being such a nice officemate and also for serving on my thesis committee when I was desperately looking for a substitute member.

It feels just like yesterday when I first met Rebecca Christianson and Yujie Wang soon after I arrived at MIT. Yujie was the first graduate student I talked with at a picnic in Killian court, and Rebecca was often spotted studying alone in an office for new graduate students in Building 13. It was a whim of fate that all three of us joined Bob's group later. Rebecca took care of many chores for the group, for which I am very grateful. I also thank her for being a good role model for young girls like my daughter. Yujie answered many questions regarding random fields and boosted my understanding of that subject. He also expanded my knowledge about China through his detailed descriptions of the country. It has been fun to spend six years together with Rebecca and Yujie, and I thank them for being such good friends.

My life at MIT would never have been easy without other members of the group. My former officemate, Martin Greven, always made the place cheerful, which reminds me that Patrick Mang was the same sort of cheerful guy and that Martin and Patrick are working together at Stanford. Young-June Kim taught me many of his computer tricks. Boris Khaykovich's advice on my research presentation was crucial in helping me to get a job at NIST. It alway makes me smile when I reflect on those nice chats I had with Suichi Wakimoto drinking beer together. Although we did not share much time, Barry Wells, Michael Young, Joan Harris, and Qiang Feng were valuable allies when I was struggling to survive during my early years at MIT.

What most impressed me at MIT was, in fact, competence of supporting staffs. Although there are many more deserving of my gratitude I especially want to thank Debra Martin, Karen Fosher, and Marybeth Costa for their assistance in many aspects of graduate life.

I thank Steve LaMarra for all the help he has gave me at Brookhaven. Even when he was awakened by phone calls around midnight, he did not complain at all and always came up with solutions to the problems I was facing at the beamline.

Jean Jordan-Sweet has been a valuable ally at Brookhaven. I thank her for doing many chores for us at the beamline, and for her unforgettable speech in front of the local congressman's office.

I am keenly aware that Ben Ocko's previous experiments on pure 8CB were vital to this research. In addition, I thank him for his valuable input given to me during brief discussions at Brookhaven, in Toronto, and in Seattle.

I thank my wife and my parents and brothers and sisters for all the support they provided during the past six years. Their unconditional love made possible to become what I am today, and I am very grateful to them.

If it were not for the great love and understanding of my wife, Jungsun, and my daughter, Qudan, it would have been impossible to pursue this research for such a long time. They had to endure very many days, evenings, and nights without me, forever waiting my return from work. For that I am greatly indebted to them, and thank them from the bottom of my heart.

Lastly, I thank God for the wonderful world He created rich in physics.

Contents

1 Introduction **17**

1.1 Liquid Crystals 19

1.1.1 Nematics 20

1.1.2 Smectics 22

1.2 Aerogels and Aerosils 23

1.3 X-ray Scattering 25

2 Theoretical Approaches to Liquid Crystals Embedded in Silica Gels **29**

2.1 Nematic to Smectic A Transition 29

2.2 Random Field Models 31

2.2.1 Random Field Ising Model 31

2.2.2 Random Field XY Model 33

2.3 Random Field Theories 34

2.3.1 Imry-Ma Domain-Wall Argument 34

2.3.2 Radzihovsky-Toner Theory 37

3 Prior Experimental Results **41**

3.1 LC + Aerogels 41

3.1.1 Calorimetry 41

3.1.2 Light Scattering 42

3.1.3 X-ray Scattering 42

3.1.4 NMR 43

3.2 LC + Aerosils 45

3.2.1 Calorimetry 45
3.2.2 Other Experiments 47

4 Experimental Techniques 49

4.1 Sample Preparation 49
4.2 Synchrotron X-ray Scattering 50
4.2.1 Synchrotron Radiation 50
4.2.2 X-ray Optics 52
4.3 Sample Environment 55
4.4 Measurements 56

5 Destruction of The Smectic Quasi-Long Range Order 63

5.1 Introduction 63
5.2 Background 64
5.3 Wider-Than-Resolution Widths 66
5.4 Method of Analysis 68
5.4.1 High Temperature Line Shape 68
5.4.2 Low Temperature Line Shape 71
5.4.3 Powder Averaging 73
5.4.4 Convolution With Resolution 74
5.4.5 Employing Bulk Result 74
5.4.6 Fit Results 77

6 Effect of Aerosil Random Disorder 91

6.1 Finite Correlation Lengths 91
6.2 Crossover From Tricritical To 3D-XY Behavior 98
6.3 X-ray Absorption and Normalization of Fit Parameters 101

7 Concluding Remarks 107

A Tables of Results 111

B Powder Averaging 119

B.1 Powder Average 119

B.1.1 Intrinsic Line Shapes 119

B.1.2 Exact Calculation 120

B.1.3 Approximate Calculation 124

List of Figures

1-1 Molecular Structure of Octylcyanobiphenyl (8CB) and Its Phase Sequence . . . 20
1-2 Schematic Diagram of The Structure For Isotropic And Several Liquid Crystal Phases . . . 21

2-1 Imry-Ma Domain Wall Argument . . . 36

4-1 Powder Ring . . . 51
4-2 Scattering Geometry . . . 53
4-3 Sample Environment . . . 56
4-4 Raw Data . . . 58
4-5 Resolution Function For Powder Diffraction Geometry . . . 60
4-6 Resolution Function . . . 61

5-1 High Temperature ($T > T_{NI}$) Scans . . . 65
5-2 Wider-Than-Resolution Widths . . . 67
5-3 Comparison of Bulk 8CB and 8CB + Aerosil Line Shapes . . . 70
5-4 Momentum Space Representation of Mono-domain and Powder Samples 73
5-5 Critical Behavior of Bulk Single-Domain 8CB . . . 76
5-6 Simulated Bulk 8CB Line Shape . . . 78
5-7 $\bar{8}$S5 and $\bar{8}$S5 + Aerosil Line Shape . . . 79
5-8 Fitting Curve for $T > T^*$ for $\rho = 0.025$ and 0.040 g/cm^3 Samples . . 80
5-9 Fitting Curve for $T > T^*$ for $\rho = 0.075$ and 0.200 g/cm^3 Samples . . 81
5-10 Fitting Curve for $T < T^*$ for $\rho = 0.025$ g/cm^3 Sample . . . 82

5-11 Fitting Curve for $T < T^*$ for $\rho = 0.040$ g/cm^3 Sample 83
5-12 Fitting Curve for $T < T^*$ for $\rho = 0.075$ g/cm^3 Sample 84
5-13 Fitting Curve for $T < T^*$ for $\rho = 0.200$ g/cm^3 Sample 85
5-14 Fits of a_2 86
5-15 Temperature Dependence of q_0 88
5-16 Behavior of σ_1 89
5-17 χ^2 Surface 90

6-1 Development of $\xi_{\|}$ 92
6-2 Development of Correlation Length 93
6-3 High Temperature ($T > T^*$) Correlation Length 94
6-4 Low Temperature Correlation Lengths vs Silica Density 96
6-5 $\xi_{\|}^{LT}/l_0$ 97
6-6 Effective Critical Exponent, x 99
6-7 a_S/a_{LC} vs. $\Phi_{\mathrm{SiO_2}}/\Phi_{\mathrm{LC}}$ 103
6-8 σ_1^N vs. T 104
6-9 Normalized σ_1 105

List of Tables

1.1 Symbols common to aerogels and aerosils 24

A.1 Table of ρ, ρ_S, $\Phi_{\mathrm{SiO_2}}$, and the X-ray attenuation length λ. 112
A.2 Best Choices for the Constant Low-Temperature Amplitudes of the LC Terms 112
A.3 $\rho = 0.025$ g/cm^3 113
A.4 $\rho = 0.040$ g/cm^3 113
A.5 $\rho = 0.050$ g/cm^3 114
A.6 $\rho = 0.075$ g/cm^3 114
A.7 $\rho = 0.100$ g/cm^3 data from two runs 115
A.8 $\rho = 0.150$ g/cm^3 116
A.9 $\rho = 0.200$ g/cm^3 116
A.10 $\rho = 0.250$ g/cm^3 117
A.11 $\rho = 0.295$ g/cm^3 117

Chapter 1

Introduction

One of the most dramatic observations in macroscopic systems is the behavior associated with phase transitions. Although the fundamental physical laws governing the behavior of individual molecules are quite well known, it is almost impossible to understand the collective phenomena through the application of those laws alone. It is only through statistical mechanics which often deals with Avogadro's number of molecules that physicists have achieved an understanding of phase transitions.

Liquid crystals have very rich and interesting phase transitional behavior. Since many of the liquid crystalline phases possess positional order, X-ray scattering techniques that probe the instantaneous positional correlations have been an effective tool to investigate liquid crystal phase transitions. Although it is far from complete, the understanding of these transitions has been greatly improved through a series of high-resolution experiments performed since the early 1980's.

Unlike ideal systems, the real world is full of imperfections, and phase transitions can be influenced by random disorder. Studying the effect of such randomness on various phase transitions has been a very challenging task both theoretically and experimentally. The investigation of random field magnets, following Fishman and Aharony's discovery of the generation of random fields in 1979 that random fields can be generated by applying a unform external field to diluted antiferromagnets [1], provided a very good test case for random field theories and was a great boost for the understanding of such systems. Because liquid crystals have many interesting phase transitions, some of which differ in character from those in magnets, applying random disorder to liquid crystals has been given much attention. For example, liquid crystalline molecules within random aerogel networks have been studied with several different methods including calorimetry, light scattering, and X-ray scattering [2-7]. More recently, LC + aerosil systems have attracted much attention [8-15] , and this work has stimulated the present thesis research.

Unlike the LC + aerogel systems, where the aerogel network is rigid and elastically quite stiff, LC + aerosil systems created by dispersing small silica aerosil particles in a liquid crystal possess a soft weakly hydrogen-bonded gel structure. Two advantages can be achieved - elastic smearing of the phase transitions (which occurs for aerogels) is greatly reduced, and very high porosities (very low gel densities) can be realized. The ability to achieve very low levels of disorder is especially important since a different phase transitional behavior may be observed compared with that seen in higher density aerosil samples and rigid aerogels. Therefore, it is attractive to study LC + aerosil systems carefully with X-rays, and the results of such a study are presented in this thesis.

The thesis is divided into six chapters. It is the author's intention to make the thesis as self-contained as possible. To that end, this chapter introduces such basic building blocks of the system, specifically, liquid crystals and aerosils as well as the basics of X-ray scattering. Chapter 2 presents a theoretical overview of the phase transitions involved in this study with or without random disorder. Chapter 3 reviews previous experimental results from a number of different random field systems. The experimental X-ray procedures used in the present work are presented in chapter 4. In chapter 5, the experimental results, the method of data analysis, and the results of this analysis are discussed. Results of the analysis are discussed in chapter 6. In the final chapter the most important results of this study are summarized.

1.1 Liquid Crystals

Contrary to the traditional belief that there are only three states of matter, namely gases, liquids, and solids, there exist a number of phases with properties intermediate between those of an isotropic liquid and a crystalline solid phase. The term liquid crystal was coined to signify systems with such states. Liquid crystalline phases are also called mesomorphic phases, which is often considered as a more appropriate term, and the molecules that show mesomorphic phases are referred to as mesogens.

Several tens of thousands of mesogens are now known to show one or more than one of these mesomorphic phases. Although there are many different mesomorphic phases corresponding to different degrees of order, most materials exhibit only a few such phases. Interestingly, many liquid crystal molecules have several features in common. One of the most important of these features is the fact that all mesogens possess an anisotropic molecular geometry. They are usually either rod-shaped or disk-like. The rod shaped molecules have a rigid central core with extended aliphatic (hydrocarbon) tails, while disk-like molecules have a rigid planar core at the center. The liquid crystal material studied in this thesis is octylcyanobiphenyl (8CB), and its molecular structure is shown in Figure 1-1(a).

Liquid crystals are usually classified as either thermotropic or lyotropic. Thermotropic liquid crystals show different phases as the temperature is changed. Lyotropic liquid crystals, which are usually a mixture of different materials, e.g., liquid crystal molecules and solvent, exhibit phase transitions as the density of the components as well as the temperature is changed. 8CB is a thermotropic liquid crystal, and its phase sequence is shown in Figure 1.1.

There are many mesomorphic phases with various degrees of order. Discussion in this thesis is, however, confined to the two most common mesomorphic phases – nematic and smectic-A, which lie between the isotropic (I) liquid and crystalline solid (K) phases. Since 8CB exhibits both nematic (N) and smectic-A (SmA) phases before it crystallizes upon decreasing temperature from the isotropic phase, a brief introduction to nematics and smectics is given below.

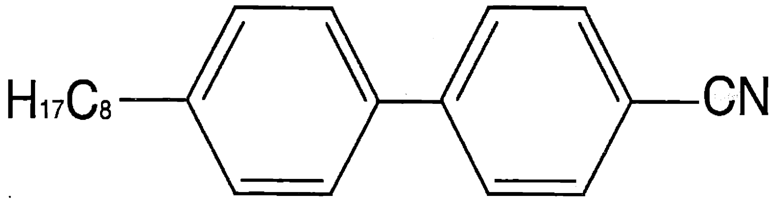

(a) Octylcyanobiphenyl (8CB)

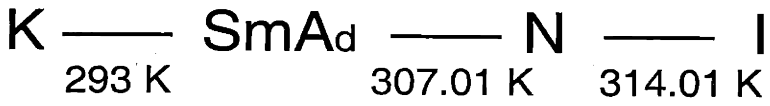

(b) 8CB Phase Sequence

Figure 1-1: Molecular Structure of Octylcyanobiphenyl (8CB) and Its Phase Sequence (a) 8CB has a rigid core and a hydrocarbon tail at one end. (b) With decreasing temperature, 8CB goes through a first order transition from isotropic (I) to nematic (N) phase, a second order phase transition from nematic to smectic-A_d phase, and a first order phase transition to a solid crystalline (K) phase.

1.1.1 Nematics

The name nematic was invented by G. Friedel from the Greek $\nu\eta\mu\alpha$ meaning thread because certain thread-like defects (disclination lines) are often observed in these materials [16]. Figure 1-2(b) shows a schematic arrangement of the molecules in the nematic phase made up of rod-like molecules.

What distinguishes the nematic phase from the isotropic liquid phase is the orientational order, that is, the direction - the long axis - of the molecules tend to align along some common axis, which is represented by the unit vector $\mathbf{n}$ and denoted as the 'director'. Note that the $-\mathbf{n}$ state is indistinguishable from the $+\mathbf{n}$ state.

Except for the orientational order described above, many other aspects of the nematic phase are similar to those of the isotropic liquid phase. The centers of mass of the molecules are random, and nematics flow like liquids.

A scalar order parameter for the nematic phase can be written as

$$Q = -\frac{1}{2} + \frac{3}{2}\left\langle \cos^2\theta \right\rangle . \tag{1.1}$$

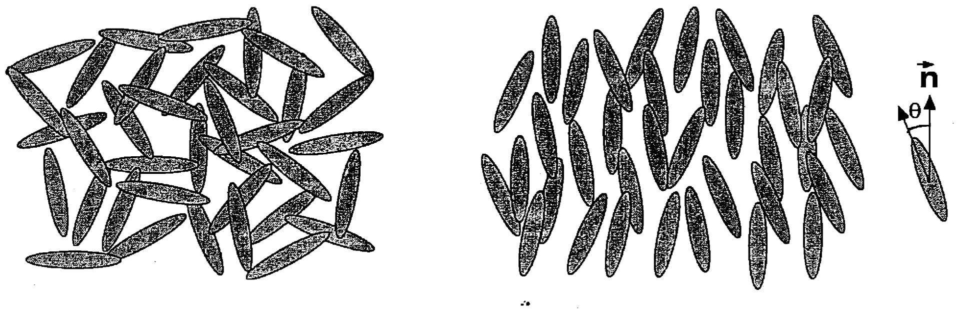

(a) isotropic phase

(b) nematic phase

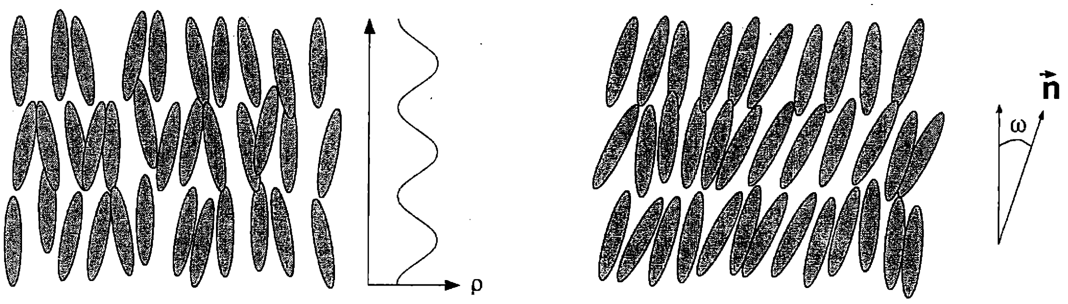

(c) smectic A

(d) smectic C

Figure 1-2: Schematic Diagram of The Structure For Isotropic And Several Liquid Crystal Phases

It is interesting to note that Q varies from -1/2 to 1 where -1/2 corresponds to a state in which all the molecules are aligned perpendicular to the director. This is not a stable state. When the molecules are randomly oriented, Q becomes 0, and when the molecules are perfectly aligned parallel to the director, Q becomes 1.

The nematic states involves a free energy of deformation that can be expressed as

$$F_N = \frac{K_s}{2}(\nabla \cdot \mathbf{n})^2 + \frac{K_t}{2}(\mathbf{n} \cdot \nabla \times \mathbf{n})^2 + \frac{K_b}{2}(\mathbf{n} \times \nabla \times \mathbf{n})^2, \tag{1.2}$$

where K_s, K_t, and K_b are respectively the splay, twist, and bend elastic constants corresponding to the elastic deformations of the same name.

1.1.2 Smectics

The name smectic was coined by G. Friedel from the Greek word $\sigma\mu\eta\gamma\mu\alpha$ meaning soap because the mechanical properties are reminiscent of soaps[16]. Smectics in general have layered structures with a well-defined interlayer spacing, which can be probed by X-ray diffraction.

The simplest smectic phase, the smectic-A phase, is illustrated in Figure 1-2(c). A smectic-A phase corresponds to a one-dimensional density wave in a three-dimensional fluid with the density wave along the nematic director. In fact, the density modulation is almost perfectly sinusoidal so that the density of the system in the smectic-A phase can be written as

$$\rho(z) = \rho_0 + |\Psi| \cos\left(\frac{2\pi z}{d} + \varphi\right), \tag{1.3}$$

where ρ_0 is the average density, $|\Psi|$ is the amplitude of the modulation, and d is the layer spacing. In the above density equation for the smectic-A phase, the higher order terms, which are typically several orders of magnitude smaller than the first order term, can be safely ignored. The 8CB layer spacing is $d = 31.73$ Å.

Strictly speaking, the smectic-A phase of 8CB is a smectic-A$_\mathrm{d}$ phase, which is a partial bilayer smectic since d has a value between L and $2L$ where L is the extended length of a single 8CB molecule.

1.2 Aerogels and Aerosils

Since they were first invented in 1931 [17], aerogels have been proved to be very useful in various applications as well as scientific research. The term "aerogel" was coined by its inventor Samuel S. Kistler. Though there are many different materials that can make aerogels, for example, alumina, tungsten oxide, ferric oxide, tin oxide, etc., silica aerogels are a focus of discussion in this thesis, thus silica aerogels are implied by aerogels unless stated otherwise. For an excellent review of silica aerogels, refer to the silica aerogels web site at Lawrence Berkeley National Laboratory[18].

Aerogels were invented in an effort to demonstrate that a wet gel contained a solid network of the same size and shape as the gel itself. Removing the liquid from the gel without damaging the solid network was achieved by drying at supercritical temperatures and pressures to avoid the formation of a solvent liquid-vapor interface with attendant surface tension forces that can severely distort the gel. The fabrication process has improved greatly since the days of Kistler, and now it typically utilizes silicon alkoxide precursors to produce aerogels. Tetramethyl orthosilicate (TMOS, $Si(OCH_3)_4$) and tetraethyl orthosilicate (TEOS, $Si(OCH_2CH_3)_4$) are the popular reagents these days. When TEOS is used, the balanced chemical equation for the formation of a silica gel is:

$$Si(OCH_2CH_3)_4 + 2H_2O = SiO_2 + 4HOCH_2CH_3 \tag{1.4}$$

The reaction occurs in a solvent, e.g., alcohol, and the final density of the aerogel depends on the concentration of silicon alkoxide monomers in the solution. The remaining water is removed by soaking the gel in the solvent several times, and finally the solvent is dried at supercritical temperature and pressure in an autoclave.

The final product, silica aerogel, thus obtained is semi-transparent, low density, and highly porous. It is believed that silica aerogels consist of a random network of silica backbones in an openly connected void space. Small-angle X-ray scattering (SAXS) results show that aerogels are fractal over a limited range in length scales[19-23].

Table 1.1: Symbols common to aerogels and aerosils

Symbol	Meaning	Definition
m_{LC}	total mass of the LC	
$m_{\mathrm{SiO_2}}$	total mass of the silica	
m_{total}	total mass of the sample	$m_{\mathrm{LC}} + m_{\mathrm{SiO_2}}$
V_{LC}	total volume occupied by the LC	
$V_{\mathrm{SiO_2}}$	total volume occupied by the silica	
V_{total}	total volume of the sample	$V_{\mathrm{LC}} + V_{\mathrm{SiO_2}}$
ρ_{total}	the total density of the LC+aerosil sample	$m_{\mathrm{total}}/V_{\mathrm{total}}$
ρ	the silica mass density of the LC+aerosil sample	$m_{\mathrm{SiO_2}}/V_{\mathrm{total}}$
$\rho_{\mathrm{SiO_2}}$	the pure silica density ($\sim 2.2\mathrm{g/cm^3}$)	$m_{\mathrm{SiO_2}}/V_{\mathrm{SiO_2}}$
ρ_{S}	silica mass density per unit LC volume	$m_{\mathrm{SiO_2}}/V_{\mathrm{LC}}$
$\Phi_{\mathrm{LC}} \equiv \phi_P$	pore volume fraction	$V_{\mathrm{LC}}/V_{\mathrm{total}}$
$\Phi_{\mathrm{SiO_2}}$	silica volume fraction	$V_{\mathrm{SiO_2}}/V_{\mathrm{total}}$

Although the preparation method is greatly different, the aerosils form gels that are chemically identical and structurally similar to the aerogels. A detailed description of making LC + aerosil samples is located in the sample preparation section in this thesis. Unlike the aerogels where silica particles are fused together, the aerosil gels are made of silica spheres attached to each other through rather weak hydrogen bonds. The presence of hydroxyl groups on the surface of the silica is what causes the aerosils to form a thixotropic gel when dispersed in an organic medium. The aerosil gels are believed to have a fractal network of silica backbones as do the aerogels. One of the important differences between the aerosil gels and the rigid aerogels is, however, that the aerosils cannot maintain their structure by themselves. Thus the preparation of aerosil gels always involve mixing the silica particles and the dispersing agent, e.g., the liquid crystal.

For both aerogels and aerosils there are quite a few frequently used common symbols. They are listed in table 1.1 for convenience.

Because the sum of the silica and the LC volume fraction must be 1, we can easily deduce the following equations from the definitions given in the table:

$$\frac{1}{\rho} = \frac{1}{\rho_{\mathrm{S}}} + \frac{1}{\rho_{\mathrm{SiO_2}}} \tag{1.5}$$

$$\Phi_{\mathrm{LC}} = \frac{\rho}{\rho_{\mathrm{S}}} \tag{1.6}$$

$$\Phi_{\mathrm{SiO_2}} = \frac{\rho}{\rho_{\mathrm{SiO_2}}} \tag{1.7}$$

Equation 1.5 is handy when it is needed to convert one type of density into another.

Finally it should be noted that liquid crystal orientational and positional order is modified through surface anchoring in the presence of a silica surface. A cyanobiphenyl liquid crystal like 8CB, due to its polar nature, is expected to have homeotropic anchoring (alignment of the liquid crystal molecules with their long axes perpendicular to the boundary surface) at a $\mathrm{SiO_2}$ surface covered with –OH surface groups [1] [24].

1.3 X-ray Scattering

X-ray scattering is a very useful tool for probing the structures of matter because the wavelengths associated with the photons are of the order of Angstroms, matching typical lattice spacings of many condensed matter systems. Since smectic phases of liquid crystals are fundamentally density waves and have "layer spacing" of the order of tens of Angstroms, X-ray scattering has been widely used to probe such smectic phases. A good review of X-ray scattering can be found in Ref.[25].

For any scattering experiment, momentum and energy transfers between an incoming and an outgoing channel must be considered. If the incident photon has momentum $\mathbf{k}_i$ and energy $E_i = hk_ic$ and the scattered photon has momentum $\mathbf{k}_f$ and energy $E_f = hk_fc$, the momentum absorbed by the sample is $\mathbf{q} = \mathbf{k}_i - \mathbf{k}_f$ and the energy transferred is $E_i - E_f$.

For the experiments of concern here, the energy change of the photons is a very small fraction of the original energy (about or less than 10^{-5}). Therefore, we are dealing with quasi-elastic approximation where $E_f \sim E_i, k_f \sim k_i$, and the Bragg

---

[1] Whether the anchoring is homeotropic or planar (alignment of the liquid crystal molecules parallel to the boundary surface) is not agreed upon and is a subject of dispute. It may dependent on the characteristic of individual molecules. We adopted a view that hydrophobic disposition of aliphatic tails cause homeotropic anchoring on a –OH rich surface.

reflection law $q = 2k_i \sin\theta$ can be used as a very good approximation. That is, X-ray scattering can be thought as the radiation from an accelerated charge due to an oscillating electric field, which is the classical Thomson scattering[26].

Quantum mechanical treatment of the scattering process is well described in Ref.[27], and the calculation of the scattering cross-section and the dynamic structure factor can be done with the standard interaction Hamiltonian

$$H = \frac{\mathbf{A}^2}{2mc^2} + \frac{\mathbf{p}\cdot\mathbf{A}}{mc^2}. \tag{1.8}$$

The transition probability between the initial and final states can be calculated through the Born approximation.

$$P_{i\to f} = \frac{2\pi}{\hbar}\left|\langle \psi_f e^{i\mathbf{k}_f\cdot\mathbf{r}} \left|H\right| \psi_i e^{i\mathbf{k}_i\cdot\mathbf{r}}\rangle\right| \delta\left(E_i - E_f - \hbar\left(\omega_i - \omega_f\right)\right), \tag{1.9}$$

where the initial plane wave state is represented by $\exp(i\mathbf{k}_i\cdot\mathbf{r})$ and the final state by $\exp(i\mathbf{k}_f\cdot\mathbf{r})$.

The resulting dynamic structure factor is

$$S(\mathbf{q},\omega) = \frac{1}{2\pi\hbar}\int \mathrm{d}t\mathrm{d}^3\mathbf{r} e^{i\mathbf{q}\cdot\mathbf{r}-i\omega t}\left\langle \rho(\mathbf{r},t)\rho(0,0)\right\rangle, \tag{1.10}$$

which clearly shows that X-ray directly probes the density-density correlations.

Unfortunately, it is not possible to observe perfect delta-function-shaped Bragg peaks from X-ray scattering. Instead, the line shapes are obscured by many factors and always have non-zero widths, which hinders the analysis, e.g., the extraction of correlation lengths. Among the contributors to the non-zero widths, the finite resolution from the instrument is of central importance.

A perfectly ordered sample of an infinite size would yield a delta function peak with fictitious infinite instrumental resolution.

$$S_{ideal}(\mathbf{q}) \propto \delta(\mathbf{q}) \tag{1.11}$$

In reality, even with a perfect sample, the line shape is broadened due to the effects of finite resolution.

$$S_{real}(\mathbf{q}) \propto \mathrm{Res}(\mathbf{q}) \tag{1.12}$$

where Res($\mathbf{q}$) is the resolution function.

The intrinsic line shape $S_{intrinsic}(\mathbf{q})$ broadens due to the same finite resolution effect. Note first that the line shape is a sum (or integral if you like) of delta functions

$$S_{intrinsic}(\mathbf{q}) = \int d\mathbf{q}'\ S_{intrinsic}(\mathbf{q}')\delta(\mathbf{q} - \mathbf{q}'). \tag{1.13}$$

The observed line shape is obviously

$$S_{observed}(\mathbf{q}) = \int d\mathbf{q}'\ S_{intrinsic}(\mathbf{q}')\mathrm{Res}(\mathbf{q} - \mathbf{q}'), \tag{1.14}$$

or equivalently

$$S_{observed}(\mathbf{q}) = S_{intrinsic}(\mathbf{q}) \otimes \mathrm{Res}(\mathbf{q}) \tag{1.15}$$

which is a convolution of the intrinsic line shape and the resolution function.

Chapter 2

Theoretical Approaches to Liquid Crystals Embedded in Silica Gels

2.1 Nematic to Smectic A Transition

As Aaron Rappaport said in his pioneering X-ray scattering work on 8CB + aerogels [28], an understanding of the bulk nematic to smectic-A transition is vital for the analysis of experiments on aerogel- or aerosil-confined systems. Thus it is appropriate to discuss the nature of the transition at this point.

Although the nematic to smectic-A transition can be identified as a simple one-dimensional freezing, it is not yet completely understood. A good description of the transition can be found in chapter 10 of de Gennes' book [16] and the most up-to-date review of the transition is presented by Garland and Nounesis [29]. In this section, those aspects of the transition relevant to the topic of this thesis will be discussed.

As discussed in Chapter 1, the N to SmA phase transition can be understood as the onset of one dimensional density wave in a three dimensional fluid, as shown in Eq. 1.3. The two parameters of the equation, the amplitude of the density modulation $|\Psi|$ and the phase φ, are the two components of the smectic-A order parameter $\Psi = |\Psi|e^{i\varphi}$. The dimensionality of the order parameter suggests the N-SmA transition should technically belong to the same universality class as the normal–superconducting transition, 3D-XY. This is one reason why the transition has attracted both theoretical and experimental interest.

The de Gennes Hamiltonian that describes the transition in a pure bulk liquid crystal is given by

$$H_{dG}[\psi, \mathbf{n}] = \frac{1}{2}\int d^d r \left[C_\perp \left|(\nabla_\perp - iq_0\delta\mathbf{n})\,\psi\right|^2 + C_\parallel \left|\nabla_\parallel\psi\right|^2 + t_0\left|\psi\right|^2 + \frac{1}{2}b\left|\psi\right|^4\right] + H_F[\mathbf{n}], \tag{2.1}$$

where $t_0 \equiv (T - T_{NA}^{bulk})/T_{NA}^{bulk}$, T_{NA}^{bulk} is the NA transition temperature of the bulk system, $\delta\mathbf{n}(\mathbf{r}) \equiv \mathbf{n}(\mathbf{r} - \mathbf{n}_0)$ is the fluctuation of the local nematic director $\mathbf{n}(\mathbf{r})$ away from its average value $\mathbf{n}_0$, which we take to be $\hat{\mathbf{z}}$, subscripts $\parallel$ and $\perp$ denote the directions parallel and transverse to $\mathbf{n}_0$, and $H_F[\mathbf{n}]$ is the Frank effective Hamiltonian that describes the elasticity of the nematic order director as shown in equation 1.2 [30].

However, the critical exponents for the N-SmA transition of real liquid crystals are not the same as 3D-XY values. For example, while the 3D-XY heat capacity critical exponent is $\alpha_{3D-XY} = -0.007$, 8CB has a noticeably different value of $\alpha \approx 0.31$. More importantly, the 3D-XY model does not account for the anisotropic nature of the correlation length. Specifically, the 3D-XY correlation length critical exponent ν_{3D-XY} is a single value of 0.699, but 8CB has $\nu_\parallel \approx 0.67$ and $\nu_\perp \approx 0.51$. Many other liquid crystals that exhibit N-SmA transitions also have anisotropic correlation length exponents.

In fact, a very thorough compilation of experimentally determined effective critical exponents of various liquid crystals shows quite interesting behavior [29]. The exponents mostly lie between 3D-XY and tricritical values, and the general trend is that the bigger the McMillan ratio ($R_M \equiv T_{NA}/T_{NI}$), the more tricritical-like the exponents, which is in qualitative agreement with what McMillan suggested in his mean-field theory [31].

A crossover from 3D-XY to tricritical nature comes from the coupling between the smectic order parameter Ψ and the nematic orientational order parameter Q. When the nematic range is narrow (large McMillan ratio), the coupling is strong and this drives the $b\Psi^4$ term of the free-energy negative, leading to a first order N-SmA transition via a Gaussian tricritical point.

Patton and Andereck suggest that the deviation from isotropic XY behavior is due to the coupling between director fluctuations $\delta\mathbf{n}$ and the smectic order parameter Ψ, which is intrinsically anisotropic [32, 33]. According to their model, there is a very gradual crossover from isotropic to a broad weakly anisotropic correlation regime followed by strongly anisotropic ($\nu_{\parallel} = 2\nu_{\perp}$) behavior in the strong-coupling limit.

Patton and Andereck's model suggests explanations of the experimental correlation length results for N-SmA transitions at least qualitatively. However, many aspects of the theory, including especially the prediction of very strong anisotropy ($\nu_{\parallel} = 2\nu_{\perp}$) at extremely small reduced temperatures, is beyond the reach of current experimental techniques, and a true test of the Patton-Andereck theory is yet to come.

Very recently, Paul Keyes [34] has developed a rotationally invariant model for the N-SmA transition. This uses the full tensor nematic order parameter, which is coupled to the smectic density gradients. Thus director fluctuations and fluctuations in the magnitude of the nematic ordering are treated on an equal footing. The important predictions of the de Gennes model are preserved, but there are several new results that seem to resolve many of the long-standing puzzles associated with the transition. For example, the model predicts a q^4 term in the transverse part of the X-ray structure factor with a temperature dependence that agrees reasonably well with experiments. Further detailed testing of this model will be of great interest.

2.2 Random Field Models

2.2.1 Random Field Ising Model

The Ising model is one of the simplest order-disorder model systems, and it has been a popular starting point of many theoretical considerations. The Hamiltonian is simply the sum of dot products of nearest-neighbor one-component spins:

$$\mathcal{H} = J \sum_{<ij>} S_i S_j - H \sum_i S_i, \tag{2.2}$$

where J denotes the strength of exchange interaction between spins and H is a uniform external field applied to the system. The system becomes anti-ferromagnetic at low temperatures when $J > 0$ or ferromagnetic when $J < 0$.

The above Hamiltonian can be easily expanded to that of the Random Field Ising Model (RFIM) to include disorder.

$$\mathcal{H} = J \sum_{<ij>} S_i S_j - \sum_i h_i S_i - H \sum_i S_i, \tag{2.3}$$

where h_i is the site random field that satisfies the following condition:

$$< h_i >= 0, < h_i^2 >= h_0^2. \tag{2.4}$$

For our purpose, we will only deal with the case in which the uniform external field is set to zero, $H = 0$.

If the random field is too strong, i.e., when $h_0 \geq |J|$, the low temperature state is a trivial one. Every spin simply follows the respective site random field. Therefore, the interesting case is the limit when $h_0 \ll |J|$, the weak random field limit. The presence of a random field dramatically changes the nature of the transition even in this limit. For example, ordering of the 2-dimensional Ising model, which was solved exactly by Onsager [35], is destroyed by the introduction of any non-zero random field.

Although many theoretical works have centered around the RFIM [36, 37], experimental realization of random field magnetic systems had to wait until Fishmann and Aharony [1] observed that the physics of the RFIM was closely related to the behavior of a random Ising antiferromagnet in a uniform field. Since then, many experimental techniques have been employed, including X-ray and neutron scattering methods, to study the nature of RFIM. These studies revealed that non-equilibrium phenomena played a very important role in 3D RFIM systems, rendering both the experimental and theoretical situation quite complex but very rich in physics.

This non-equilibrium behavior is directly shown by zero field cooling (ZFC) and field cooling (FC) studies of random magnets. In ZFC, the antiferromagnet is cooled down without any applied magnetic field across the phase transition to the antiferromagnetic state. The field is applied at this stage, and the system is heated across the transition again. All measurements in ZFC indicates a sharp transition to a long range order with distinct critical exponents. In FC, a disordering field is applied to the system first, followed by a cooling process within the field. Instead of a sharp transition, the FC procedure yields a metastable frozen domain state, a result dramatically different from that of ZFC procedure.

It is now believed that this disparity of ZFC and FC results is caused by the complex free energy landscape which has numerous local minima. Depending on the initial state, the system can be easily trapped in one of the local energy minima, and the evolution to the true ground state is expected to be extremely slow, perhaps beyond the reach of experimentally observation.

Meanwhile, Imbrie [38] proved that the lower critical dimension of RFIM is two, thus 3D RFIM exhibits long-range order.

2.2.2 Random Field XY Model

A model that is more relevant to the current study is the Random Field XY Model (RFXYM) which is designed to study the role of quenched randomness in systems with a planar (XY) symmetry. It is also useful in understanding the vortex lattice structure observed in type II superconductivity including high-T_C superconductors. The RFXYM Hamiltonian is identical to that of RFIM except that two component spins, $\mathbf{S}$, are used. Thus the Hamiltonian is written as

$$\mathcal{H} = J \sum_{<ij>} \mathbf{S}_i \cdot \mathbf{S}_j - \sum_i \mathbf{h}_i \cdot \mathbf{S}_i - \mathbf{H} \cdot \sum_i \mathbf{S}_i, \tag{2.5}$$

Again we will only deal with systems without any applied uniform field, i.e., $\mathbf{H} = 0$.

It is now believed that there is no long range order in random field XY magnets with quenched disorder in less than four dimensions [36]. The nature of the ground state, however, is not well understood yet. We will deal with those theoretical aspects of RFXYM in the next section.

It must be noted that the LC + aerosil systems differ from the simple RFXYM in a subtle way. In the LC + aerosil systems, the randomness enters through random pinning of molecules and positional disorder due to silica strands. Thus, the disordering field is not randomly distributed in space (as in random magnetic systems) but is distributed along the silica strands. At long length scales, however, the random pinning and positional disorder introduced by the fractal network of silica strands can be considered as a random field like that in the simple model.

2.3 Random Field Theories

The dimensionality of a system is very important in determining whether there is a phase transition and, if so, its critical properties. When the spatial dimension is low, the role of fluctuation becomes important, eventually driving the transition temperature to zero at the lower critical dimension. When the spatial dimension is high, the opposite happens. The high connectivity of a system makes fluctuation less important and eventually mean field theory becomes exact above the upper critical dimension.

For non-random systems, the canonical method for determining the lower critical dimension has been to test the stability of the ordered phase to the creation of differently oriented domains due to fluctuations. This method yields a lower critical dimension of 1 for the Ising model [39].

2.3.1 Imry-Ma Domain-Wall Argument

Imry and Ma [36] used the classical domain wall argument frequently used for determining the stability of an ordered state. With the presence of random field, it is possible to estimate the energy cost of having a domain of spins flipped from a ferromagnetic ground state. If the size of the domain (let us say the radius as shown in figure 2-1) is R, the energy cost comes from the broken bonds on the surface of the domain wall. If it is an Ising system with discrete symmetry, this is simply proportional to the surface area. If it is a continuous symmetry system, the energy cost is optimized by a continuous rotation of the order parameter over a distance comparable to R.

$$\begin{aligned} E_{cost} &\sim JR^{d-1} \text{ if Ising} && (2.6) \\ &\sim JR^{d-2} \text{ if XY.} && (2.7) \end{aligned}$$

This argument immediately shows there is no long range order for $d \leq 2$ for continuous symmetry systems.

The energy cost must be balanced against the energy gain from the random field for the domain to be stable. Simple statistics show that the sum of the random field in a domain fluctuates from one domain to another with typical values being given by $\sim R^{d/2}$. Thus the energy gain is

$$E_{gain} \sim -h_0 R^{d/2}. \tag{2.8}$$

The net energy gain/loss due to the domain formation can be now written as

$$\begin{aligned} E(R) &\sim JR^{d-1} - h_0 R^{d/2} \text{ if Ising} && (2.9) \\ &\sim JR^{d-2} - h_0 R^{d/2} \text{ if XY.} && (2.10) \end{aligned}$$

Therefore, whenever

$$\begin{aligned} \frac{d}{2} &\geq d-1 \text{ if Ising} && (2.11) \\ \frac{d}{2} &\geq d-2 \text{ if XY} && (2.12) \end{aligned}$$

there will be some sufficiently large R for which it will become energetically favorable to have domains of size R even with an arbitrarily small random field, i.e., the lower critical dimensions of RFIM and RFXYM are 2 and 4 respectively. Thus no phase

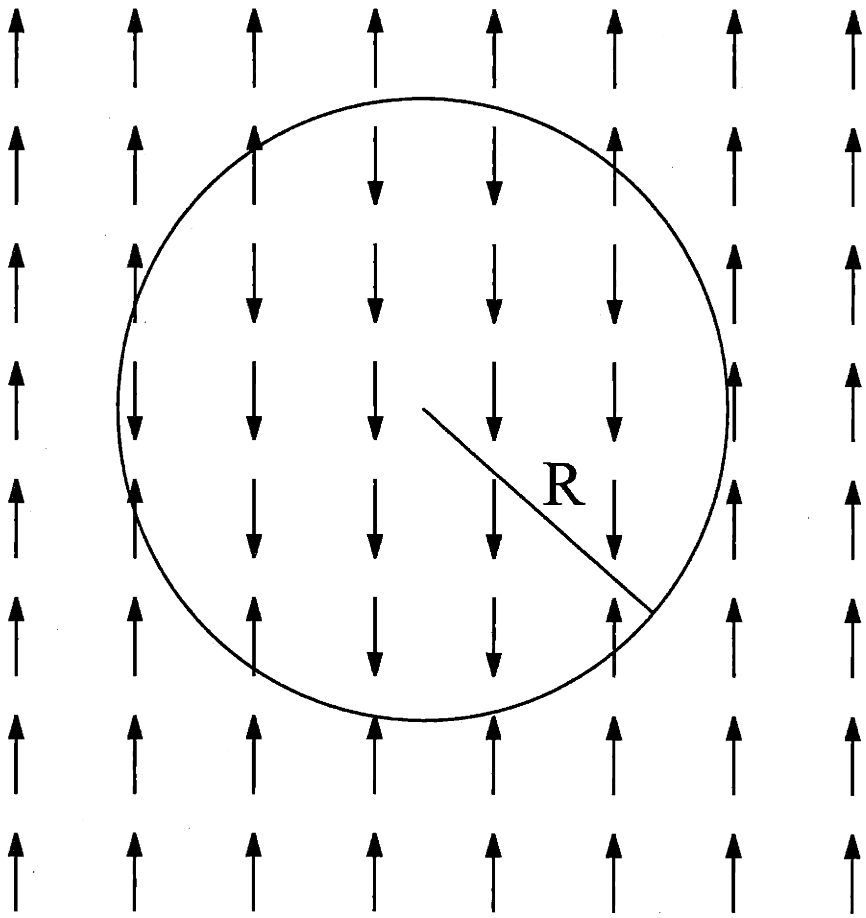

Figure 2-1: Imry-Ma Domain Wall Argument

Imry and Ma [36] assumes smooth domain walls that enclose regions of size (radius) R.

transition to long range order is expected for continuous symmetry systems in 3 dimensions.

The above domain wall argument should not be considered exact due to the following points. Firstly, it is a zero temperature argument without any consideration given to thermal fluctuation or entropic effects. Secondly, only smooth domain walls are considered. Thirdly, domains within domains are not considered.

Aizenman and Wher [40] provided an exact theoretical treatment to prove the non-existence of long range order for continuous symmetry systems in dimensions less than four.

2.3.2 Radzihovsky-Toner Theory

Inspired by "Bragg glass" systems [41], in which an elastically disordered glass is topologically ordered, Radzihovsky and Toner [42, 43, 30] made a major theoretical effort to understand the low temperature behavior of LC + aerogel systems.

In addition to the de Gennes Hamiltonian, the disorder was introduced through the following terms added to the Hamiltonian:

$$F_d = \int d^d r \left[\frac{1}{2}\delta t(\mathbf{r})(\rho - \rho_0)^2 + U(\mathbf{r})\rho + [\mathbf{g}(\mathbf{r}) \cdot \mathbf{n}]^2 \right], \tag{2.13}$$

where $\delta t(\mathbf{r})$ represents the effect of randomness on the shift of T_C, $U(\mathbf{r})$ is a quenched random potential, and $\mathbf{g}(\mathbf{r})$ is a quenched random field. All of the randomness terms introduced above are proportional to the local aerogel density $\rho_A(\mathbf{r})$. The first two terms contribute to the random positional disorder (Δ_V) and the last term, which reflects the proclivity of aerogels for particular orientations of the nematogens, constitutes the random orientational disorder (Δ_h, "tilt" field).

The major findings of the theory are

- the *tilt* disorder dominates the total disorder in the system,
- a three-dimensional smectic phase is unstable to arbitrarily weak quenched disorder, and

- a new orientationally ordered low-temperature "smectic Bragg glass"(SBG) phase replaces the smectic phase under certain conditions, but ϵ-expansion results suggest that the SBG does not exist in three dimensions.

According to the theory, the elastic properties of liquid crystals are significantly modified due to the presence of quenched disorder, which affects both the X-ray scattering line shape and the growth of the correlation length, ξ, as a function of temperature. The elastic constants B and K are found to be functions of wavevector q, $B(q) \sim q^{\eta_B}$ and $K(q) \sim q^{-\eta_K}$, where η_B and η_K are positive definite universal exponents. Theory predicts the nematic to SBG (N-SBG) transition survives if and only if the exponents η_B and η_K satisfy the bounds

$$\eta_K + \eta_B < 2, \tag{2.14}$$

$$\eta_K < 1, \tag{2.15}$$

$$\eta_B + 5\eta_K > 4. \tag{2.16}$$

A $d = 5 - \epsilon$ expansion result indicate that in $d = 3, \eta_B = 12/5$ and $\eta_K = 2/5$, thus the N-SBG transition should not occur.

The theoretical result that is most relevant to the actual X-ray measurements is a correlation length that satisfies the following relation:

$$\xi(\rho_A, T) \sim \Delta_h^{-1} B(T)^{\frac{1}{\Gamma}} \tag{2.17}$$

where $\Gamma \equiv (2/(\eta_B + \eta_K) - 1/2)^{-1}$ is a universal constant, $B(T)$ is effective layer compressional modulus of the pure liquid crystal, and ρ_A enters the right hand side of the above equation through the random tilt field Δ_h. Thus the X-ray correlation length is expected to be approximately inversely proportional to the silica density. Since $B(T)$ is a measurable quantity, see Benzekri *et al.* [44], X-ray scattering techniques can be used to find the exponent $1/\Gamma$, hence $\eta_K + \eta_B$. In addition, X-ray scattering line shape is also expected to be affected by this "anomalous elasticity" from the Lorentzian form, a powder average of the Lorentzian squared, into a generalized

Lorentzian, $I(q) \sim 1/(1 + (\xi\delta q)^{1+\Gamma})$.

A detailed study of the 8CB + aerogel system [7] seems to find $\Gamma \approx 1$, indicating that the smectic Bragg glass phase should be possible in that system. However, for the 8CB + aerosil system, we observe a different behavior for the correlation lengths, which is not well described by equation 2.17. See chapter 6 for a discussion of the dependence of 8CB + aerosil correlation lengths on the density and the temperature. Thus, a comparison of the 8CB + aerosil data with RT theory was not attempted.

Chapter 3

Prior Experimental Results

To understand a complex system such as 8CB + aerosils while the phase behavior of bulk 8CB is itself not yet completely understood is a difficult task. Therefore, it is desirable to use a wide variety of experimental techniques to collect as much information as possible in order to discover the fundamental nature of the system. There have been extensive studies of liquid crystals in various confined media by researchers around the globe over the past few decades. Studies of LC + aerogel systems, due to their similarity to LC + aerosils, are especially able to shed light on the transitions we are interested in. In this chapter the most notable previous experimental results on LC + aerogels and LC + aerosils are reviewed.

3.1 LC + Aerogels

3.1.1 Calorimetry

Detailed ac calorimetry was performed by Wu, Zhou, Garland, Bellini, and Schaefer on $\rho = 0.08, 0.17, 0.36,$ and 0.60 g/cm^3 8CB + aerogel samples [4]. Small angle X-ray scattering showed that these rigid aerogels had average pore chords of $L = 700, 430, 180,$ and 120 Å, respectively, corresponding to pore volume fractions of $\phi_P = 0.945, 0.90, 0.79$ and 0.73. To sum up the important results: (i) for the nematic to isotropic transition, as the aerogel density ρ increased, there is a dramatic reduction in the magnitude of the excess N-I heat capacity peak and a systematic shift in the peak position relative to the bulk peak, (ii) the N-I transition was weakly first order for $\rho = 0.08$ and 0.17, but there was no evidence for a first order transition for $\rho = 0.36$ and 0.60, (iii) the N-SmA transition is modified severely (broad and very rounded C_p peaks) due to the presence of the aerogel network, and (iv) the transition temperature and the magnitude of the excess heat capacity $\Delta C_p(NA)$ vary systematically with the density ρ or average pore chord L.

3.1.2 Light Scattering

Bellini, Clark, and Schaefer performed dynamic light scattering experiments on $\rho =$ 0.08, 0.36, and 0.60 g/cm^3 8CB + aerogel samples [5]. They observed (i) a relatively fast (10^2 μs) relaxation near T_{NI} indicative of nematic intrapore orientational fluctuations, (ii) a slow relaxation reminiscent of a glassy behavior in the nematic range, and (iii) a dramatic slowing down for temperatures where the bulk smectic occurs.

3.1.3 X-ray Scattering

Because X-rays directly probe the density-density correlation function, smectic density waves can be easily studied with X-ray diffraction methods. For the LC + aerogel systems, a remnant of smectic ordering was observed with synchrotron X-ray diffraction [3, 28, 7].

The 8CB + aerogel samples used for the X-ray study were prepared in exactly same manner as those used for the calorimetry measurements described in section 3.1.1. Thus the densities were $\rho = 0.08$, 0.17, 0.36, and 0.60 g/cm^3. For all samples, a smectic peak considerably wider than the resolution-limited bulk smectic peak appeared for temperatures below the bulk T_{NA} at $q_0 = 2\pi/d \approx 0.2$ Å^{-1}, where d is the smectic layer spacing. Surprisingly there was another very broad but much smaller peak at almost the same q_0 value for temperatures spanning the range from above T_{NA} to well below T_{NA}, and this scattering was attributed to local smectic ordering on the aerogel surface.

The scattering profile was fit with a single Lorentzian above a certain "effective" transition temperature T^*, and two Lorentzians for $T < T^*$. Since a Lorentzian line shape is the powder average of a Lorentzian squared, the effect of a quenched random field was suggested to play a role in the scattering structure factor. Although bulk 8CB shows anisotropic correlation lengths, $\xi_{\parallel}$ and $\xi_{\perp}$ with $\xi_{\parallel}/\xi_{\perp}$ ranging from ~ 3 to ~ 15, the 8CB + aerogel system, on the other hand, was reportedly well described by a single correlation length.

The correlation lengths thus obtained at low temperatures were similar to the mean void chord L except for the $\rho = 0.08$ sample, in which case a monotonically increasing ξ was observed on cooling with a value at the lowest accessible temperature about twice as big as L.

3.1.4 NMR

Nuclear magnetic resonance (NMR) is a powerful tool for liquid-crystal research because of its capability to probe directly the orientational order Q, director configurations $\mathbf{n}(\mathbf{r})$, and molecular dynamics. Deuteron NMR (DNMR) has been successfully applied to liquid crystals in confined media as well as bulk studies [6].

In a nematic phases, the DNMR spectrum consists of two sharp absorption lines separated in frequency by

$$\delta\nu = \frac{1}{2}\delta\nu_0 Q(3\cos^2\theta_B - 1), \tag{3.1}$$

where $\delta\nu_0$ is the maximum frequency splitting observable in a fully aligned bulk nematic sample, Q is the scalar order parameter, and θ_B is the angle between the static magnetic field of the NMR and the nematic director $\mathbf{n}$. θ_B is 0 for bulk due to the magnetic-field-induced uniform alignment. For confined liquid crystals, however, θ_B as well as other parameters in the above equation have positional dependence, i.e., $\delta\nu = \delta\nu(\mathbf{r})$, $Q = Q(\mathbf{r})$, and $\theta_B = \theta_B(\mathbf{r})$.

An excellent DNMR experiment on 8CB + aerogel was performed by Zeng, Zalar, Iannacchione, and Finotello [6]. Their samples ranged from $\rho = 0.068$ g/cm^3 to

$\rho = 0.600$ g/cm^3, which correspond to the void volume fractions (ϕ_P) ranging from 0.95 to 0.73.

In the isotropic phase, they observed for aerogel samples a broader absorption peak than that of the bulk, which is typical of confined liquid crystals regardless of the randomness of the host media. This is attributed to the remnant, nematic-like order in the isotropic phase, sometimes referred to as paranematic order. This broad peak's width increased rapidly as the temperature decreased near T_{NI}, which is suggestive of quasi-complete wetting of the aerogel surface from homeotropic anchoring of the 8CB molecules on aerogel strands.

Below T_{NI}, all aerogel samples except the one with the highest density showed powder-pattern DNMR spectra indicative of randomly oriented nematic domains with a single value of Q. Nematic ordering was suppressed as density increased, eventually vanishing at the highest density. Interestingly there was no enhancement of orientational order as the temperature dropped further down below bulk T_{NA} even though X-ray studies found smectic scattering. It was suggested that the confinement decoupled the smectic and nematic order parameters.

Before we finish the discussion of the NMR results, it should be mentioned that NMR employs a static magnetic field which could cause the systems to behave differently than when there was no applied field at all. The criteria on the field strength is that the external magnetic field does not affect the aerogel – or aerosil – samples' induced director structure of the nematic liquid crystal once the confining length L (the aerogel void size) is smaller than the magnetic coherence length ξ_M. The magnetic coherence length is given by

$$\xi_M = \sqrt{\frac{\mu_0 K}{B_0^2 \Delta\chi}}, \tag{3.2}$$

where K is the average Frank elastic constant (single elastic constant approximation), B_0 is the applied static magnetic field strength, and $\Delta\chi$ is a measure of the anisotropy of the magnetic susceptibility. For the experiment discussed above, a 4.7 T magnet was utilized and it was reported that $\xi_M \approx 1$ μm, which is well above the confining length L for all aerogel samples (which varied from 12 nm to 91 nm). Thus with the weak applied magnetic field there should not be any noticeable effect on the director structure. This argument is further strengthened by the observed powder patterns.

3.2 LC + Aerosils

3.2.1 Calorimetry

As discussed in chapter 1, there has recently been interest in the effect of aerosil gels on liquid crystal phase transitions due to the fact that random disorder could be introduced in a more controlled manner than with rigid aerogels. This work began with precise calorimetry studies which produced important results in the early stage of LC + aerosil research. Zhou, Iannacchione, Garland, and Bellini successfully demonstrated that aerosils affect the liquid crystal transition differently than aerogels [8]. The LC-aerosil dispersions were first prepared by direct mechanical mixing of the 7 nm aerosil powder particles with the liquid crystal (8CB or $\overline{8}$S5), and the resultant changes in the character of the N-I and N-SmA transitions were studied through ac calorimetry. In contrast to LC + aerogels, very sharp C_P peaks were found for low density aerosils ($\rho \leq 0.09$) at the N-SmA transition, and the excess heat capacity ΔC_P could be well described with a power law yielding a heat capacity critical exponent α. For 8CB, where the pure bulk liquid crystal has an exponent value $\alpha = 0.30$, this critical exponent decreased on adding aerosil until $\alpha = -0.03$ for $\rho \approx 0.09 \mathrm{g/cm}^3$. This latter value is close to the 3D XY value of -0.007 that would be expected at an ideal N-SmA transition. For $\overline{8}$S5, whose bulk value of $\alpha = -0.022$ is already close to the 3D XY value, the critical exponent did not change significantly when aerosil was added to the system. The transition temperatures were observed generally to shift downward as the density of silica was increased, and a complex dependence on the aerosil density (described below) was seen in later experiments.

Further calorimetry studies on LC + aerosil systems have produced similar results. Important improvements were also made in the method of sample preparation.

In order to improve the homogeneity of the aerosil dispersion and increase the range of accessible densities, a solvent method was devised. The liquid crystal was first dissolved in a high-purity solvent (absolute ethanol or spectroscopic grade acetone). The aerosil powder was then introduced, and the system sonicated to insure a uniform dispersion. Finally, the solvent was removed by vacuum distillation. Haga and Garland studied the 4O.8 + aerosil system using this solvent preparation method, and the N-SmA transition showed similar crossover from positive $\alpha \approx 0.135$ of the bulk 4O.8 to a negative $\alpha \approx -0.066$ for $\rho_S \approx 0.109$ g/cm^3, again close to the 3D XY value of α [9]. Also the 8CB + aerosil system was revisited in detail by Iannacchione, Garland, Mang, and Rieker with the improved sample preparation technique, and similar results were reproduced, i.e., a crossover from a positive α to 3D XY value [11]. In this experiment, both the transition temperatures T_{NA} and T_{NI} were measured as functions of the aerosil density and each one showed qualitatively the same complex behavior. There was a rapid initial decrease in the transition temperature as ρ increased up to ~ 0.05 g/cm^3. This was followed by a modest recovery (slight increase in T_C) as ρ increased from ~ 0.05 to ~ 0.1g/cm^3. A subsequent increase in ρ caused a monotonic decrease in T_C. Because the low density samples showed very sharp C_P peaks, unlike LC + aerogels, while the high density samples featured smeared C_P peaks similar to LC + aerogels, $\rho \leq 0.1$ g/cm^3 was labelled as "soft" gels and $\rho \geq 0.1$ g/cm^3 as "stiff" gels. Small angle X-ray scattering (SAXS) was also performed, and this showed that the fractal aerosil network was very similar to that of aerogels. Thus, for the low-density gels, it was suggested that the elastic strain, which smears the transition in the case of rigid aerogels and stiff sil gels, was annealed and the surface anchoring played the role of a quenched random field to the system through the decoupling of nematic and smectic order parameters. However, this interpretation is purely heuristic with little direct evidence.

An additional calorimetry study of 7O.4 + aerosil conducted by Haga and Garland showed that the first order N-SmA transition of bulk 7O.4 remained first order, and it was suggested that the aerosil randomness was too weak to change the transition to a continuous one for $\rho_S \leq 0.14$ g/cm^3 [10].

3.2.2 Other Experiments

Light scattering measurements on the 6CB + aerosil system were performed by Bellini *et al.* through turbidity measurements [12]. The estimated nematic correlation lengths ζ followed the power law $\zeta \propto \Phi_{\mathrm{SiO_2}}^{-1.6}$, where $\Phi_{\mathrm{SiO_2}}$ was the silica volume fraction and ζ was of the order of μm, which far exceeds the mean void sizes of the corresponding gels.

Mercuri, Ghosh, and Marinelli studied the specific heat and the thermal conductivity of homeotropically aligned 8CB + aerosil and 7CB + aerosil samples with sil densities below the gelation threshold and found a history dependent behavior for the thermal conductivity in the nematic phase [13]. This was attributed to the elastic strain not being completely annealed at T_{NI} on cooling.

A nuclear magnetic resonance study was carried out by Jin and Finotello on deuterated 8CB (8CB-αd_2, deuterated at the first carbon position along the hydrogen chain) + aerosil dispersions [14]. Due to the nature of NMR, a $B_0 = 4.7$ T magnetic field was used and the effect of the magnetic field on the aerosil structure was observed. It was suggested that the director structure induced by the surfaces is affected by the magnetic field if the magnetic coherence length $\xi_M = \sqrt{\mu_0 K / B_0^2 \Delta\chi} \sim 1 \mu m$ is less than the mean void size l_0, where K is the average Frank elastic constant and $\Delta\chi$ is a measure of the anisotropy of the magnetic susceptibility. Thus, those samples with densities below the gelation threshold were aligned by the magnetic field. It was speculated that the field also had an effect of breaking the silica strands of the low density gels and realigning some of the nematic domains whose dimension is, supposedly, larger than the magnetic coherence length once the field direction changes. In the case of high density gels, the disordering effect of the silica strands dominated the molecular orientation, and the magnetic field effect was weak. The transitional behavior of these NMR aerosil samples was consistent with the calorimetry results, i.e., the lower-than-gelation-threshold samples were bulk-like, the soft gels had sharp transitions, and the stiff gels were like rigid aerogels.

Most recently Hourri, Bose, and Thoen carried out dielectric measurements on heptylcyanobiphenyl (7CB) perturbed by the dispersion of 70-(Å)-diameter hydrophilic silica spheres in an aligning magnetic field of 0.5 T [15]. The density dependence of the nematic to isotropic transition temperature followed the general trend of decreasing T_C as ρ_S increases. Interestingly one low density sample showed a large transition temperature shift similar to what was seen for 8CB + aerosil measurements [11]. The dielectric behavior in the nematic phase gradually changed from the bulk 7CB behavior as a function of density, and higher density samples showed a slower dielectric process absent in the bulk sample, which the authors attribute to surface layers formed by the 7CB molecules at the silica aerosil surface.

Chapter 4

Experimental Techniques

4.1 Sample Preparation

8CB + aerosil samples were prepared at M.I.T. in Professor Carl W. Garland's laboratory during the early stages of research and later at Worcester Polytechnic Institute in Professor Germano Iannacchione's laboratory using the same equipment and following the same preparation procedure as described in Ref. [11].

The bulk 8CB used in this experiment was obtained from Aldrich in 1 g bottles from a single synthetic batch. The chemical had a quoted 98% purity and was used without further purification.

A hydrophilic aerosil (type 300) was obtained from Degussa Corp [45]. The sil consists of 70-Å-diameter SiO_2 spheres with hydroxyl groups covering the surface and a specific surface area of $a = 300\ \mathrm{m^2g^{-1}}$ determined from a Brunauer-Emmett-Teller adsorption isotherm. The aerosil was dried under vacuum at ~ 200 °C overnight before use.

The preparation method starts by adding the silica powder to a dilute solution of 8CB in a solvent. Either absolute ethanol or acetone can be used as the solvent [9, 11], but spectroscopic-grade acetone was used exclusively in this study since it is readily available and allows comparison with previous calorimetry results. The mixture was mechanically stirred and sonicated to achieve a good dispersion of silica particles before being placed on a hot plate at temperatures just above 42 °C to evaporate the solvent slowly. It is later placed under vacuum at 10^{-3} Torr for about 12 hours at 50 °C to remove any remaining solvent and water vapor from the sample.

The samples prepared in this method were white (chalk-like) at room temperature and had a uniform appearance. When heated above the bulk T_{NI}, the samples turned semi-transparent but the gel structure was maintained, i.e., they were good gels. A few attempts to make dilute samples very near the gelation threshold ($\rho \approx 0.02$ g/cm^3) resulted, however, in phase separation, and those samples were discarded.

4.2 Synchrotron X-ray Scattering

Because none of the samples including pure 8CB characterized in this study were under any applied field, they were powders in a X-ray diffraction sense. Although the experimental procedures are in some ways simpler when dealing with a powder sample, which does not require a serious search for a Bragg peak, the scattered intensity is significantly reduced compared to that of a single crystal because just a small fraction of the domains satisfies the Bragg reflection condition. That is, for a high resolution experiment, only a tiny section of the diffraction ring is observed at any given time, as depicted in Fig. 4-1. This causes a significant problem when the X-ray source is not bright enough. Indeed, initial attempts to see the scattered beam with a rotating-anode X-ray source (see Ref. [46] for details) failed due to very poor signal-to-noise ratio.

4.2.1 Synchrotron Radiation

A synchrotron, on the other hand, can produce an X-ray beam several orders of magnitude brighter than that of rotating-anode X-ray sources. Charged particles (typically electrons), moving with relativistic speed in curved trajectories emit electromagnetic radiation due to acceleration, and this is called synchrotron radiation. There are three components of a synchrotron which produces radiation: bending magnets, wigglers, and undulators.

Charge particles are constrained to move in arc trajectories in bending magnets,

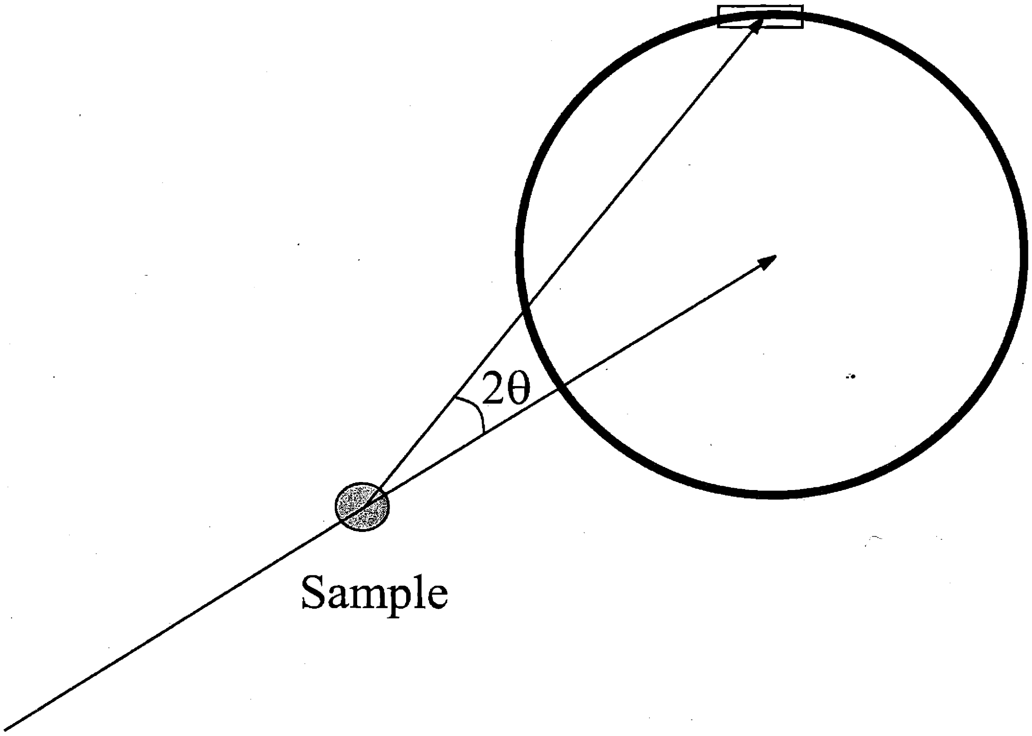

Figure 4-1: Powder Ring

With a powder sample, the diffracted beam forms a powder sphere centered about the direct beam. For high resolution measurement of $S(q)$, a very narrow section of the ring is scanned along the 2θ angle. It is not possible to completely remove the effects of the arc. A small box which represents the counted area still contains not just the photons scattered to 2θ but also $2\theta - \delta\theta$ at both left and right ends. Therefore, the box must be made as small as possible using slits, which inevitably reduces the counts. Therefore, a balance must be sought between the intensity and resolution.

and produce a continuous spectrum of electromagnetic radiation, which is often referred to as a “white beam”.

A wiggler consists of an array of magnets with alternating polarity. Due to the alternating magnetic field, the electron itself follows a sine-like wiggling trajectory, radiating at each wiggle.

An undulator is similar to a wiggler, but the electron path is designed so that the radiation from each wiggle would interfere with the others. Due to the interference, the outgoing spectrum consists of a discrete fundamental line plus many harmonics.

4.2.2 X-ray Optics

The X-ray scattering experiments described in this thesis were performed on the X20A and X20C beam lines of National Synchrotron Light Source (NSLS). These two essentially identical beam lines are jointly operated by MIT and IBM. A detailed description of these beam lines can be found in Ref. [47].

Figure 4-2 is a schematic diagram of the scattering geometry for both beam lines. The diagram is separated into two parts representing outside and inside the hutch components respectively. The setup is essentially that of triple axis spectroscopy (TAS). TAS has been widely used for both X-ray and neutron scattering experiments for its simplicity and “inefficiency” [48], and the important components are the monochromator, the sample (2θ), and the analyzer axes as shown in the diagram. In this experiment, however, the monochromator and the analyzer angles are fixed once the X-ray energy is selected.

Outside the hutch, the incoming white beam from the synchrotron source is reflected by a focusing mirror made of platinum coated silicon which is controlled by a piezoelectric material so that the beam can be focused at the place of choice. In this experiment, the beam is focused at the center of the spectrometer where the sample is located. The reflected beam from the focusing mirror is Bragg scattered by a pair of monochromator crystals (scanning double-crystal fixed-exit-beam monochromator) to select a well defined energy from the white beam. Si (111) surface is used to monochromatize the beam for the X20A and X20C beam lines. 8 keV X-rays, which

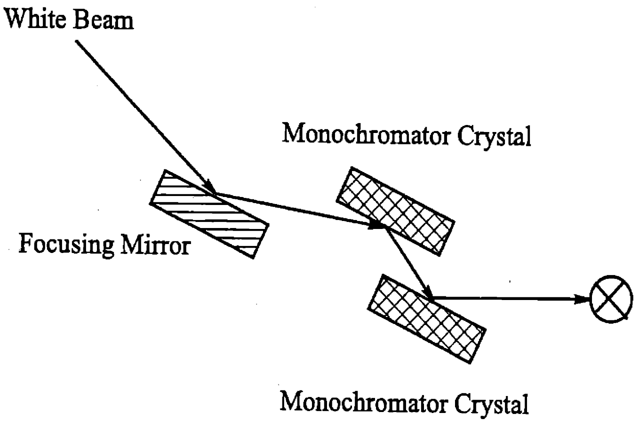

(a) Outside the hutch

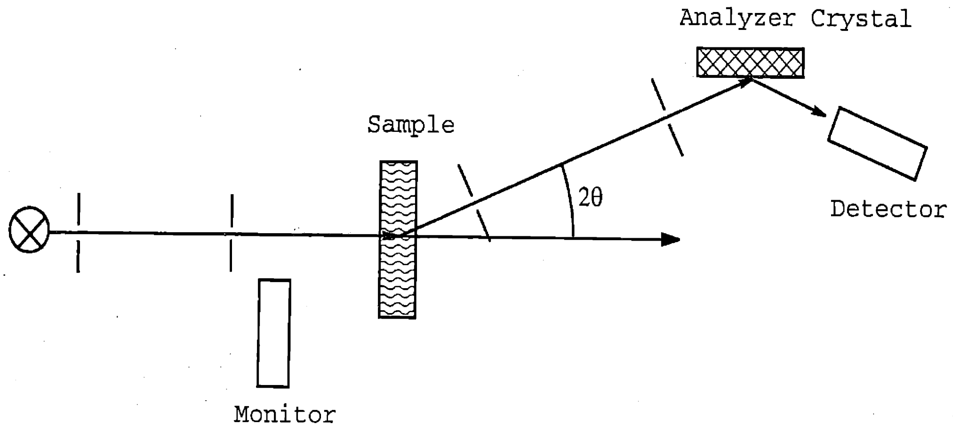

(b) Inside the hutch

Figure 4-2: Scattering Geometry

correspond to the wavelength of 1.54 Å, were used exclusively in these experiments. Unfortunately, the third harmonic with an energy three times that of the selected X-ray photons is also Bragg reflected from a Si (111) surface as well as the first harmonic. The signal from the third harmonic is suppressed by the use of a pulse height analyzer by counting the signal pulses that belong to the properly chosen energy band only.

The two sets of slits between the monochromator and the sample serve the dual purposes of defining the beam tightly and preventing any stray beam from reaching the sample. A monitor is set up just after the second set of slits to provide a means to normalize the data against the intensity of the incoming beam. The air particles in the path of the beam scatter photons, and some of them are counted by the monitor. It is imperative to have this monitor because typically between injections of electrons into the synchrotron (twice a day) the number of electrons inside the synchrotron decays to about half of its maximum and the X-ray intensity drops accordingly. After the beam is scattered by the sample it goes through two sets of slits which serve to narrow the instrumental resolution. An analyzer crystal is located just before the detector to enhance the resolution even further. Si (111) or Ge (111) were typically used as the analyzer, with Si having a slight edge over Ge with respect to resolution and Ge over Si with respect to intensity. We typically chose Ge because the gain in intensity could justify a slight loss in resolution for our weak powder diffraction signals.

The monitor and the detector were identical Bicron detectors composed of a NaI scintillation counter composed of a photomultiplier tube and a preamplifier. Each incident X-ray photon generates a current pulse whose amplitude is roughly proportional to the incident photon energy. The pulse height analyzer mentioned above selects those pulses corresponding to the first harmonic, and a timer/counter counts number of pulses for a given amount of time.

4.3 Sample Environment

For X-ray scattering experiments, consideration should be given to the scattering geometry according to the sample properties. One of the most important property here is the X-ray attenuation length. The details about the attenuation length are presented later in this thesis (see section 6.3). It is sufficient to say that the attenuation length of 8CB + aerosil samples for 8 keV X-ray is $\sim$ 1 mm, and the sample holder is designed to make the sample roughly 1 mm thick for scattering in a transmission geometry.

The sample was placed between two aluminium holders with epoxy sealed Kapton windows, and the sample cell was then placed in a two-stage oven backfilled with dry N_2 gas for stable temperature control. Figure 4-3 shows the location of the sample in relation with the two-stage oven and a diagram of the sample holder. The Kapton window is placed where the diameter of the hole in the sample holder changes. The depth of the sample is 2×0.02 inches $\approx$ 1 mm when two such holders are used. Mylar and Aluminized Mylar were also used as windows for comparison, and there was no discernible difference in the data from when Kapton was used.

The two-stage oven consists of an inner oven which holds the Kapton windowed sample cell and the outer oven with a cylindrical Beryllium window which contains the dry N_2 gas. To reach temperatures below room temperature, a thermoelectric cooler (TEC) was used. A 60 W TEC with a fan was placed on top of the two-stage oven for constant operation during cooling runs. For stable temperature control, a home-made P-I temperature controller was used for the inner oven, and a Lakeshore temperature controller for the outer oven. For the temperature range we investigated (15 °C $\sim$ 45 °C), however, it was not even necessary to use the outer oven. Using the outer oven as merely gas container, the temperature variation during a scan was typically ±0.001 °C.

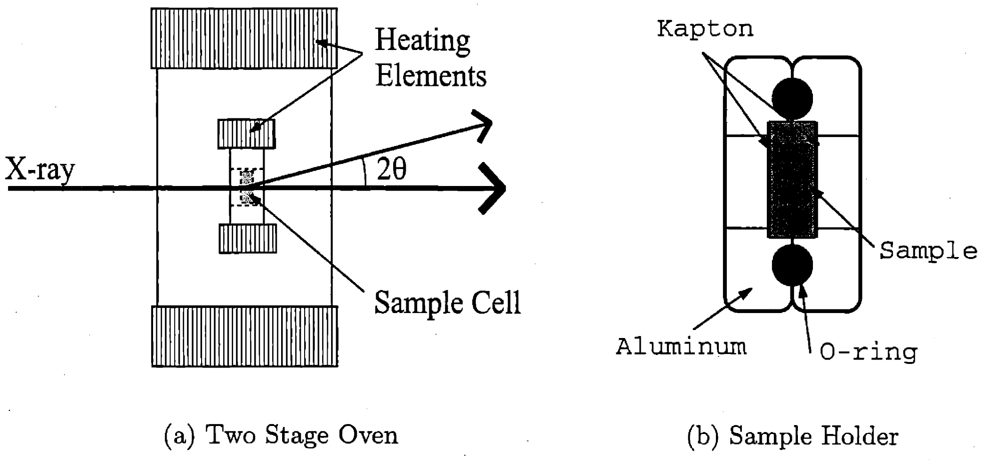

(a) Two Stage Oven

(b) Sample Holder

Figure 4-3: Sample Environment

(a) The sample cell is placed in a two-stage oven which is backfilled with dry N_2 gas. (b) The sample holder is made of Aluminium and has a hole at the center so that X-rays can pass through. The sample is placed between a pair of such holders with epoxy sealed Kapton windows.

4.4 Measurements

Once the sample was placed in the oven, dry N_2 gas was backfilled and the temperature was raised to 45 °C where it remained overnight ($\sim$ 8 hrs). This protocol was developed to remove any remaining solvent or water from the sample as well as to give enough time for silica strands to re-arrange in case they were pressed too hard when the sample was first placed in the cell. In fact, the above mentioned annealing process was more important for $\bar{8}$S5 + aerosil because $\bar{8}$S5 crystallizes at room temperature, thus the silica structure can be distorted during transportation.

Measurements were made by cooling a few tenths of a degree, waiting for half an hour or more for the temperature to reach the designated point, and taking a scan before moving on to a new temperature. All measurements were done by scanning 2θ angles instead of typical $\theta - 2\theta$ scan for single crystals. In this way X-ray photons would hit the same parts of the sample all the time, avoiding complications when the θ-axis is also rotated.

Figure 4-4(a) show raw data from the 8CB + aerosil $\rho = 0.200$ g/cm^3 sample at a few selected temperatures. The strong background due to aerosil scattering can be easily identified in the figure.

Beam Damage

Although it would be ideal if we could take measurements indefinitely with one sample, this was not possible due to sample deterioration. It was observed that when the sample was placed in a X-ray beam for a prolonged period of time the onset in the growth of smectic ordering shifted downward in temperature visibly. This phenomena has been observed for 8CB + aerogel measurements [28] as well as for bulk 8CB measurements [46]. It is not yet quite clear what process is going on when X-rays hit the 8CB and/or silica strands. Although the powerful X-ray photon is suspected to be able to break the bonds of liquid crystalline molecules, a very high energy X-ray ($\sim$ 50 keV) is reported to have no effect on the transition temperatures of a liquid crystal [49].

One way to reduce the beam damage is to count fewer photons for each data point, thus reducing the amount of time the sample spends in the beam. We have performed systematic reduction of statistics to the level where there was no noticeable change of temperature dependence when measurements at a series of temperatures were repeated on an already exposed sample. Also measurements at high temperatures were restricted to just a few temperatures to further cut the exposure in order to avoid a severe transition temperature shift.

Resolution

As discussed in section 1.3, the intrinsic X-ray scattering line shapes are broadened by the instrumental resolution. Thus it is important to know the resolution function with precision if accurate correlation functions are to be extracted from the scattering data. For a powder diffraction geometry, it is easily achieved by looking at the direct beam itself.

Figure 4-5 illustrates the relation between the direct beam profile and the resolu-

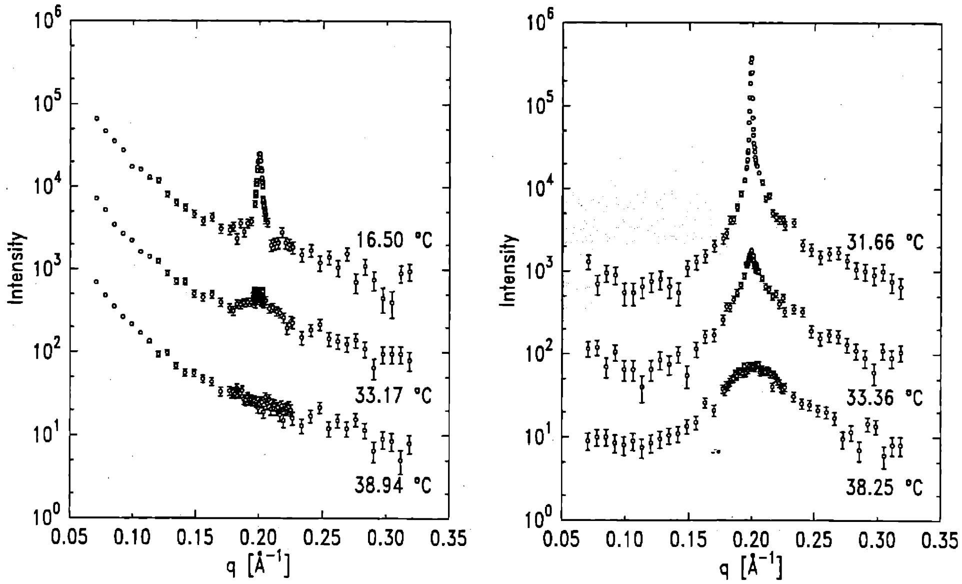

(a) 8CB + aerosil $\rho = 0.200$ g/cm^3

(b) Bulk 8CB

Figure 4-4: Raw Data

The data points in this figure have been moved upward or downward for easy viewing. For both plots, the lowest temperature points (top) were multiplied by 50, the middle by 5, and the highest temperature points (bottom) by 0.5. (a) Raw data of a high density sample show a very strong background due to scattering from the gel structure. (b) Bulk 8CB at $T = 38.25$ °C show a sign of smectic layering above bulk transition temperature. The 33.36 °C data do not exhibit a sharp resolution limited peak even though the temperature is below the literature bulk $T_{NA} \sim 33.9$ °C value. Pure 8CB is especially susceptible to beam damage compared to the 8CB + aerosils, and the transition temperature seems to have shifted downward in this case. 31.66 °C data show the resolution-limited smectic peak.

tion function for powder diffraction geometry. Simply put, the beam divergence δ in the direct beam remains the same when a perfectly Bragg reflecting powder sample is placed in the beam. The resolution function for our direct beam is shown in figure 4-6.

Bulk 8CB

The bulk 8CB was also put in the sample cell for powder diffraction measurements for comparison with 8CB + aerosil samples. Figure 4-4(b) shows typical scans for the bulk 8CB with the horizontal axis representing the scattering wave vector in reciprocal space. Because bulk 8CB was more susceptible to beam damage than 8CB + aerosil samples, no detailed systematic study of the temperature dependence was made for the pure bulk material. However, it is expected that bulk 8CB has a resolution limited line shape below bulk T_{NA}, and indeed the bulk 8CB line shape closes matches that of the direct beam as shown in figure 4-6.

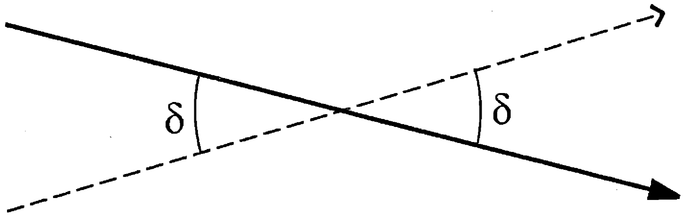

(a) Direct Beam

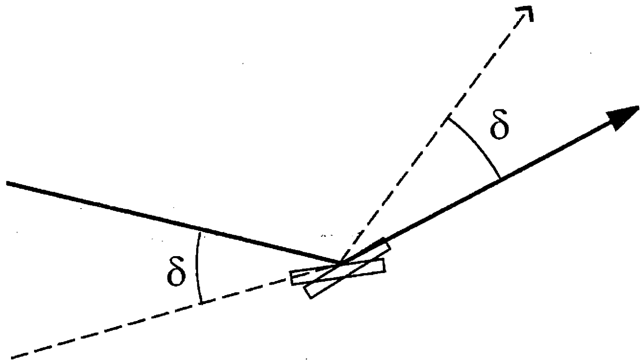

(b) Reflected Beam

Figure 4-5: Resolution Function For Powder Diffraction Geometry

If a perfect powder is used, the beam divergence of the direct beam is maintained. Therefore, the direct beam profile can be used as the resolution function in powder diffraction geometry. However, it should be noted that this is only true if $\delta\theta$ from figure 4-1 is much smaller than δ. Otherwise, the observed resolution would be wider by $\sim \delta\theta$ than the direct beam profile.

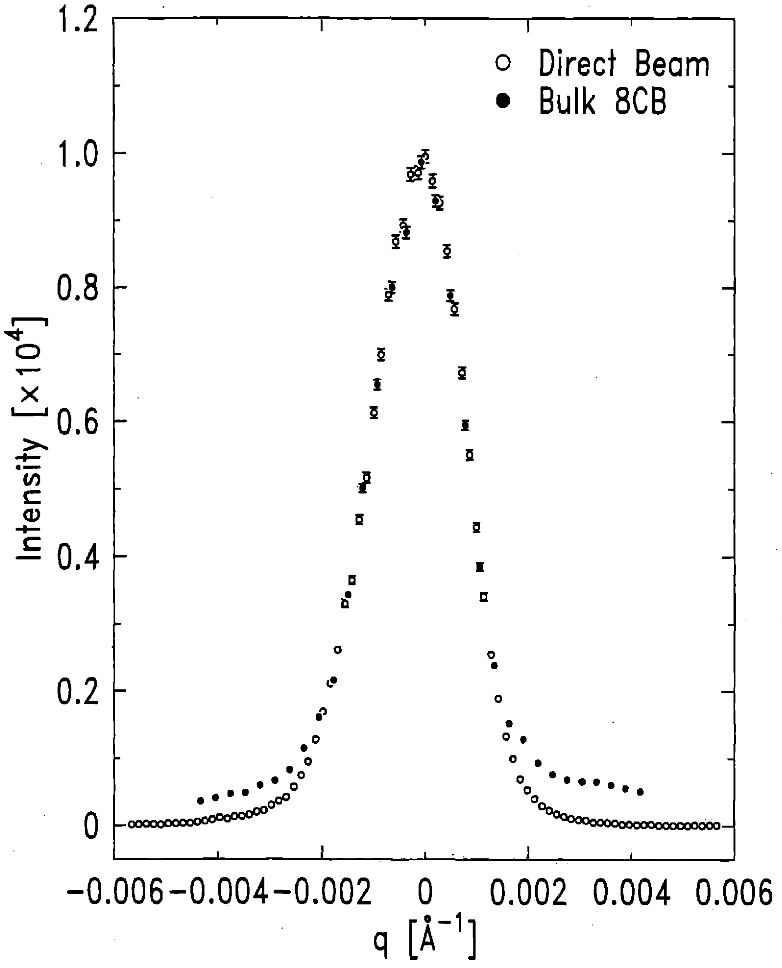

Figure 4-6: Resolution Function

The open circles (○) represent the direct beam and the closed circles (●) represent bulk 8CB data shifted and multiplied by 1.2 to match the direct beam for comparison. The two sets of data closely agree very well with each other and have the same width as expected.

Chapter 5

Destruction of The Smectic Quasi-Long Range Order

5.1 Introduction

Following the general Imry-Ma type argument in chapter 2, the smectic long range order is not expected to survive even the weakest quenched randomness imposed on the system. This conclusion is also supported by the Radzihovsky-Toner theory for randomness effects on liquid crystals. Finding experimental evidence of this is feasible since X-ray scattering techniques directly probe the density correlation of smectic phases.

The 8CB + aerogel system has already been studied with X-rays, and it had the expected property of short-range correlation with no smectic quasi-long range ordering being observed [28]. It should be noted, however, that calorimetry results for 8CB + aerogels had already showed severe smearing of the heat capacity peak, indicating that a rigid aerogel provides too strong quenched randomness for any long range ordered state to survive at low temperatures.

The calorimetry results for the 8CB + aerosil system, however, showed an interesting behavior. The heat capacity peak associated with the N-SmA transition for low sil densities remained sharp enough that it was possible to fit it with a power law, indicative of very long correlation lengths and much weaker quenched randomness than with aerogels. X-ray scattering techniques should be able to provide the correlation lengths of this novel disordered system, and this chapter provides the result of such an effort.

5.2 Background

One of the complications in this experiment is that the network of silica particles interacts with the probing beam as well. There are primarily two effects that should be considered in this experiment: scattering and absorption of X-ray by the silica network. The former results in a strong background contribution to the resulting scattering profile as can be seen in figure 4-4(a), and the later reduces the total intensity of the scattered beam as a function of the amount of silica in the sample (both sample thickness and sil density contribute). The effect of absorption will be discussed later in section 6.3.

The other contributions to the total scattering besides the main smectic peak come from nitrogen gas, Kapton windows, and the diffuse scattering from the liquid crystal itself in increasing importance. The scattering from the nitrogen gas and the Kapton windows is orders of magnitude smaller than the scattering from the silica in the samples for the range of q of interest ($0.1\ \text{Å}^{-1} < q < 0.3\ \text{Å}^{-1}$), and these can be neglected safely. Kapton has a strong scattering peak at $q \approx 0.4\ \text{Å}^{-1}$, but it does not have any noticeable effect on the smectic peak which is located far from this wave vector at $q \approx 0.2\ \text{Å}^{-1}$.

To extract the smectic peak from the total scattering, the above mentioned contributions must be eliminated carefully. Because there is no smectic peak in the isotropic phase of 8CB, data taken above T_{NI} effectively contain all the contributions except the interesting smectic peak, and such data can be used as the background to be subtracted from the total scattering profile. A few of such high temperature data are shown in figure 5-1. The data sets in this figure are shifted in order to avoid confusing overlap and permit easier comparison. At low q, it is essentially the scattering from the silica that dominates the scattering profile, and the scattering

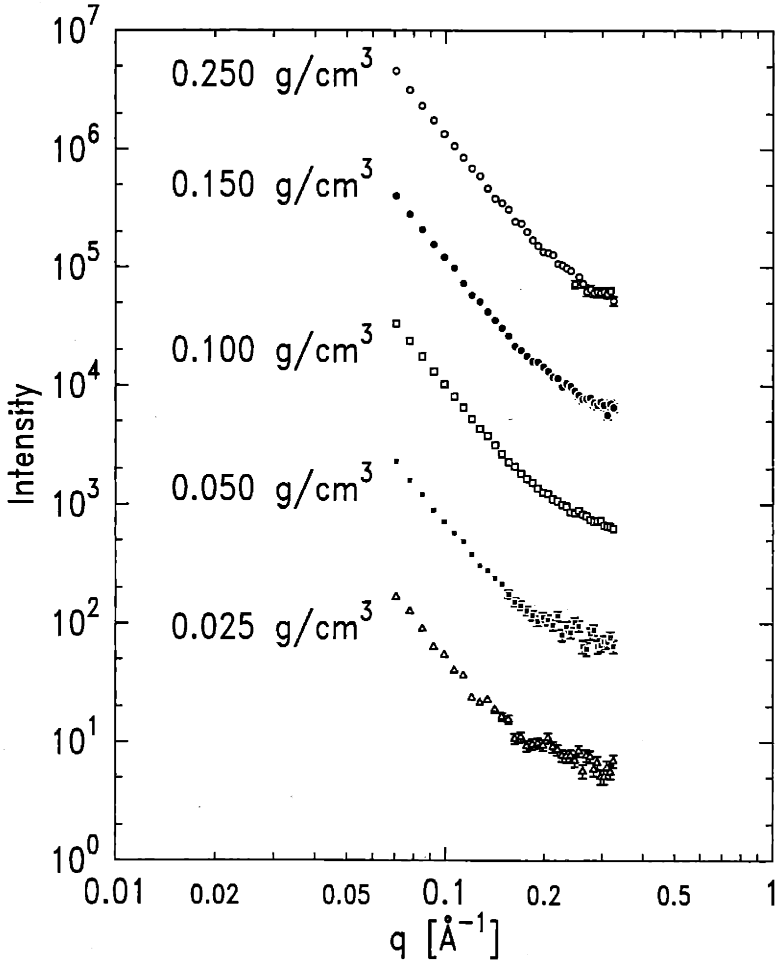

Figure 5-1: High Temperature ($T > T_{NI}$) Scans

These high temperature scans of 0.25, 0.15, 0.10, 0.05, and 0.025 g/cm^3 samples have been normalized and then multiplied by 1000, 100, 10, 1, and .1 respectively to show them individually.

profile has essentially the same power law behavior for all densities. At high q, a contribution from the liquid crystal diffuse scattering becomes important, and the data show a bend from the steep power law region to a relatively flat region. Since scattering from silica is more important for high density samples, this crossover of the data curve is relatively weak at high densities, e.g., the $\rho = 0.250$ g/cm^3 sample has a barely observable bend at high q.

It is known, however, that the background changes slightly as measurement takes place at $T < T_{NI}$. The difference in the thermal expansion coefficients of silica and the liquid crystal, the reduction of the diffuse scattering from 8CB when T decreases past T_{NI}, and changes in the incoming beam profile as a function of time are the three important reasons for this behavior. It was found empirically that changes in the background can be modelled very well by multiplying an isotropic temperature scan by a temperature-dependent factor denoted as b. Therefore, if we define the high temperature scan as $B(q)$, the background at a temperature $T < T_{NI}$ can be expressed as $b(T)B(q)$. In the X-ray scattering experiments reported on 8CB + aerogel samples, there was an additional adjustable constant in the total background, resulting in one more parameter in the fitting program, i.e., $a(T) + b(T)B(q)$ was subtracted from the total scattering profile [28]. It was not necessary to include an additional constant $a(T)$ in the present aerosil experiments.

5.3 Wider-Than-Resolution Widths

Before moving on to the full description of the line shape analysis, it is worth mentioning that one of the most important results of the experiment was obtained by inspecting the scattering profiles directly. As stated previously, bulk 8CB had resolution limited smectic peaks below T_{NA}, proving that our bulk sample retained smectic quasi-long range order, hence a SmA phase. Compared to the bulk result, all 8CB + aerosil samples with densities above the gelation threshold (~ 0.02 g/cm^3) had wider smectic Bragg peaks. In fact, as the silica density in the samples increased, the width corresponding to the smectic peak of each sample progressively widened.

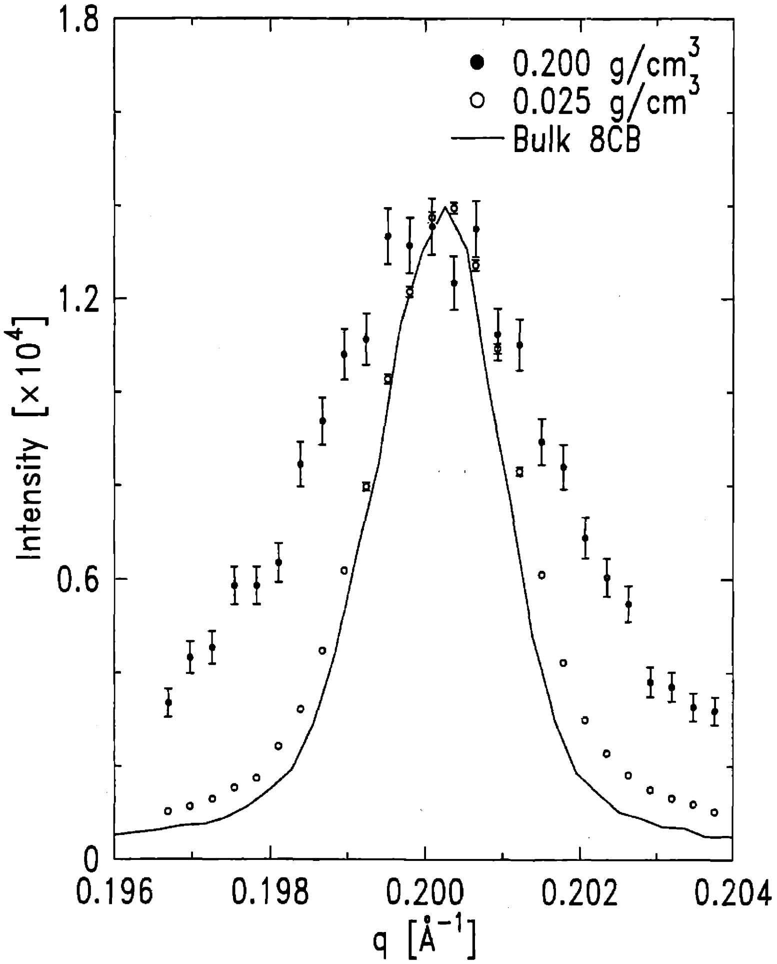

Figure 5-2: Wider-Than-Resolution Widths
The filled circles (•) represent a 0.200 g/cm^3 sample at 16.50 °C, the open circles (○) a 0.025 g/cm^3 sample at 14.62 °C, and the solid line (—) bulk 8CB at room temperature and thus in the SmA phase. The 0.200 and bulk data were shifted horizontally and normalized in magnitude to match the top of the 0.025 data.

Figure 5-2 illustrates this point very well. Even at the lowest temperature [1] (16.50 °C), the lowest density sample investigated, $\rho = 0.025$ g/cm^3, has a scattering peak which is wider than the resolution-limited bulk 8CB smectic peak, although the width is very close to that of the resolution. For comparison, the scattering profile of a high density sample, $\rho = 0.200$ g/cm^3, is also plotted in the same figure. The width of the peak for the high density sample is significantly larger than the resolution, indicating a considerably smaller correlation length than for the low density sample.

This result indicates that the smectic quasi-long range order is destroyed even for the lowest density 8CB + aerosil sample above the gelation threshold despite the apparently sharp heat capacity peak shown at the "N-SmA" transition. This destruction of smectic quasi-long range order is consistent with the theories previously described in chapter 2. Reconciliation of calorimetry and X-ray scattering results will be discussed later in the next chapter.

5.4 Method of Analysis

To extract useful information from the scattering data, a proper fitting function with a plausible physical basis is required. A few intrinsic line shapes that are used frequently for the analysis of X-ray scattering of liquid crystals are discussed in appendix B.

5.4.1 High Temperature Line Shape

The observed scattering profile was markedly different between the high temperature regime and the low temperature regime separated by $T^* \sim T_{NA}$, where T^* is defined to be the "effective" transition temperature of a given 8CB + aerosil sample corresponding to the sharp increase of almost resolution-limited peak at low temperatures. Note that T^* is not well defined for high density samples due to severe smearing of the transition. T^* is not an ordinary N-SmA transition temperature, T_{NA}, because we

---

[1] The crystallization temperature of pure 8CB is 20 °C. However, the crystallization is suppressed by several degrees by the aerosil, and the temperature can be reduced to a few degrees below the bulk crystallization temperature without freezing the 8CB and breaking the silica network.

have already shown there is no SmA phase for 8CB embedded in an aerosil random structure. It is still possible that T^* indicates the onset of a topological order.

The X-ray scattering study of 8CB + aerogels revealed a similar difference between the line shapes in these two temperature regimes, and a single Lorentzian was used for $T > T^*$ and two Lorentzians for $T < T^*$ to analyze that data [46]. Including the background terms, the total fitting function used by Rappaport [28] for 8CB + aerogels was

$$\begin{aligned} I_+(q) &= \frac{A_0}{1+(\xi_0(q-q_0))^2} + bB(q) + a, \quad (T > T^*) \qquad (5.1) \\ I_-(q) &= \frac{A_L}{1+(\xi_L(q-q_L))^2} + \frac{A_S}{1+(\xi_S(q-q_S))^2} + bB(q) + a, \quad (T < T^*) \qquad (5.2) \end{aligned}$$

where A_0, A_L, and A_S are amplitudes, ξ_0, ξ_L, and ξ_S are correlation lengths, and q_0, q_L, and q_S are centers of Lorentzians. Indices L and S denote large and small Lorentzians, respectively. Note that the total number of free parameters were 5 when $T > T^*$ and 8 when $T < T^*$.

Although our 8CB + aerosil data could also be fit well with the above scheme, comparison of the sil data with the bulk 8CB scattering profile as well as requirements of the most physically plausible model for $T > T^*$ led us to adopt a different fitting function. Figure 5-3 demonstrates the similarity of the bulk and 8CB + aerosil line shapes at high temperatures, an indication that 8CB + aerosil data could be fit well with the same type of fitting function that is used for the bulk material in this high temperature regime.

This similarity is not surprising after all, considering that the critical thermal fluctuations have small correlation lengths largely unaffected by the aerosil network at high temperatures. Therefore, it is natural to use a similar line shape form that also describes the bulk behavior at least for $T > T^*$.

It has been known since the pioneering work of Als-Nielsen *et al.* [50] that the X-ray scattering line shape of the thermal fluctuation of liquid crystals can be described by an anisotropic Lorentzian with higher order corrections. Traditionally, an anisotropic Lorentzian with a fourth order correction in the transverse direction

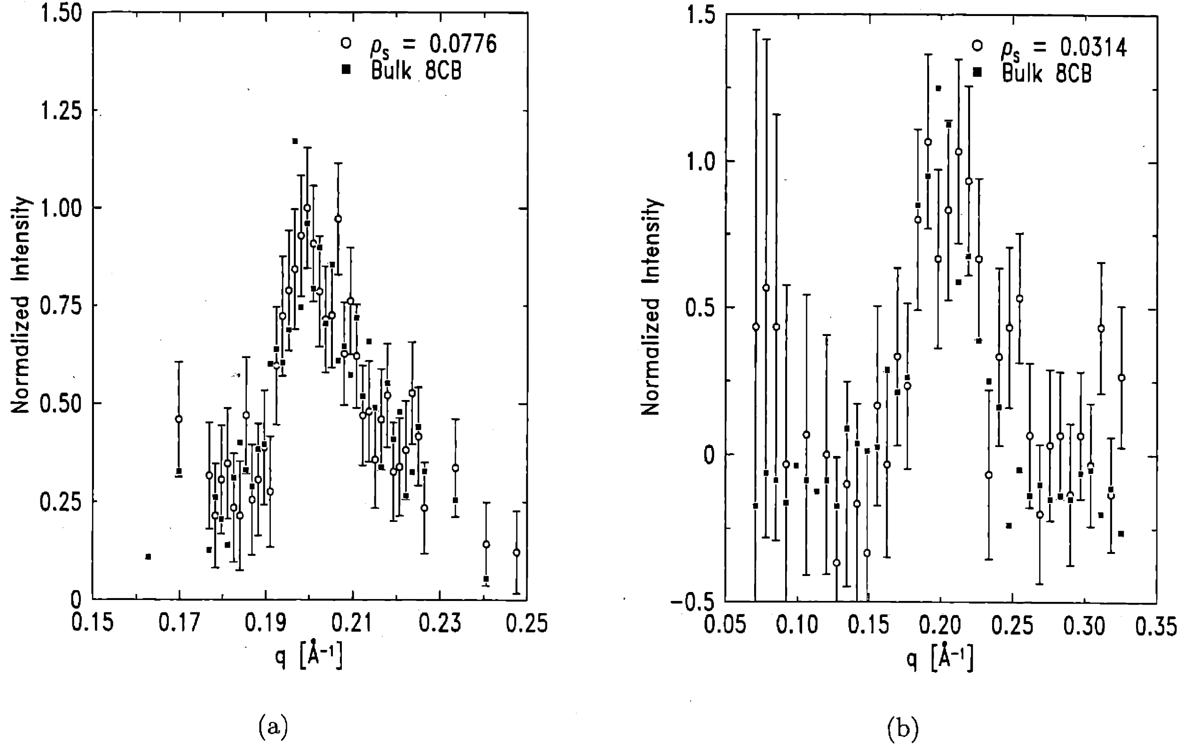

Figure 5-3: Comparison of Bulk 8CB and 8CB + Aerosil Line Shapes
When $T > T^*$, the 8CB + aerosil line shape is similar to that of the bulk material. (a) The 8CB + aerosil sample compared to bulk 8CB is $\rho_S = 0.0776$ g/cm^3 at 35.13 °C. The bulk data was taken at 35.09 °C. (b) $\rho_S = 0.0314$ g/cm^3 sample at 37.61 °C is compared with the bulk 8CB at 37.33 °C. (a,b) All scattering data are raw data minus background. The background data were taken from a scan at $T > T_{NI}$ and used without any scaling. The peak heights were normalized to unity at q_0 for easy comparison.

(LFC) has been widely used by experimentalists [16, 46]:

$$S(\mathbf{q}) = \frac{\sigma}{1 + \xi_{\|}^2(q_{\|} - q_0)^2 + \xi_{\perp}^2 q_{\perp}^2 + c\xi_{\perp}^4 q_{\perp}^4}, \tag{5.3}$$

where $q_{\|}$ and $q_{\perp}$ are the wave vectors parallel and perpendicular to the layer normal respectively.

An anisotropic Lorentzian raised to the power $1 - \eta_{\perp}/2$ along the transverse direction (LPC) is an equally valid form [16]:

$$S(\mathbf{q}) = \frac{\sigma}{\xi_{\|}^2(q_{\|} - q_0)^2 + (1 + \xi_{\perp}^2 q_{\perp}^2)^{1-\eta_{\perp}/2}} \tag{5.4}$$

The anisotropic correlations is not unexpected. After all, liquid crystals are anisotropic liquids because of the anisotropic molecular force. Strangely large corrections to the anisotropic Lorentzian, however, is not well understood theoretically.

Although either LFC or LPC could be used in the current data analysis, LFC was chosen due to a practical reason – it was possible to powder-average LFC exactly while LPC required very slow numerical powder averaging. The intricacies of powder averaging will be discussed in section 5.4.3.

5.4.2 Low Temperature Line Shape

The observed low temperature scattering profile has a shape qualitatively similar to that seen in the case of 8CB + aerogels, i.e., on top of a broad peak that developed above T^*, a sharp but still wider-than-resolution peak grows rapidly as temperature decreases below T^*. One of the simplest interpretations of this phenomena is growing static correlations modified by the quenched disorder which replaces the Bragg delta-function scattering from long-range smectic ordering with a short-ranged order scattering profile. Therefore, we model the scattering structure factor for low temperatures in the following way:

$$S(\mathbf{q}) = \frac{\sigma_1}{1+\xi_\parallel^2(q_\parallel - q_0)^2 + \xi_\perp^2 q_\perp^2 + c\xi_\perp^4 q_\perp^4} + \frac{a_2 \xi_\parallel \xi_\perp^2}{\left(1+\xi_\parallel^2(q_\parallel - q_0)^2 + \xi_\perp^2 q_\perp^2 + c\xi_\perp^4 q_\perp^4\right)^2} \tag{5.5}$$

where a_2 is a parameter that is approximately proportional to the integrated intensity of the second term. This second term, which is the square of the thermal fluctuation term with a separate amplitude, is a standard term that describes short-range correlations induced by static fluctuations in random magnetic systems [51-55]. This term has been theoretically justified for RFIM by Pelcovits *et al.* [56], which developed upon Grinstein *et al.* [57]. A Lorentzian squared structure factor corresponds to algebraically decaying exponential correlation ($e^{-r/\xi}/r^{(d-3)/2}$) for three dimension. When correlation lengths diverge, it becomes a Bragg delta peak, $a_2\delta(q_\parallel - q_0)\delta(\mathbf{q}_\perp)$. (Note that $q_\perp$ is the amplitude of a two dimensional vector $\mathbf{q}_\perp$.)

The relationship between the structure factor for thermal fluctuations and static fluctuations originating from a random field can be obtained by a simple calculation starting from the Landau-Ginzburg free energy functional [58]. This calculation results in a static structure factor which is the square of thermal fluctuation term. Therefore, the anisotropic correlation lengths and the higher order correction term are retained in the second term of equation 5.5.

Thus the total fitting function used for all 8CB + aerosil samples was

$$\begin{aligned} I(\mathbf{q}) \;=\; & \frac{\sigma_1}{1+\xi_\parallel^2(q_\parallel - q_0)^2 + \xi_\perp^2 q_\perp^2 + c\xi_\perp^4 q_\perp^4} \\ & + \frac{a_2 \xi_\parallel \xi_\perp^2}{\left(1+\xi_\parallel^2(q_\parallel - q_0)^2 + \xi_\perp^2 q_\perp^2 + c\xi_\perp^4 q_\perp^4\right)^2} + bB(q), \end{aligned} \tag{5.6}$$

The $I(q)$ equation can be written in the short-hand form $I = LC + LC^2 + bg$, where the form of the background bg has been discussed in section 5.2. Technically one might have used Eq. 5.6 at all temperatures. However, when allowed to be freely adjustable a_2 is negligibly small for high temperatures, and therefore a_2 was set to zero to reduce scatter of the other parameters in this temperature range.

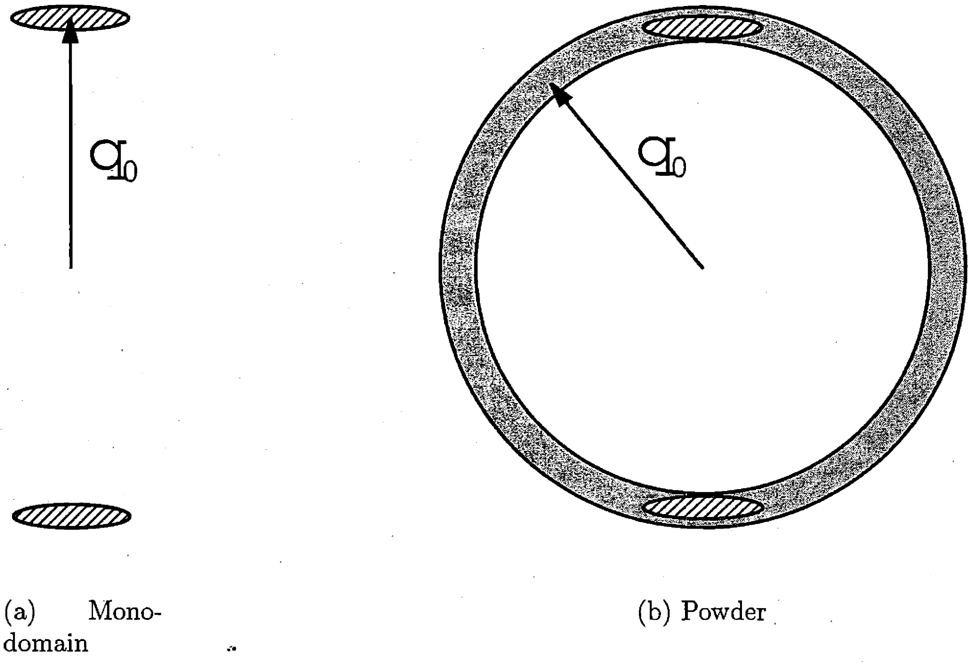

(a) Mono-domain

(b) Powder

Figure 5-4: Momentum Space Representation of Mono-domain and Powder Samples

5.4.3 Powder Averaging

It must be remembered that the samples we are dealing with are powders in an X-ray diffraction sense. Although bulk 8CB deviates from pure powder behavior as discussed before, 8CB + aerosil data do not show any such deviations, which is evidence that the aerosil network is properly randomizing the orientation of smectic domains. Therefore, the intrinsic line shape must be properly powder-averaged in order to be compared with the experimental data.

Figure 5-4 depicts the difference between mono-domain and powder samples in momentum space. With a line shape with finite width, the momentum transfer from a mono-domain sample can be any vector from the origin to a point in the shaded region around $\mathbf{q}_0$ or -$\mathbf{q}_0$ in figure 5-4(a). When it is a powder, $\mathbf{q}_0$ can point anywhere in the solid angle. Thus the tip of the momentum transfer vector forms a spherical shell as shown in figure 5-4(b).

Therefore, powder averaging is simply integrating the intrinsic mono-domain line shape over all solid angles for $\mathbf{q}_0$. Precise and approximate calculations of powder averaging typical line shapes are presented in Appendix B.

Since powder averaging involves integration, coupled with the convolution with the resolution function, which is another integration described below, numerical calculation of the line shape involves long computing times. Fortunately, for some intrinsic line shapes including LFC, the powder average can be calculated exactly – although it cannot be easily written in a closed form. That is one reason why LFC was chosen over LPC for the analysis of our 8CB + aerosil results.

5.4.4 Convolution With Resolution

As was shown in figure 5-2, the low density samples had line shapes with widths that are slightly wider than the resolution width. As in the case of high density sil samples and 8CB + aerogels, if the width is far greater than the resolution width, it is not necessary to consider the effect of finite resolution on the intrinsic line shape. However, when the width is barely larger than the resolution width, as in the case of the low density 8CB + aerosil samples, taking this effect into account is of high priority in order to properly extract meaningful data.

There are a few methods that can be used to counteract the effect of the resolution depending on the intrinsic line shape involved. Unfortunately, the powder-averaged line shape that is of concern here is so complex that it is required to numerically convolve the line shape with the resolution function before comparison with experimental data. One advantage of dealing with a powder in such a convolution is that only one dimensional integration is required due to the isotropic nature of powders, i.e.,

$$S_{observed}(q) = \int dq' \; S_{intrinsic}(q')\mathrm{Res}(q - q'), \tag{5.7}$$

where q and q' are used instead of $\mathbf{q}$ and $\mathbf{q}'$ of equation 1.14.

5.4.5 Employing Bulk Result

If the parameters in equation 5.6 are all allowed to vary freely, nonphysical spurious results can occur because of the large number of adjustable parameters involved in the fitting. The situation is much worse by powder averaging since all angular information is lost. This ambiguity can be overcome through the following physically reasonable assumption. Since the line shapes of 8CB + aerosil and the bulk 8CB are very similar to each other at high temperatures, some of the parameters can be interrelated in a manner similar to that in the bulk material, i.e., $\xi_\perp$ and the correction coefficient c can be tied to $\xi_\parallel$ precisely as they are in bulk 8CB. The relations between these parameters may be ascertained from the bulk 8CB critical properties.

Precise measurements of bulk 8CB were done by B. M. Ocko [46], and the critical exponents of $\xi_\parallel, \xi_\perp$ and c can be easily extracted from his tabulated results. Although c may not have any true critical behavior associated with it, the variation of c with t has been found to roughly follow a power law. The parameters shown in figure 5-5 were taken from the data reported in Ref. [46]. When fit with a power law, the results are

$$\begin{aligned} q_0\xi_\parallel &= 0.70\ t^{-0.702} && (5.8)\\ q_0\xi_\perp &= 0.443\ t^{-0.496} && (5.9)\\ c &= 0.528\ t^{0.249}. && (5.10) \end{aligned}$$

Therefore, $\xi_\perp$ and c can be expressed as a function of $\xi_\parallel$ simply by removing the reduced temperature t from these equations. We obtain

$$\begin{aligned} q_0\xi_\perp &= 0.570\left(q_0\xi_\parallel\right)^{0.707} && (5.11)\\ c &= 0.456\left(q_0\xi_\parallel\right)^{-0.355}, && (5.12) \end{aligned}$$

and these 8CB expressions have been assumed to be valid also for all the 8CB + aerosil samples.

Fixing $\xi_\perp$ and c through the relations 5.11 and 5.12 leaves five adjustable parameters: the amplitudes σ_1 and a_2, the location of the peak q_0, the correlation length along the director normal $\xi_\parallel$, and the background parameter b. For high temperatures, since a_2 is set equal to zero, there are then only four adjustable parameters.

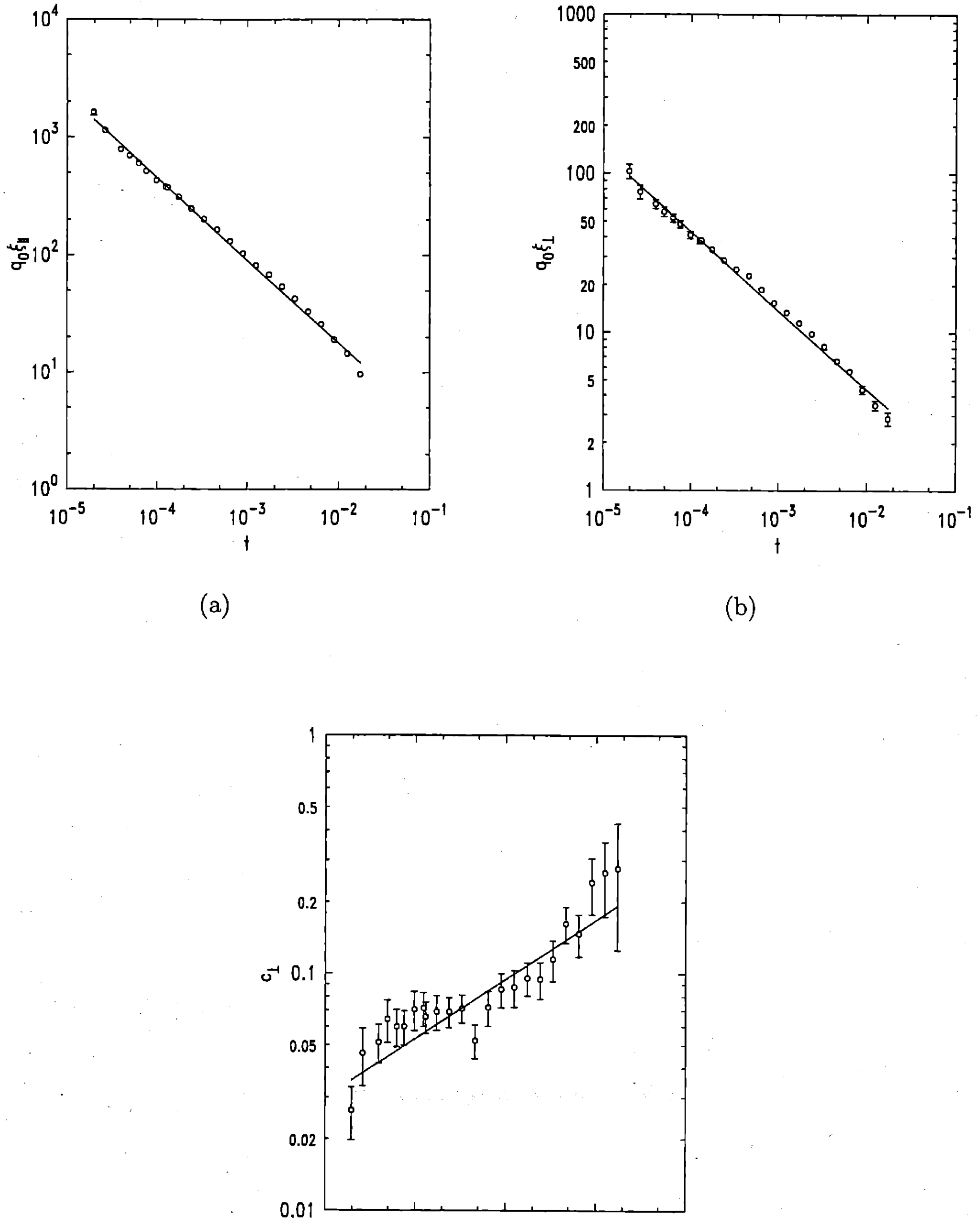

(a) (b)

(c)

Figure 5-5: Critical Behavior of Bulk Single-Domain 8CB
The data are taken from Ocko's thesis [46]. (a, b) Fitting the correlation lengths with a power law reproduced the well-known effective critical exponents $\nu_\parallel \approx 0.70$ and $\nu_\perp \approx 0.50$. (c) This 8CB correction coefficient was also taken from Ocko's thesis [46]. The coefficient decreases to zero as the reduced temperature approaches zero, and this behavior can be fit reasonably well with a power law. We obtained $c = 0.528\ t^{0.249}$.

The validity of this approach is confirmed by comparing the line shapes of 8CB + aerosil and $\overline{8}$S5 + aerosil.

Figure 5-6 is a simulated powder average of the bulk 8CB line shape. It can be readily seen from the figure that there is a slight asymmetry in the resulting line shape: the tail on the higher q side ($q > q_0$) has slightly more intensity than the lower q side ($q < q_0$). This is consistent with the observed behavior as shown in figure 5-3(a).

Figure 5-7 shows measurements on a $\overline{8}$S5 + aerosil sample compared with a calculated powder average of the pure $\overline{8}$S5 line shape. $\overline{8}$S5 has a different anisotropy $\xi_{\|}/\xi_{\perp}$ for the correlation lengths and a smaller 4th order correction coefficient c than 8CB. When powder averaged using the single-domain $\xi_{\perp} = f_{\xi_{\perp}}(\xi_{\|})$ and $c = f_c(\xi_{\|})$ relations, the resulting line shape has strong asymmetry: a large tail on the high q side. Actual data from the $\overline{8}$S5 + aerosil sample indeed have exactly such an asymmetry.

We will call the line shape obtained in this method employing the bulk measurement results as LC (or LC^2 for the squared term) throughout the rest of this thesis. It indicates that the pure bulk liquid crystal result was employed to constrain the parameters of the LFC by assuming that $\xi_{\perp}$ and c have values for a given freely adjustable $\xi_{\|}$ that are those which a single-domain bulk sample would have for that $\xi_{\|}$ value.

5.4.6 Fit Results

Fitting experimental data using the fitting function 5.6 generated through the above method, i.e., powder averaging $LC + LC^2$ and convolution with the resolution function, resulted in excellent fits. Figures 5-8 to 5-13 show representative fits for four samples at various temperatures and silica densities. For all samples and temperature ranges the goodness-of-fit parameter χ^2 remained roughly between 1 and 2.

Figures from 5-10 to 5-13 show the relative size of the LC and LC^2 parts of $I(q)$ in equation 5.6 for selected samples. When the temperature is close to T_{NA}, the LC term is the dominant contributor to the peak, and the LC^2 term is just a small fraction. On the other hand, the LC^2 term becomes dominant when $T \ll T_{NA}$, while

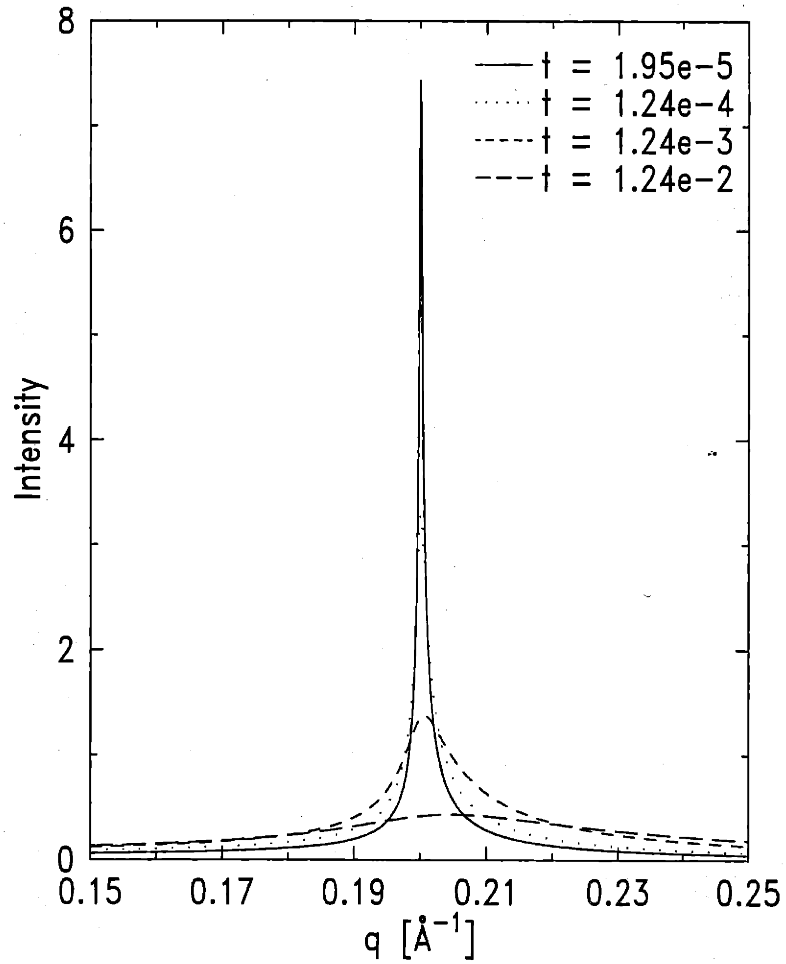

Figure 5-6: Simulated Bulk 8CB Line Shape

Single-domain 8CB data from ref [46] were used to simulate the powder averaged line shape of bulk 8CB. The corresponding correlation lengths and the correction coefficients in order of increasing reduced temperature t are ($\xi_{\parallel}$, $\xi_{\perp}$, c) = (8150 Å, 515 Å, 0.0264), (1890 Å, 189.5 Å, 0.0714), (408 Å, 67 Å, 0.0875), and (72.5 Å, 17.35 Å, 0.265).

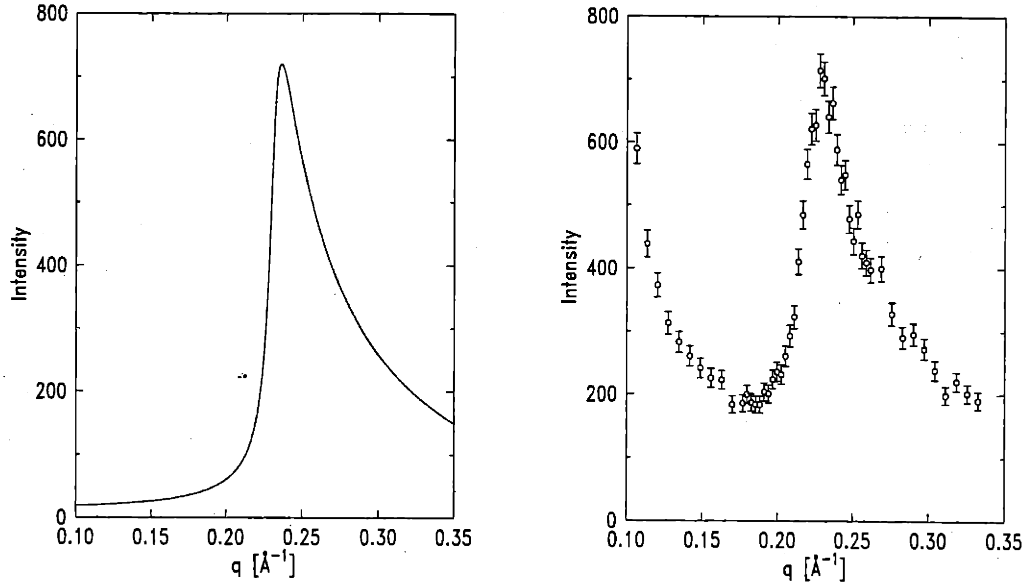

(a) Simulated Bulk $\bar{8}$S5 Line Shape

(b) Scattering Data From $\bar{8}$S5 + Aerosil

Figure 5-7: $\bar{8}$S5 and $\bar{8}$S5 + Aerosil Line Shape

Simulated powder average of $\bar{8}$S5 line shape has a close resemblance to the $\bar{8}$S5 + aerosil data. (a) Powder average of bulk $\bar{8}$S5 line shape is simulated with the parameters obtained from power law fits of single-domain $\bar{8}$S5 data in ref [59]. The line shape shown in the figure corresponds to $\Delta T \equiv T - T_{NA}^{\bar{8}S5} = 2.56$ °C, correlation lengths of $\xi_{\parallel} = 230$ and $\xi_{\perp} = 15$ Å and the 4th order correction coefficient $c = 0.04$. (b) Scattering data of $\bar{8}$S5 + aerosil $\rho = 0.030$ g/cm^3 at $T = 65.89$ °C, 2.56 °C above the bulk $\bar{8}$S5 N-SmA transition temperature. The data look very similar to the simulated powder average except a strong background due to the silica network at low q region.

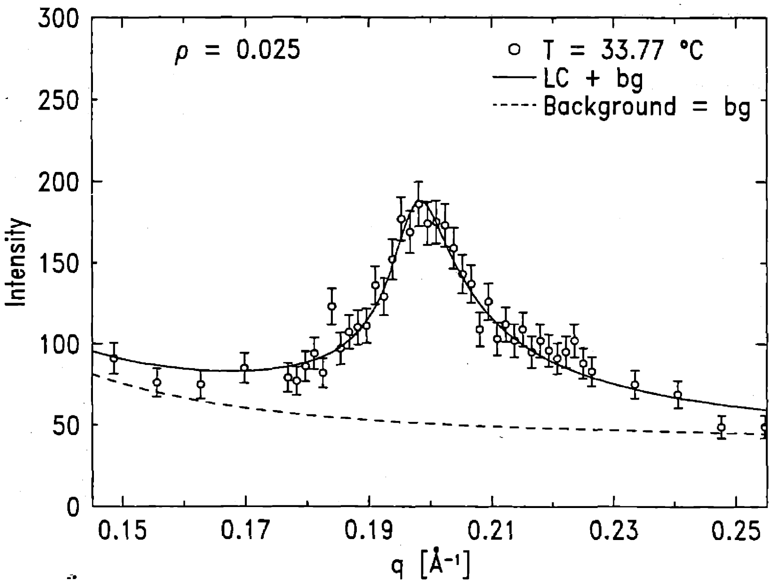

(a) $\rho = 0.025$ g/cm^3, $T > T^*$

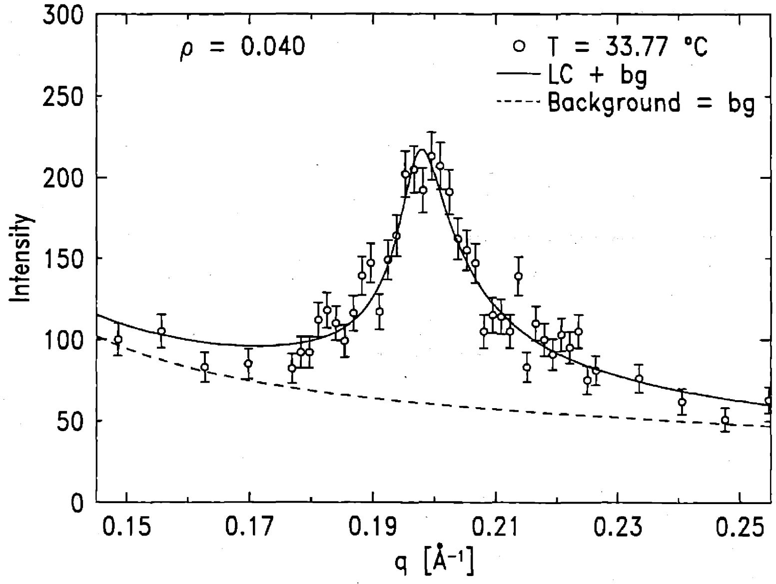

(b) $\rho = 0.040$ g/cm^3, $T > T^*$

Figure 5-8: Fitting Curve for $T > T^*$ for $\rho = 0.025$ and 0.040 g/cm^3 Samples

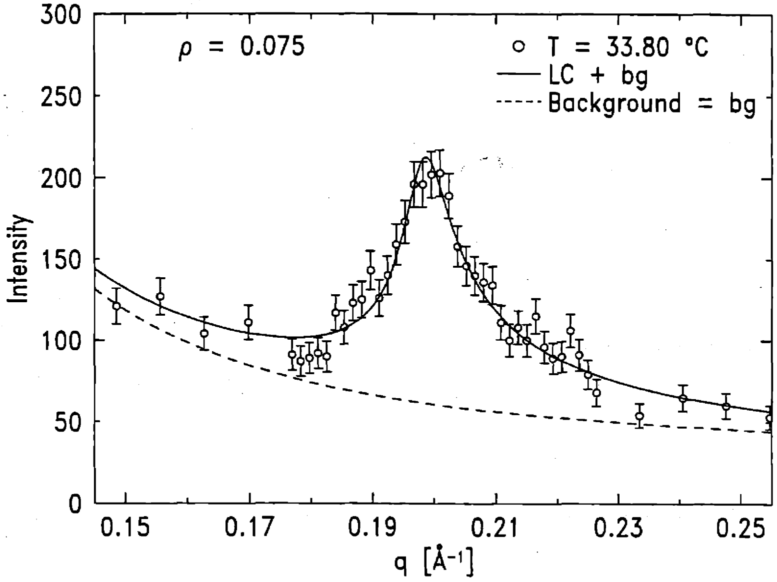

(a) $\rho = 0.075$ g/cm^3, $T > T^*$

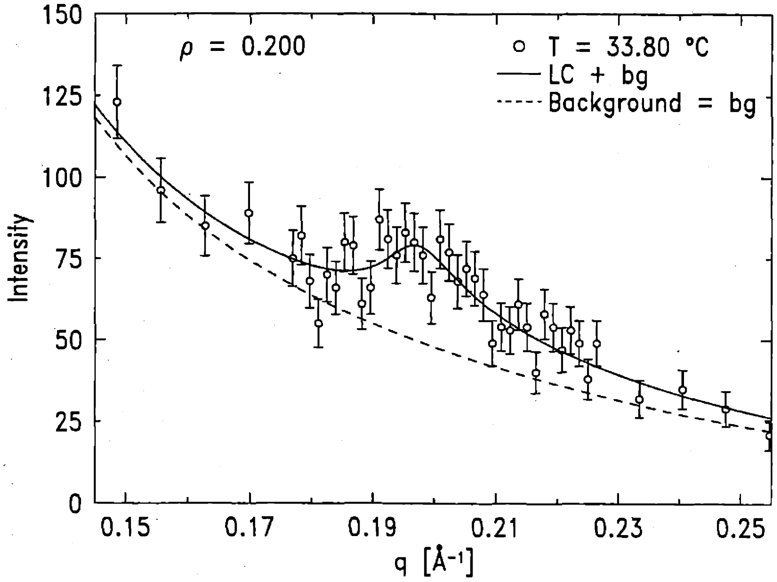

(b) $\rho = 0.200$ g/cm^3, $T > T^*$

Figure 5-9: Fitting Curve for $T > T^*$ for $\rho = 0.075$ and 0.200 g/cm^3 Samples

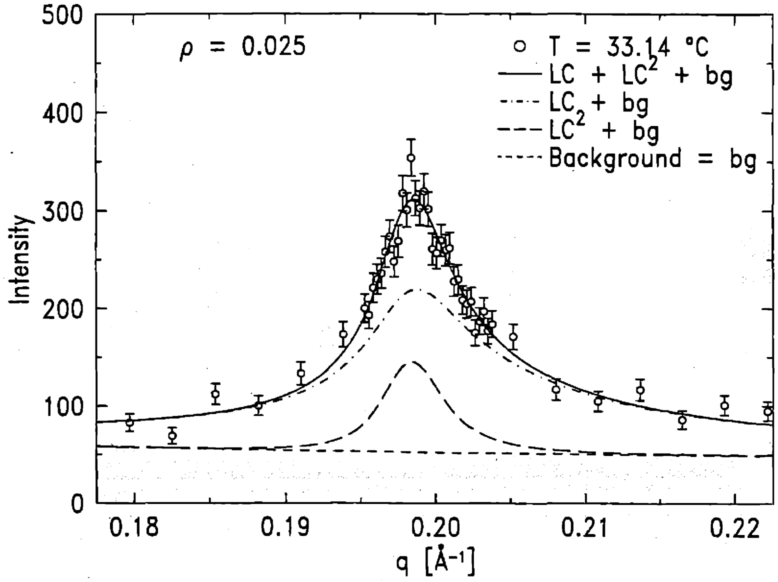

(a) $\rho = 0.025$ g/cm^3, $T \lesssim T^*$

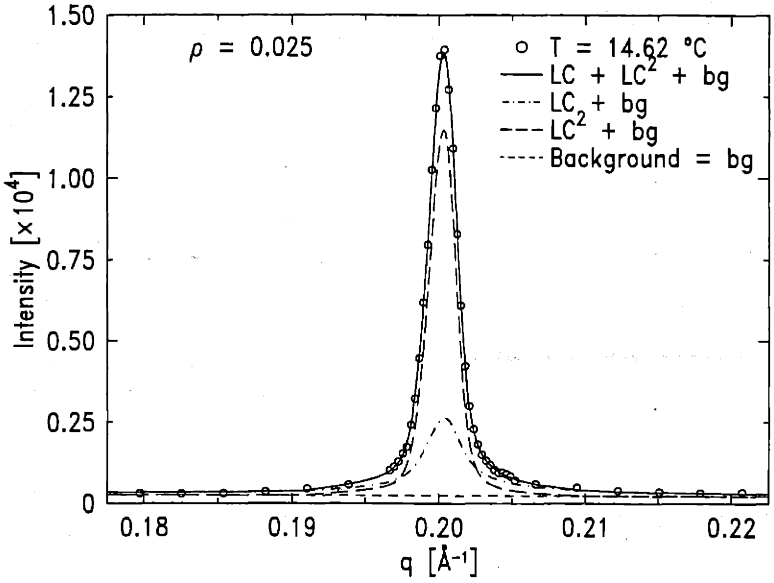

(b) $\rho = 0.025$ g/cm^3, $T \ll T^*$

Figure 5-10: Fitting Curve for $T < T^*$ for $\rho = 0.025$ g/cm^3 Sample
Note: the scan shown in (b) was taken by counting ten times more than usual. Thus the numbers shown on its vertical axis must be divided by 10 to be properly compared with those in (a).

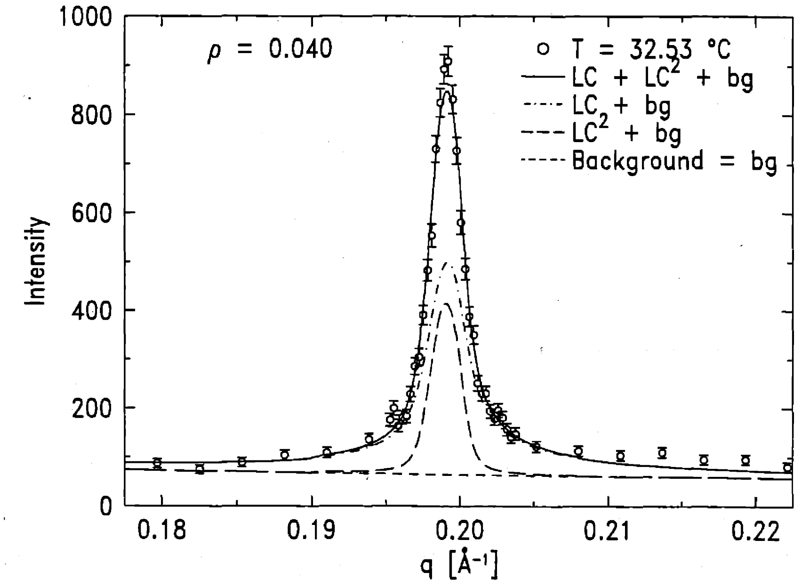

(a) $\rho = 0.040$ g/cm^3, $T \lesssim T^*$

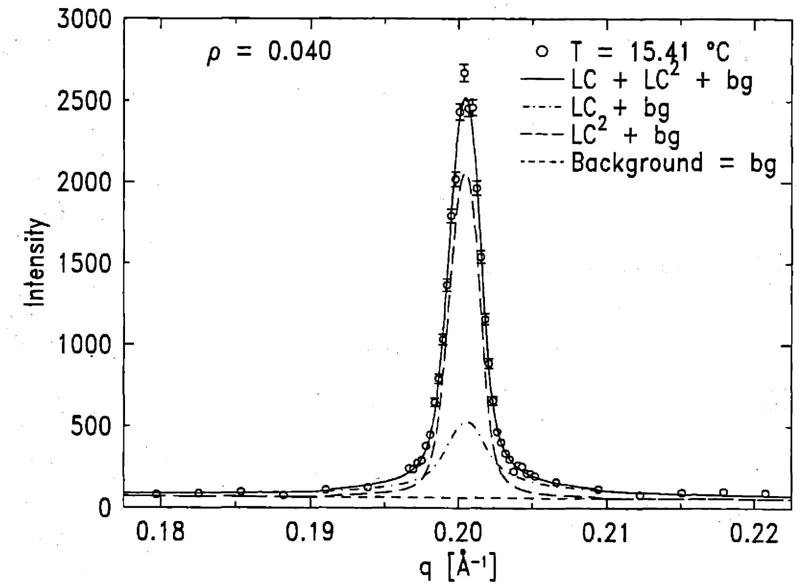

(b) $\rho = 0.040$ g/cm^3, $T \ll T^*$

Figure 5-11: Fitting Curve for $T < T^*$ for $\rho = 0.040$ g/cm^3 Sample

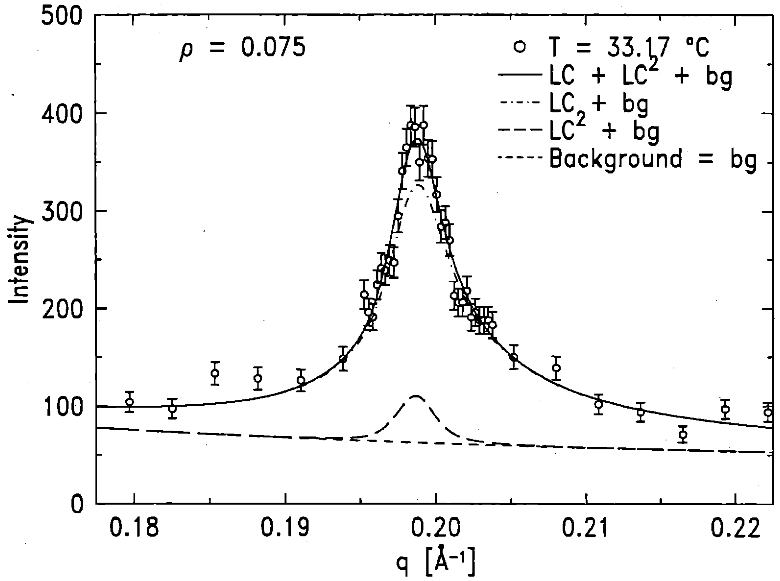

(a) $\rho = 0.075$ g/cm^3, $T \lesssim T^*$

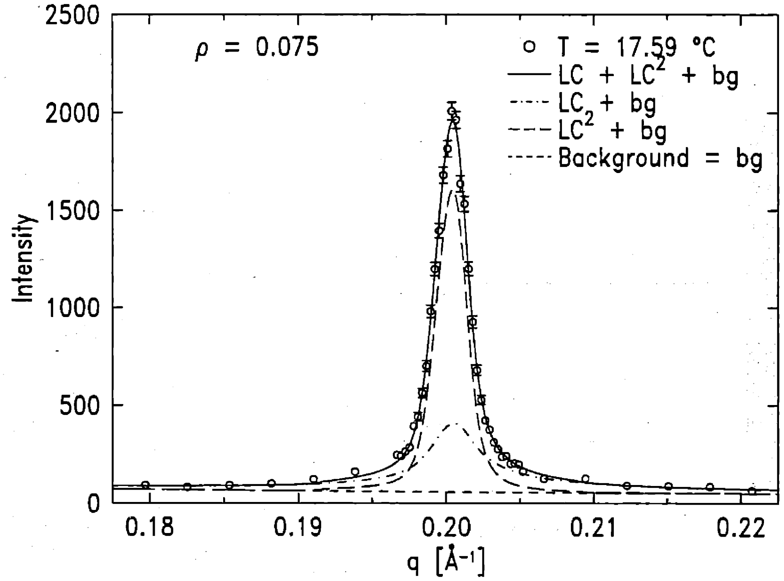

(b) $\rho = 0.075$ g/cm^3, $T \ll T^*$

Figure 5-12: Fitting Curve for $T < T^*$ for $\rho = 0.075$ g/cm^3 Sample

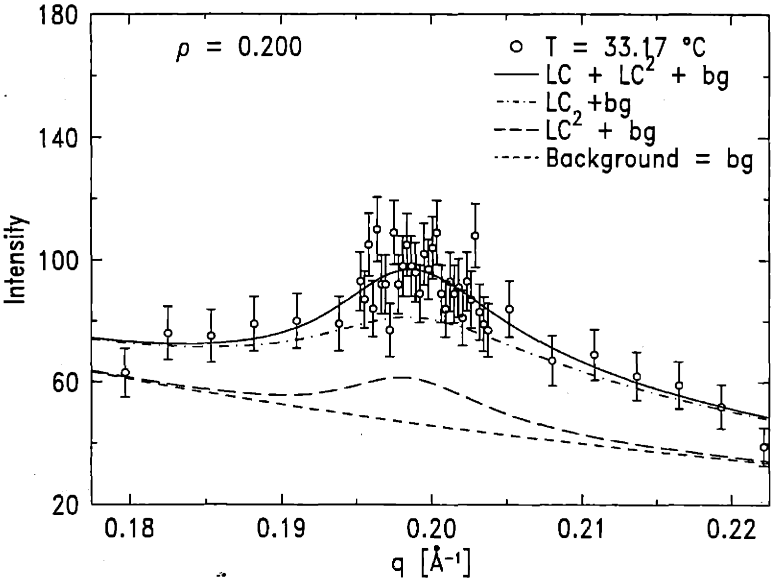

(a) $\rho = 0.200$ g/cm^3, $T \lesssim T^*$

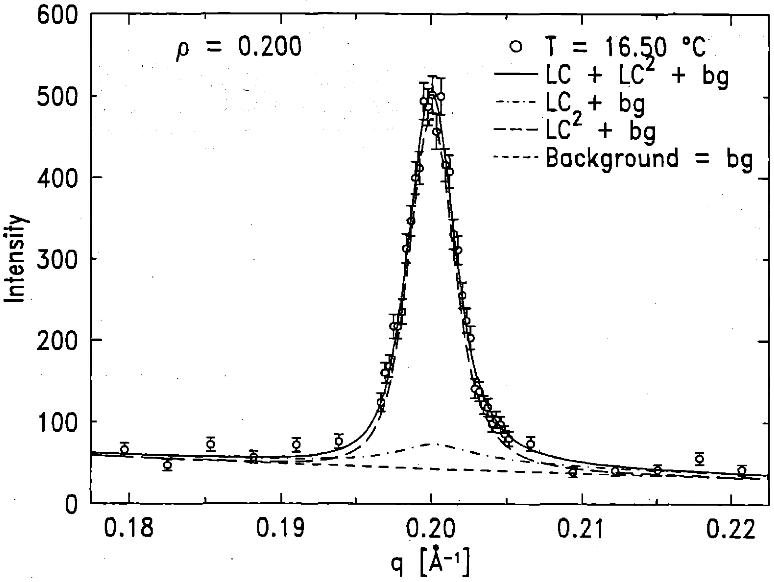

(b) $\rho = 0.200$ g/cm^3, $T \ll T^*$

Figure 5-13: Fitting Curve for $T < T^*$ for $\rho = 0.200$ g/cm^3 Sample

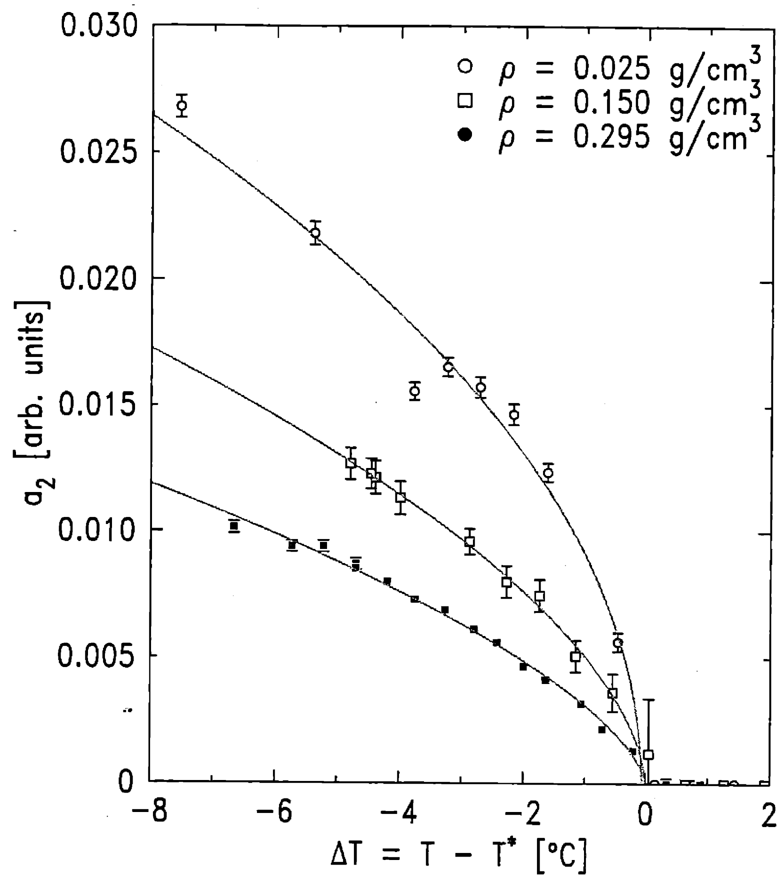

Figure 5-14: Fits of a_2

The power law equation 5.13 was used to fit a_2. Solid curves represent the fit curves. In this plot, a_2 has been scaled for easy viewing.

the *LC* part is small but still important since it explains most of the tails. Figures 5-11 and 5-12 show this behavior of the *LC* part especially clearly.

As seen from figure 5-14, a_2 rapidly decreases to zero as T increases toward the effective "transition" temperature T^*. Since a_2 shows order-parameter-like behavior, it was fit with an empirical power law:

$$a_2 = A_2 \left| T - T^* \right|^x . \tag{5.13}$$

As described previously, when a_2 was taken as a free parameter for high temperatures, the resulting values were extremely small. Thus a_2 is fixed at zero for temperatures above T^* to reduce fitting noise in other parameters [2]. This is equivalent to fitting

---

[2] Note that this T^* is different from T_{NA} (bulk) and is determined differently from the T^* values

the high temperature data with the pure 8CB line shape.

It is interesting to note that the LC^2 contribution to the scattering peak resembles a genuine smectic ordering peak in many ways. Figure 5-15 shows a slight increase in q_0 on cooling 8CB + aerosil samples at low temperatures, much like the behavior seen below T_{NA} in bulk 8CB.

Figure 5-16 shows the behavior of σ_1 as a function of temperature for one typical sample. In general σ_1 grows on cooling at high temperatures and settles down at a constant value at low temperatures albeit with some noise.

One of the difficulties with the fitting procedure was the insensitivity of the quality of the fits to variations in σ_1 when T is near T^* for low density samples. This property comes from the strong coupling between the σ_1 and $\xi_\|$ parameters. When the LC^2 portion is almost resolution limited for the small ρ samples, unless there are very good statistics, the uncertainty in $\xi_\|$ is large, and this uncertainty propagates to σ_1 as well. Thus these two parameters can not be determined with great accuracy. Away from T^*, when the sharp static fluctuation peak grows in size, LC^2 has enough statistics to overcome this difficulty. Therefore, the χ^2 surface as a function of σ_1 shows a very broad minimum near T^* and a relatively well defined minimum when $T \ll T^*$. In the case of high density samples, LC^2 is broad, and correlation lengths and consequently σ_1 are relatively well determined.

Figure 5-17 illustrates the evolution of the χ^2 surface as the temperature is decreased when σ_1 has a fixed value that has been stepped over a wide range. The dotted curve which corresponds to a temperature close to T^* has a shallow minimum, and σ_1 cannot be determined with great precision. As the temperature is decreased, a relatively well defined minimum (which corresponds to $LC + LC^2$ minimum) appears and σ_1 is much better determined.

To obtain better fit parameters from the low temperature ($T < T^*$) data, we used the fact that σ_1 is basically due to thermal fluctuations and its temperature dependence can only be proportional to $k_B T$. In the temperature range of interest (T^* to $T^* - \sim 15$ K), the variation of σ_1 is expected to be less than 5% because the

---

used for 8CB + aerogel X-ray scattering measurements (see Eqs. 5.1 and 5.2 in section 5.4.1).

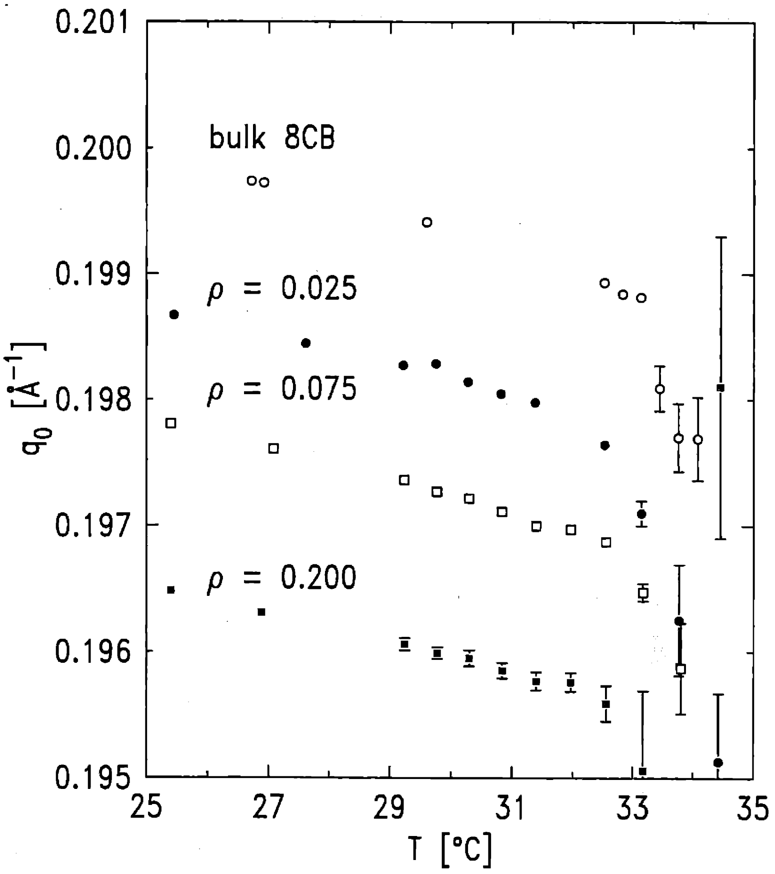

Figure 5-15: Temperature Dependence of q_0

q_0 values for three 8CB + aerosil samples are compared with those for bulk 8CB as a function of temperature. The temperature dependence above T^* is unclear due to broad weak peaks to result in considerable scatter. As the temperature decreases below T^*, q_0 of all 8CB + aerosil samples follow the same pattern as bulk 8CB. As the temperature decreased, q_0 increases slightly as the smectic layer spacing d becomes smaller. The bulk 8CB data was analyzed with $LC + \delta(q)$ line shape to find q_0. q_0 values of 8CB + aerosil samples are reduced by 0.001, 0.002, and 0.003 Å^{-1} for ρ = 0.025, 0.075, and 0.200 g/cm^3 samples, respectively, in order to avoid confusing overlap and provide easy viewing.

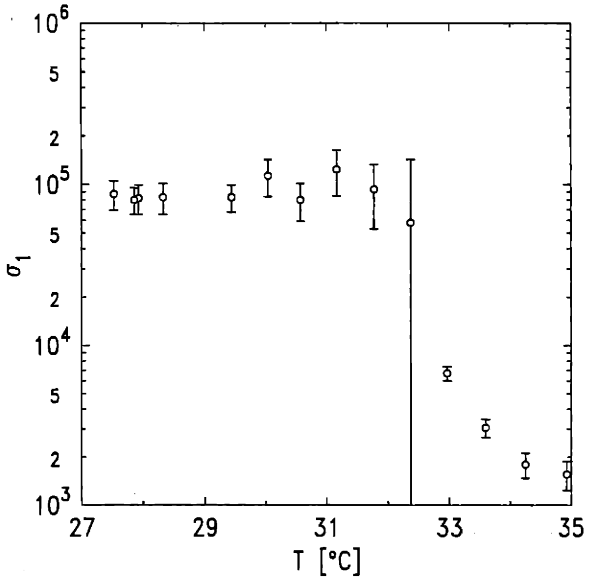

Figure 5-16: Behavior of σ_1
The data were taken from fits of the $\rho = 0.150$ g/cm^3 sample with the $LC + LC^2 + bg$ line shape with σ_1 allowed to vary freely at all temperatures. Note that σ_1 is roughly constant for the low temperature region.

absolute temperature was roughly 300 K. Furthermore, when σ_1 was taken to be a freely adjustable parameter in the range T^* to $\sim (T^* - 15K)$ the resulting σ_1 values were usually clustered around a common value and any "noise" in the σ_1 values was due to fitting problems since there was a strong correlation between odd (high or low) σ_1 values and odd values in the associated $\xi_{\|}$ values. Thus σ_1 was held fixed at a constant value for fits at $T < T^*$. Usually this constant σ_1 was decided by averaging several free low temperature σ_1 values. In a few cases where the low temperature data did not yield a reasonably narrow minimum in χ^2, σ_1 was determined from the best visual estimate of the left edge of the minimum in the χ^2 surface in plots like figure 5-17 . It should be remembered that correlation lengths thus obtained have much a bigger error bar because σ_1 in fact has a large uncertainty.

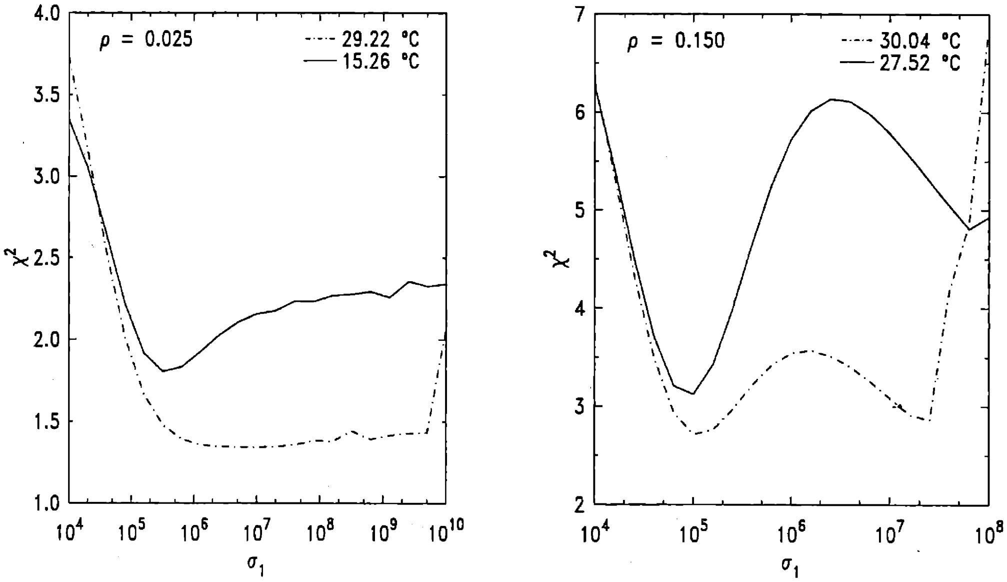

(a) (b)

Figure 5-17: χ^2 Surface
(a) The curves shown are χ^2 surfaces for the $\rho = 0.025$ g/cm^3 sample at $T = 29.22$ and 15.26 °C. When T is close to T^*, this low density sample has a very shallow χ^2 minimum, which evolves into a narrower and well-defined minimum when $T \ll T^*$. (b) χ^2 surfaces for the $\rho = 0.150$ g/cm^3 sample at $T = 30.04$ and 27.52 °C. At low temperatures, this high density sample has a deep χ^2 minimum that corresponds to the $LC + LC^2$ line shape with the LC^2 contribution dominant. The other minimum at high σ_1 corresponds to the LC line shape only (i.e. a_2 is very small). Due to the difference in the depths of two minima, the low σ_1 minimum is statistically significant at this temperature. When the temperature is close to T^*, the two minima have comparable χ^2 values but starting fits from the low temperature values of the parameters, the least-squares program always converges on the low σ_1 minimum.

Chapter 6

Effect of Aerosil Random Disorder

6.1 Finite Correlation Lengths

Figure 6-1 shows the evolution of the parallel correlation lengths for a few of the samples as a function of temperature. One of the most intriguing results, which can be readily seen from this plot, is that the correlation lengths vary rapidly with T at high temperatures and then plateau at a constant value for low temperatures . This behavior is dramatically different from that of 8CB + aerogels where the correlation length grows monotonically as the temperature decreases. However, the results are very similar to that of LC + millipore samples in which liquid crystals are confined in randomly interconnected voids. However, the plateau values of the parallel correlation length ($\xi_{\parallel}$) for 8CB + aerosils far exceed the corresponding mean void size (l_0) of each sample, while in the case of millipore the correlation lengths are restricted by the average pore size [60].

Very high density 8CB + aerosil samples exhibit a somewhat different behavior. The increase on cooling in the correlation length near T^* is more gradual than that for low density samples, and this increase happens over an extended region of temperature as shown for the $\rho = 0.295$ g/cm^3 sample in figure 6-2. This clearly shows the severe smearing of the "transition" for high density samples. Indeed, it is difficult to choose good T^* values for the highest density aerosil samples.

The behavior of the correlation lengths will be discussed in three separate tem-

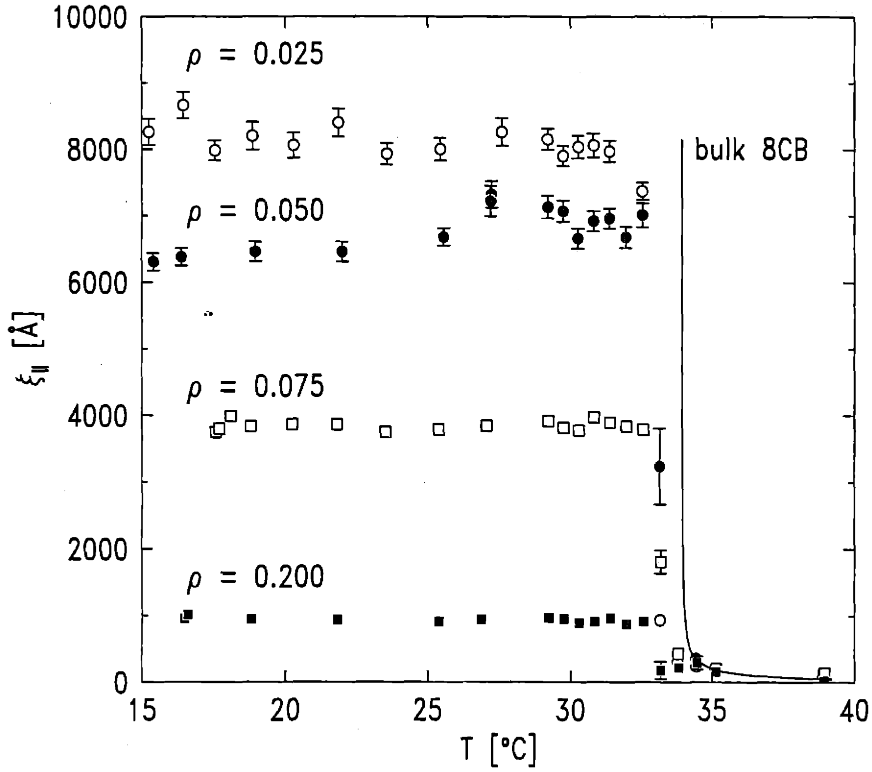

Figure 6-1: Development of $\xi_{\parallel}$
Shown in the figure are the parallel correlation lengths for $\rho = 0.025$, 0.040, 0.075, and 0.200 g/cm^3 samples. $\xi_{\parallel}$ increases rapidly above T^* on cooling and saturates at an effectively constant value below T^*.

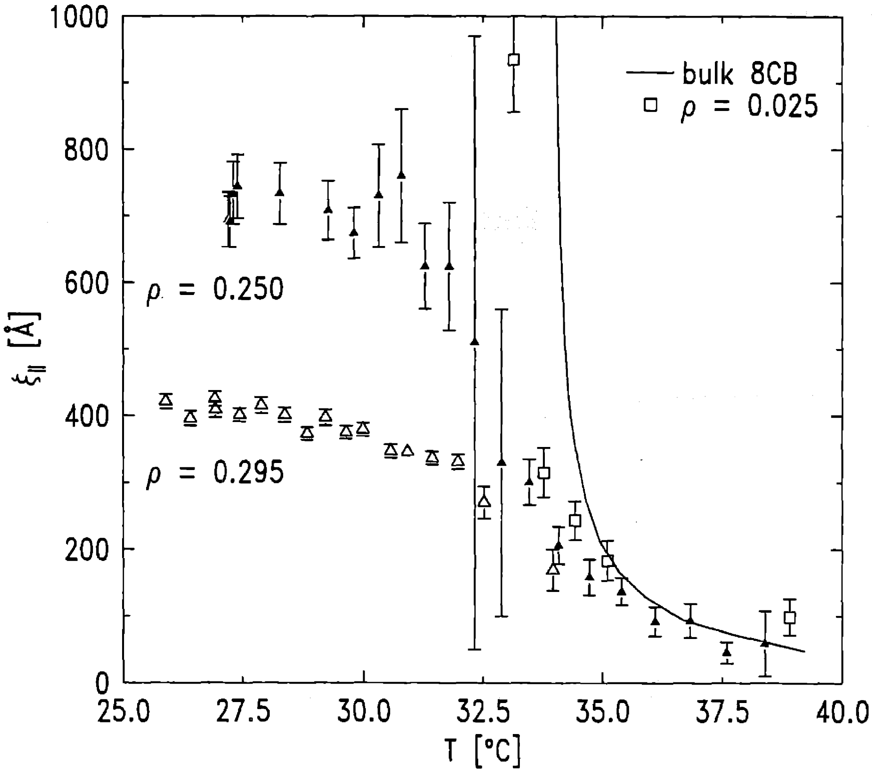

Figure 6-2: Development of Correlation Length

$\xi_{\parallel}(T)$ values for two high density samples with $\rho = 0.250$ and 0.295 g/cm^3 are compared with the $\rho = 0.025$ g/cm^3 sample and bulk 8CB in this figure. Compared with the rapid rise of correlation length of the low density sample and the bulk at high temperatures, high density samples (especially $\rho = 0.295$ g/cm^3) show a slower increase of $\xi_{\parallel}$ over more extended temperature region.

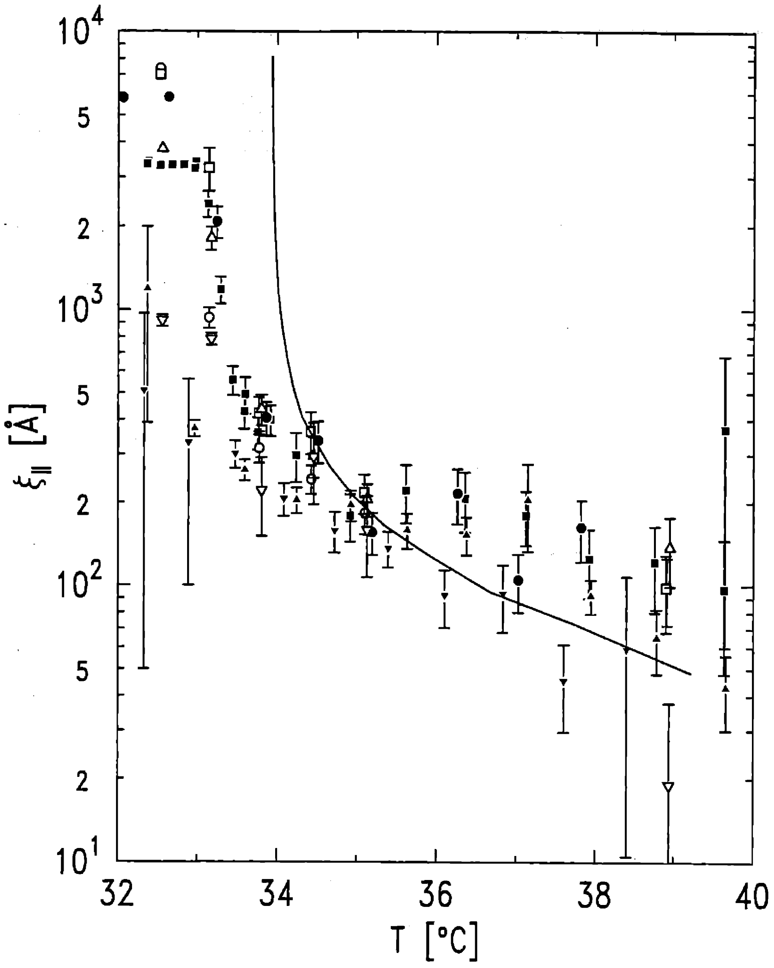

Figure 6-3: High Temperature ($T > T^*$) Correlation Length
Bulk 8CB data (—) taken from ref [46] is compared to 8CB + aerosil samples. Plotted are parallel correlation lengths of various samples: ρ = 0.025 (○), 0.040 (□), 0.050 (●), 0.075 (△), 0.100 (■), 0.150 (▲), 0.200 (▽), and 0.250 g/cm^3 (▼). No adjustment has been made for possible shifts in T^* as a function of ρ [11].

perature regimes, i.e., $T > T^*$, $T \sim T^*$, and $T < T*$.

When the temperature is far above T^*, the correlation lengths are expected to be smaller than the mean void size, l_0. Thus it is natural that they should behave just like the correlation lengths of bulk 8CB as a function of temperature. The observed high temperature behavior is consistent with this interpretation. Figure 6-3 illustrates this point by comparing correlation lengths for many 8CB + aerosil samples at high temperatures .

The correlation lengths increase markedly as the temperature is decreased toward

T^* (which is near the bulk 8CB transition temperature). The rate of increase on cooling just above T^* is, as can be seen from this figure, faster for the low density samples and slower for the high density samples. This result is consistent with sharp and smeared heat capacity peaks for low and high density samples obtained from the calorimetry experiment [11].

When the temperature was brought below T^*, the correlation lengths saturate, although it should be noted that the parallel correlation length at low temperatures, $\xi_{\|}^{\mathrm{LT}}$, is much longer than the mean void size l_0. This low temperature saturation plateau behavior indicates that there is no development into long range order even if the temperature is lowered appreciably below T^*.

Figure 6-4 summarizes the low-temperature plateau values of the correlation lengths, $\xi_{\|}^{LT}$ and $\xi_{\perp}^{LT}$, as a function of silica density.

The nematic correlation length of the homolog 6CB with dispersed aerosil measured with static light scattering demonstrates the formation of very large but finite nematic domains [12]. Because the smectic ordering is expected to be bounded by the nematic domain size, a $\xi_{\|}^{LT}$ which is much smaller relative to this domain size indicates that the aerosil network not only restricts the nematic domains but also disrupts the smectic ordering within such domains, consistent with theory. Note that the aerogel and aerosil systems with equivalent densities of silica have different ξ values. Thus, the partial annealing of the aerosil disorder is a significant feature in contrast to the strongly quenched aerogel disorder.

Nevertheless, $\xi_{\|}^{LT}$ values are about four times larger than l_0 independent of the density as shown in figure 6-5. This is in contrast to 8CB + aerogels, where the correlation lengths were comparable to the void sizes: $\xi^{LT}/L \simeq 2$ for the $\rho = 0.08$ aerogel and $\xi^{LT}/L \simeq 1$ for the other three aerogel samples [28]. This indicates that aerosil systems have much weaker disordering fields than aerogel systems.

The large magnitude of $\xi_{\|}^{LT}$ for the low density samples also provides an explanation for the sharp heat capacity peak. Although there is no transition to true long range order (i.e., no resolution limited SmA peak), such long-correlation-length fluctuations to all intents and purposes mimic the true singular behavior for calorimetry

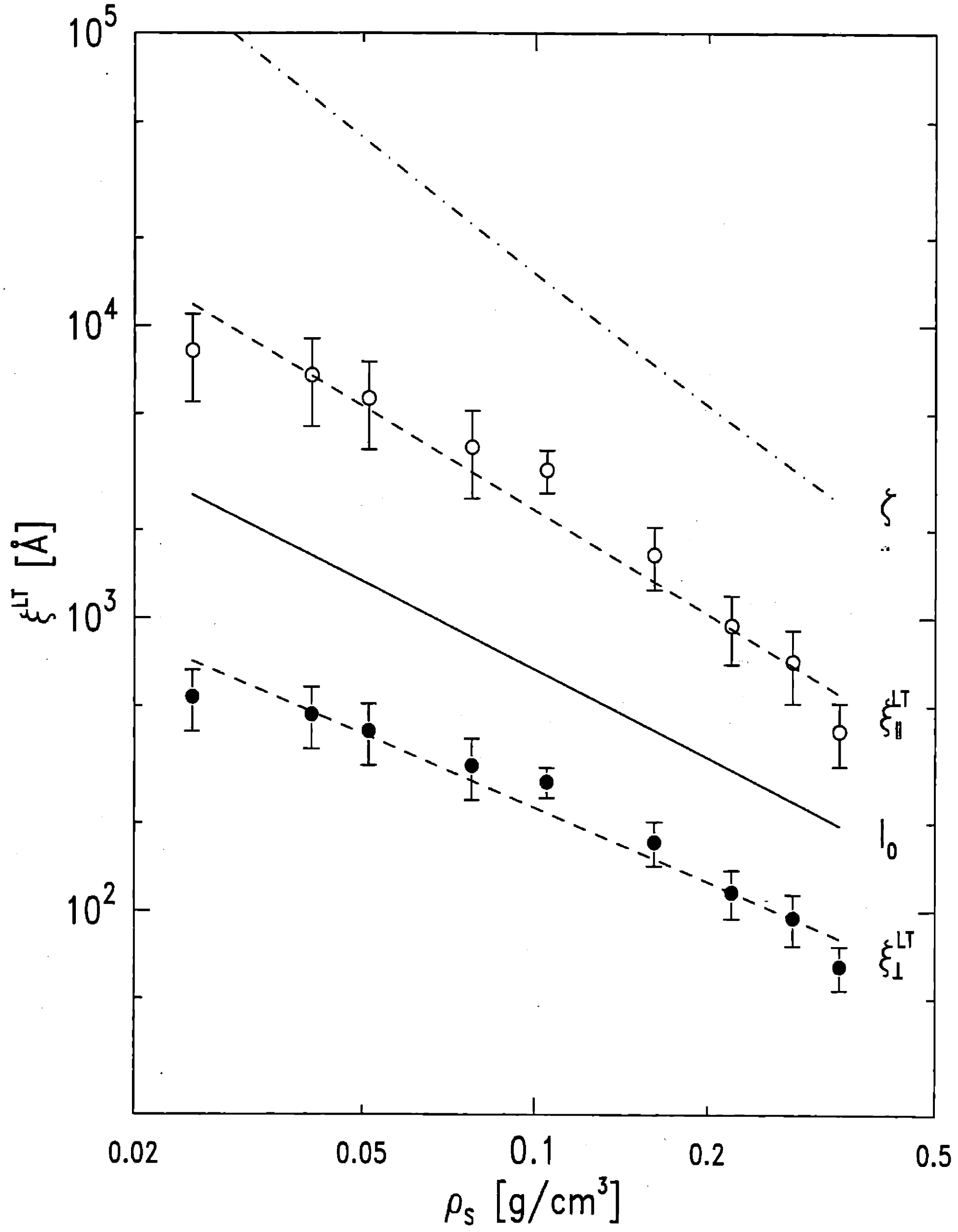

Figure 6-4: Low Temperature Correlation Lengths vs Silica Density
Low temperature correlation lengths ($\xi_{\parallel}^{LT}$ and $\xi_{\perp}^{LT}$) are compared with 6CB + aerosil nematic correlation lengths (ζ) taken from Bellini *et al.* [12] and the mean void size $l_0 = 2/a\rho_S$ as defined in reference [11].

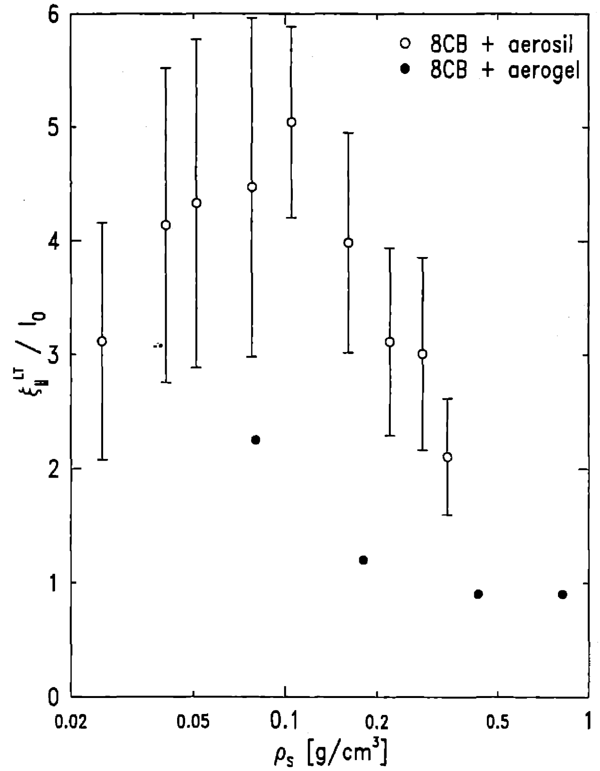

Figure 6-5: $\xi_{\parallel}^{LT}/l_0$

The ratio of the low temperature correlation length ($\xi_{\parallel}^{LT}$) to the mean void size $l_0 = 2/a\rho_S$ is considerably higher for 8CB + aerosil gels (open circles, ○) than for 8CB + aerogels (filled circles, ●). The aerogel data were taken from Clark *et al.* [3], and the filled circles represent ξ/L, where L is an experimental pore chord length.

measurements with finite temperature resolution except for finite size effects at very small reduced temperatures where ΔC_p is truncated when $\xi_{\parallel} = l_0$. [61].

Below the lower critical dimension, ξ is expected to have a simple algebraic dependence on the random field. In figure 6-4, the low temperature correlation lengths are fit with simple power laws (dotted lines): $\xi_{\parallel}^{LT} \sim \rho_S^{-1.2\pm0.2}$ and $\xi_{\perp}^{LT} \sim \rho_S^{-0.8\pm0.2}$. Gingras and Huse [62] estimated the correlation length of the RFXYM at the transition temperature of the XY model to be $\xi \sim H_{RF}^{-2/(2-\eta)}$, where H_{RF} is the random field strength and η is the usual critical exponent for the spatial decay of the correlations of the pure XY model. Since $2-\eta = \gamma/\nu$, $-2/(2-\eta) = -1.02$ and -1.0 for 3D-XY and tricritical, respectively. The empirical power laws are also compatible with one of the predictions of the Radzihovsky-Toner theory: $\xi \sim \Delta_h^{-1}$. However, it should be noted that our $\xi_{\parallel}$ values do not exhibit the temperature dependence expected from RT theory, where ξ is expected to vary as $B(T)^{1/\Gamma}$.

6.2 Crossover From Tricritical To 3D-XY Behavior

The integrated intensities of the static fluctuations, a_2 of the LC^2 term, exhibits order parameter-like growth, as shown in section 5.4.6. Power-law fitting of a_2 with Eq. 5.13 was restricted to the effective reduced temperature range of $t^* \equiv |1-(T/T^*)| < 2.8 \times 10^{-2}$. Figure 5-14 shows a_2 fits for three different samples with densities $\rho = 0.025, 0.150$, and 0.295 g/cm^3, respectively, and figure 6-6 summarizes the exponents x obtained from such fits on all samples.

Since a_2 becomes the intensity of the smectic Bragg peak in the limit of $\rho_S \to 0$, the exponent x is equivalent to the critical exponent, 2β, for the smectic order parameter squared, $\langle|\Psi|^2\rangle$ in this limit. Integrated X-ray scattering intensity measurements on a series of pure liquid crystals by Chan *et al.* show that the effective power-law exponent x^* in the expression Intensity $\sim |t|^{x^*}$ for $T < T_{NA}$ and $T > T_{NA}$ does not follow the simple behavior, $x^* = 1-\alpha$, which is expected as a consequence of the

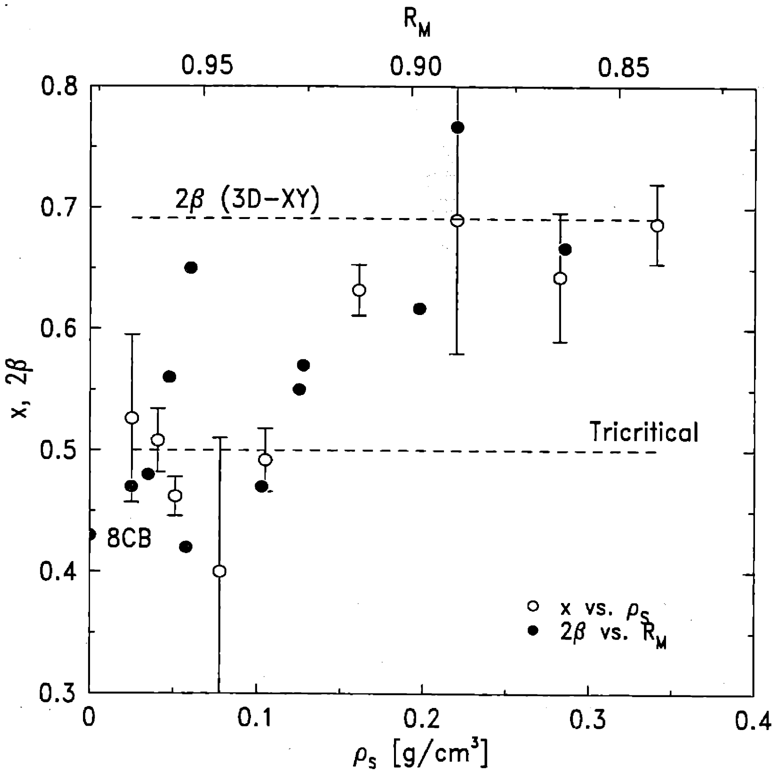

Figure 6-6: Effective Critical Exponent, x

The open circles (○) are the effective critical exponent x obtained from fitting a_2 with the power law 5.13 for each 8CB + aerosil sample. The filled circles (•) represent 2β values for bulk liquid crystals calculated using the Rushbrooke equality with the α and γ values taken from reference [29] with the McMillan ratio $R_M \equiv T_{NA}/T_{NI}$ as the horizontal axis. This horizontal axis was scaled so that the 8CB McMillan ratio of 0.977 corresponds to $\rho_S = 0$. The filled circle located at $(\rho_S = 0, 2\beta = 0.43)$ corresponds to the pure 8CB value.

The exponent x shows a crossover like that seen for 2β in pure liquid crystals from an 8CB 2β value (0.43) or tricritical 2β value (0.5) to the $2\beta = 0.694$ value of 3D-XY. For 8CB + aerosils, this crossover occurs as the silica density of the sample increases; pure liquid crystals show the same type of crossover in 2β as the McMillan ratio decreases.

Landau-de Gennes free energy, but rather an empirical rule, $x^* \approx (\nu_{\parallel} + \nu_{\perp})/2$ [63]. Since in our samples the transition is destroyed by the aerosil, leading to finite $\xi_{\parallel}$ and $\xi_{\perp}$ values, and because of the significant scatter in our results for high temperatures, it was not possible to obtain effective exponents $\nu_{\parallel}$ and $\nu_{\perp}$ for the 8CB + aerosil samples. Thus it is not possible to test whether x is related to $(\nu_{\parallel} + \nu_{\perp})/2$ for aerosil samples. However, if we associate x with 2β, the canonical critical exponent for the order parameter squared, its trend fits very well with that of 2β for pure liquid crystals as a function of nematic range. (The 2β values for pure liquid crystals are calculated using the Rushbrooke equality, $2\beta = 2 - \alpha - \gamma$, with α and γ values taken from reference [29]). The filled circles (●) in figure 6-6 represent 2β values for pure liquid crystals as a function of the McMillan ratio ($R_M \equiv T_{NA}/T_{NI}$) given by the upper horizontal axis. Since pure bulk 8CB has $R_M = 0.977$, the R_M scale starts from 0.977 where $\rho_S = 0$ g/cm^3 and decreases as ρ_S increases. The open circles are the results for 8CB + aerosil samples. Both the pure liquid crystals as a function of nematic range and the 8CB + aerosil samples as a function of disorder strength ρ_S show a trend from near-tricritical to 3D-XY.

This crossover from 8CB-like (or roughly tricritical) behavior to 3D-XY criticality also manifests itself in the calorimetry measurements of 8CB + aerosil samples, where the effective heat capacity critical exponent α decreased from the bulk 8CB value of 0.31 to -0.02, a value close to that of 3D-XY α, -0.007, as silica density increased [11].

The observed crossover from tricritical to 3D-XY may be explained by the reduction of nematic director fluctuations by giving away fluctuation energy to aerosil strands. The coupling between the nematic director fluctuations and the smectic order parameter, which is one of the reasons why there is a crossover from 3D-XY to tricritical behavior for pure liquid crystals, is affected by reduced director fluctuations. The enhancement of orientational order at just below T^* is reduced for high density aerosil samples in this scenario, and the NMR results of Jin and Finotello [14] confirms this.

6.3 X-ray Absorption and Normalization of Fit Parameters

As previously stated, although the different aerosil samples were placed in identical sample environments, the samples had different thicknesses due to their differences in rigidity. Comparing absolute scattering intensities thus becomes difficult. It is, therefore, important to devise a method to work around this problem in order to put the different samples on the same arbitrary intensity scale for appropriate comparison.

The major impact of different sample thickness to the scattered intensity is through the X-ray absorption. For an ideal homogeneous slab of sample, the scattered intensity is dependent on the thickness as

$$I \sim d e^{-d/\lambda}, \tag{6.1}$$

where I is the scattered intensity, d is the thickness of the sample, and λ is the X-ray attenuation length. Note that λ is a function of the silica density because silica and the liquid crystal have different absorption coefficients. At 8 keV, the X-ray attenuation length of silica is $\lambda_{\mathrm{SiO_2}} = 130\ \mu\mathrm{m}$ and that of 8CB is $\lambda_{\mathrm{8CB}} = 2400\ \mu\mathrm{m}$. The X-ray attenuation length of each 8CB+aerosil sample can be calculated from the following formula using the two attenuation lengths:

$$\frac{1}{\lambda} = \frac{\Phi_{\mathrm{SiO_2}}}{\lambda_{\mathrm{SiO_2}}} + \frac{\Phi_{\mathrm{8CB}}}{\lambda_{\mathrm{8CB}}}, \tag{6.2}$$

where $\Phi_{\mathrm{SiO_2}}$ and Φ_{8CB} are the silica and the 8CB volume fraction respectively. In Table A.1, λ for each sample calculated using the formula given above is listed.

Fortunately, the background scans made at a high temperature give us a valuable clue as to how normalize the scattering intensity from different samples. Background scans are composed primarily from the scattering from the silica, with non-negligible amounts of scattering from the liquid 8CB at high q as well. Therefore, the background scattering intensity can be written as

$$B(q) = a_S S_S(q) + a_{LC} S_{LC}(q) \tag{6.3}$$

where a_S and a_{LC} are sample density and thickness dependent coefficients and $S_S(q)$ and $S_{LC}(q)$ are the scattering profiles of the silica and the liquid crystal respectively.

S_{LC} is measured by the bulk 8CB scans at temperatures above T_{NI} and $S_S(q)$ can be obtained by power law fits of small-q scattering data for aerosil samples. It was found that $S_S(q) \propto q^{-3.55}$ when 0.05 Å$^{-1} < q < 0.10$ Å^{-1}. Thus a_S and a_{LC} values can be obtained by fitting high temperature background scans as described below.

Because a_S is proportional to the amount of silica present in the sample while a_{LC} is proportional to the amount of the liquid crystal and both are affected by absorption through the same attenuation coefficient, they can be written as

$$a_S \propto \Phi_{\mathrm{SiO_2}}\, d\, e^{-\frac{d}{\lambda}} \tag{6.4}$$

$$a_{LC} \propto \Phi_{\mathrm{LC}}\, d\, e^{-\frac{d}{\lambda}}, \tag{6.5}$$

where d is the sample thickness. Therefore, we obtain the following simple relation between the two coefficients:

$$\frac{a_S}{a_{LC}} \propto \frac{\Phi_{\mathrm{SiO_2}}}{\Phi_{\mathrm{LC}}}. \tag{6.6}$$

The validity of equation 6.6 can be verified through a log-log plot of the ratio a_S/a_{LC} vs. $\Phi_{\mathrm{SiO_2}}/\Phi_{\mathrm{LC}}$, as shown in figure 6-7. As expected, the data points nicely follow a line of slope one in this figure.

Note that S_{LC} contains contributions from the smectic fluctuations below T_{NI}. Thus the scattering profile we observe can be normalized by dividing by a_{LC}.

One such attempt is shown in figures 6-8 and 6-9. When normalized properly, the low-temperature "plateau" σ_1 values are approximately constant for $\rho_S < 0.1$ g/cm^3 and decrease as the density increases for $\rho_S > 0.1$ g/cm^3. Due to some ambiguity involved in determining the low temperature σ_1 values as discussed in section 5.4.6, the behavior in this figure is not completely certain.

Since a_2 shows order-parameter-like growth as a function of $|T - T^*|$ below T^*

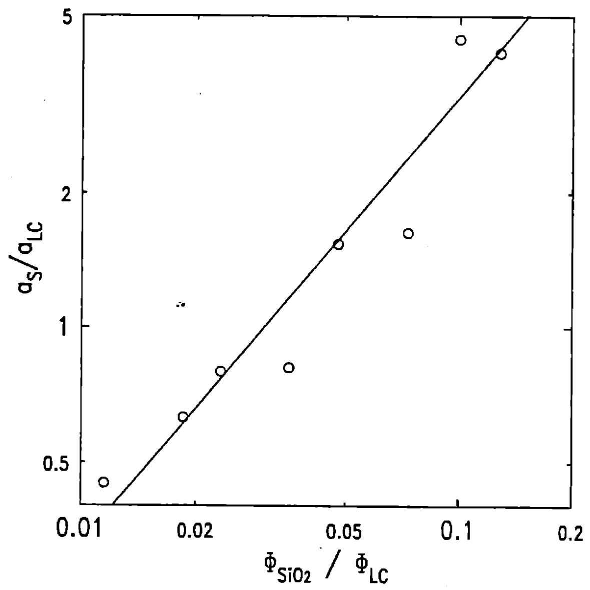

Figure 6-7: a_S/a_{LC} vs. $\Phi_{\mathrm{SiO_2}}/\Phi_{\mathrm{LC}}$

The open circles corresponds to $\rho = 0.025, 0.040, 0.050, 0.075, 0.100, 0.150, 0.200$, and 0.250 g/cm^3 samples from left (small $\Phi_{\mathrm{SiO_2}}/\Phi_{\mathrm{LC}}$) to right (large $\Phi_{\mathrm{SiO_2}}/\Phi_{\mathrm{LC}}$). If the assumptions about the high temperature background scan (it consists of separable the silica and the LC part) is correct and if adequate scattering profiles, $S_S(q)$ and $S_{LC}(q)$, are used, the points in this plot must lie on a line with unit slope. The solid line (—) shown is a guide line with a slope of unity to demonstrate the validity of our analysis.

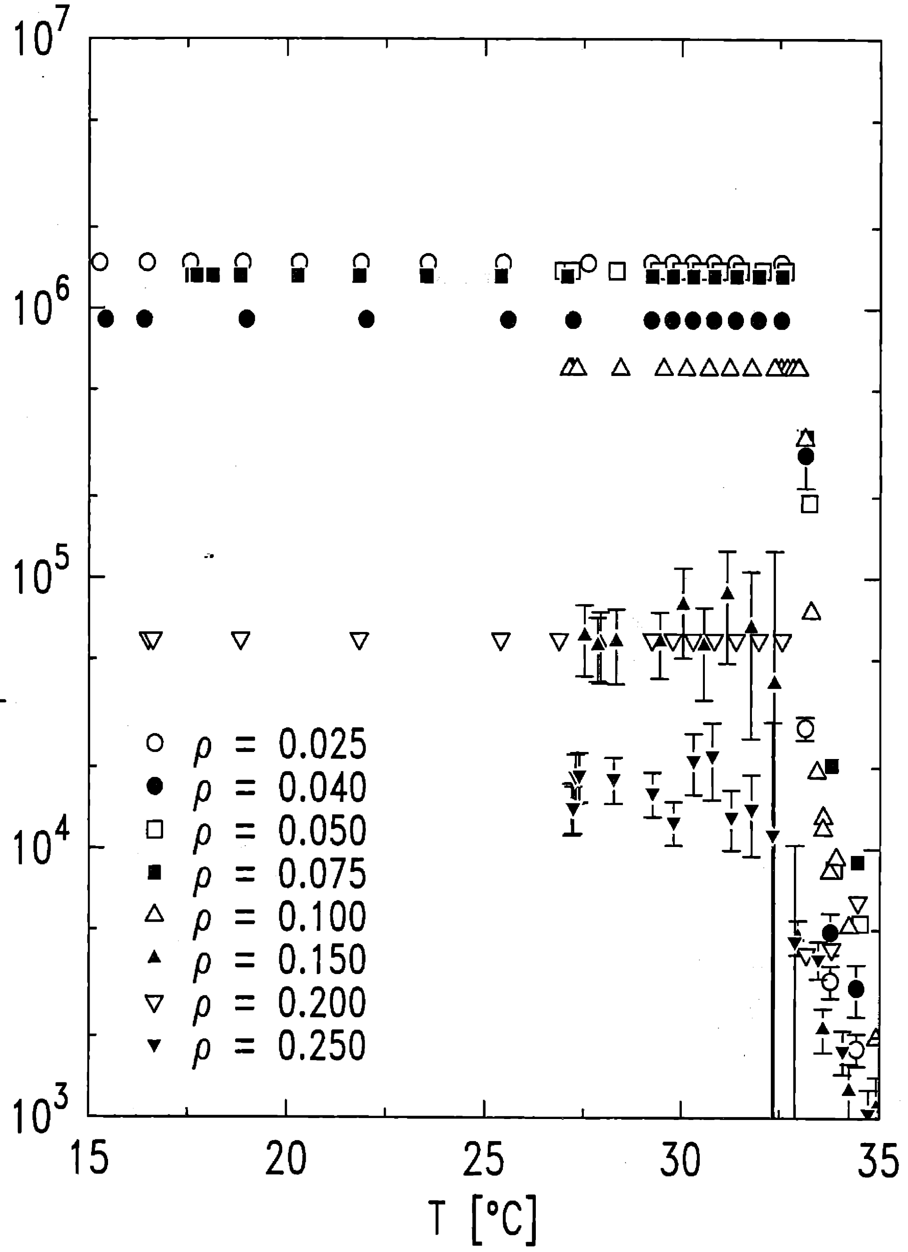

Figure 6-8: σ_1^N vs. T

$\sigma_1^N \equiv \sigma_1/a_{LC}$ designates properly normalized values of σ_1, in terms of which comparison between samples is possible. σ_1^N is temperature independent for low temperatures except perhaps for the highest density sample shown in this figure.

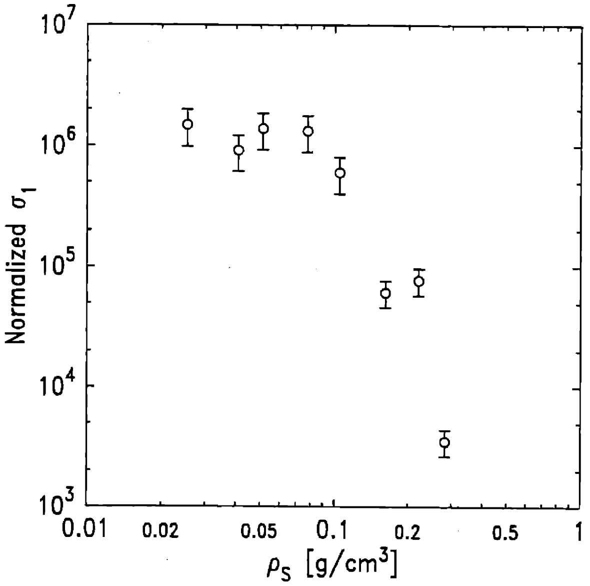

Figure 6-9: Normalized σ_1

When normalized by dividing the low temperature σ_1 values by a_{LC}, $\sigma_1^N (\equiv \sigma_1/a_{LC})$ shows an interesting trend. For low density samples with $\rho_S < 0.1$ g/cm^3, σ_1^N does not show any significant dependence on ρ_S. As the silica density increases above $\rho_S \sim 0.1$ g/cm^3, there is a noticeable decrease in σ_1^N.

with different ρ-dependent exponents, a direct comparison of a_2 for different samples is not simple. It was attempted, however, to compare a normalized a_2 value at the same effective reduced temperature, $t^* \approx 1.0 \times 10^{-2}$. The obtained normalized values were noisy and did not show any systematic trend with ρ, with the values fluctuating within a factor of three. It must be noted that a_2 values were increasing on cooling to the lowest accessible temperature, which is set by crystallization of the samples. This a_2 result may indicate the following. While most of the liquid crystal in the samples contributes to the static fluctuations at low temperatures regardless of silica density (the same normalized a_2 for different samples), there are weaker thermal fluctuations for the high density samples.

Chapter 7

Concluding Remarks

We have investigated the 8CB + aerosil system using X-ray diffraction methods to study the effect of quenched randomness on the nematic to smectic-A transition. There are several important points we have uncovered from the scattering measurements.

- The high temperature scattering was very similar to that from the thermal fluctuations of bulk 8CB, a fact indicative of weak quenched randomness. The measured scattering profile could be fit with the powder average of the bulk 8CB critical scattering line shape, i.e., LFC with $\xi_\perp$ and c determined from the $\xi_\parallel$ values using the bulk relations between them (LC line shape):

  $$S(\mathbf{q}) = \frac{\sigma_1}{1 + \xi_\parallel^2 (q_\parallel - q_0)^2 + \xi_\perp^2 q_\perp^2 + c^2 \xi_\perp^4 q_\perp^4}. \tag{7.1}$$

  Therefore, the above line shape has only 3 adjustable parameters: q_0, σ_1, and $\xi_\parallel$ (plus of course the background coefficient b).

- The low temperature scattering required the use of an additional term. We added the square of the thermal fluctuation term with an independent amplitude to describe the static fluctuations originating from quenched randomness. Thus the low temperature line shape was taken to be LC + LC^2:

$$S(\mathbf{q}) = \frac{\sigma_1}{1+\xi_{\parallel}^2(q_{\parallel}-q_0)^2+\xi_{\perp}^2 q_{\perp}^2+c^2\xi_{\perp}^4 q_{\perp}^4} + \frac{a_2\xi_{\parallel}\xi_{\perp}^2}{\left(1+\xi_{\parallel}^2(q_{\parallel}-q_0)^2+\xi_{\perp}^2 q_{\perp}^2+c^2\xi_{\perp}^4 q_{\perp}^4\right)^2}. \tag{7.2}$$

a_2 is the only additional adjustable parameter, thus there are only 4 adjustable parameters in the above line shape (plus the background b coefficient).

- No line shape was resolution limited at any temperature or density of aerosil, unlike the bulk 8CB peak, indicating the destruction of the quasi-long range order of the smectic-A phase as predicted by various theories.

- The anisotropic correlation lengths grew as T decreased toward T^* from above. They stopped growing below T* and were almost constant over a wide temperature region with density dependent values of $\xi_{\parallel}^{\mathrm{LT}}$ and $\xi_{\perp}^{\mathrm{LT}}$.

- The longitudinal correlation lengths at low temperatures, $\xi_{\parallel}^{\mathrm{LT}}$, are believed to be long enough to account for the observed sharp heat capacity peak (pseudo N-SmA transition) for low density samples [61].

- Integrated intensity of the static fluctuation term, a_2, behaves like a smectic order parameter squared, $\langle|\Psi|^2\rangle$, and could be fit with a power law:

$$a_2 \propto |T^* - T|^x . \tag{7.3}$$

  Equating x with 2β, it exhibits crossover from 8CB or near-tricritical values to 3D-XY values as the silica density increased, a behavior consistent with the calorimetry results which showed similar crossover for the effective heat capacity critical exponent α.

Preliminary X-ray scattering experiments on $\overline{8}$S5 + aerosil system showed quite interesting behavior in contrast to the 8CB + aerosil system. $\overline{8}$S5 + aerosil had almost resolution limited line shapes if not completely resolution limited. This is not surprising considering the fact that $\overline{8}$S5 is non-polar (hydrocarbon tails at both ends) and interacts with silica network differently. Most likely the anchoring force is much weaker for $\bar{8}$S5. This indicates that the strength of disorder in LC + aerosil systems is dependent on the individual liquid crystalline molecules as well as the silica density. Hence, with a variety of liquid crystals available, LC + aerosil systems, can be studied over a wide range of disorder.

In conclusion, this thesis has shown that 8CB with dispersed silica particles provides a model random field system for studying a transition that breaks a continuous symmetry. These findings have already stimulated other experimental efforts on different LC + aerosil systems including but not limited to liquid crystals with a smectic-A to smectic-C transitions or a re-entrant nematic phase (i.e., N-SmA-N sequence on cooling).

Appendix A

Tables of Results

The fit results are tabulated in this section. The units of temperature (T), correlation lengths ($\xi_{\parallel}, \xi_{\perp}$), and center of the peak (q_0) are °C, Å, and Å^{-1} respectively. The corresponding error of the parameters uses the same unit. The σ_1 values in tables A.3-A.11 are in arbitrary units, and since absolute σ_1 values are dependent upon individual experimental setup details, σ_1 values for different samples should not be compared directly with each other. Though the intensity of the LC^2 term a_2 has the dimension of Å^{-3}, like σ_1, its values for different samples should not be compared. Normalized values of σ_1 and a_2 can be obtained using the factor a_{LC} given in table A.1, and low-temperature plateau values of $\sigma_1^N (\equiv \sigma_1/a_{LC})$ are given in table A.2.

In tables A.3 - A.11, $\xi_{\perp}$ is not a freely adjustable parameter as explained in section 5.4.5.

Table A.1: Table of ρ, ρ_S, $\Phi_{\mathrm{SiO_2}}$, and the X-ray attenuation length λ.

ρ is in g of SiO_2 /cm^3, and ρ_S is grams of SiO_2 per cm^3 of LC. The volume fraction of silica $\Phi_{\mathrm{SiO_2}}$ is dimensionless. The last column is a_{LC}, the normalization coefficient discussed in section 6.3.

ρ	ρ_S	$\Phi_{\mathrm{SiO_2}}$	λ (μm)	a_{LC}
0.025	0.0253	0.0114	2020	0.675
0.040	0.0407	0.0182	1830	0.759
0.050	0.0512	0.0227	1730	0.231
0.075	0.0776	0.0341	1510	0.106
0.100	0.105	0.0455	1340	0.167
0.150	0.161	0.0682	1100	1.42
0.200	0.220	0.0909	930	0.0270
0.250	0.282	0.114	806	0.881
0.295	0.341	0.134	720	

Table A.2: Best Choices for the Constant Low-Temperature Amplitudes of the LC Terms

The values in parenthesis indicate average values for σ_1 at low enough temperatures. Rather than fixing σ_1 at a constant, it was allowed to vary freely because its scatter was not severe. The quantity σ_1^N is the normalized value σ_1/a_{LC}.

Sample (ρ in g/cm^3)	σ_1	σ_1^N
0.025	1.0×10^6	1.5×10^6
0.040	6.9×10^5	9.1×10^5
0.050	3.2×10^5	1.4×10^6
0.075	1.4×10^5	1.3×10^6
0.100	1.0×10^5	6.0×10^5
0.150	(83000)	6.1×10^4
0.200	1600	7.7×10^4
0.250	(14200)	3.5×10^3
0.295	7500	

Table A.3: $\rho = 0.025$ g/cm^3

T	σ_1	$\sigma_{1,err}$	a_2	$a_{2,err}$	$\xi_{\parallel}$	$\xi_{\parallel,err}$	$\xi_{\perp}$	$\xi_{\perp,err}$	q_0	$q_{0,err}$
14.618	1e+06	0	0.03416	0.00026	8420	110	545.625	4.81239	0.20019	5.8e-06
15.258	1e+06	0	0.03362	0.00049	8260	200	538.284	8.95524	0.200326	1.1e-05
16.459	1e+06	0	0.03263	0.00041	8660	200	556.277	9.13532	0.200249	9.7e-06
17.559	1e+06	0	0.03136	0.00041	7980	150	524.929	7.12732	0.200186	9.9e-06
18.880	1e+06	0	0.03155	0.00052	8200	210	535.209	9.7411	0.200115	1.3e-05
20.296	1e+06	0	0.03022	0.00048	8060	190	528.772	8.8259	0.200092	1.2e-05
21.857	1e+06	0	0.03034	0.00046	8400	210	544.469	9.61403	0.199983	1.1e-05
23.564	1e+06	0	0.0284	0.00042	7930	160	522.807	7.39682	0.199832	1.1e-05
25.448	1e+06	0	0.0268	0.00043	8000	170	525.807	8.09916	0.199669	1.2e-05
27.603	1e+06	0	0.02183	0.00046	8260	210	538.062	9.63459	0.199444	1.4e-05
29.215	1e+06	0	0.01558	0.00035	8150	160	532.971	7.38883	0.199271	1.4e-05
29.746	1e+06	0	0.01655	0.00037	7900	150	521.34	7.00863	0.199284	1.4e-05
30.272	1e+06	0	0.01575	0.00041	8040	170	528.024	7.72935	0.19914	1.6e-05
30.813	1e+06	0	0.01467	0.00041	8060	180	528.977	8.16001	0.199046	1.7e-05
31.370	1e+06	0	0.01237	0.00036	7970	160	524.767	7.28932	0.198977	1.7e-05
32.530	1e+06	0	0.00563	0.00037	7370	130	496.36	6.19807	0.198642	2.5e-05
33.140	18900	2700	0	0	935	79	115.232	6.84852	0.198097	9.9e-05
33.772	2180	440	0	0	315	37	53.4559	4.31498	0.19725	0.00044
34.426	1220	250	0	0	243	29	44.3995	3.74264	0.19613	0.00054
35.103	680	180	0	0	183	30	36.3681	4.12979	0.19742	0.00093
38.914	141	56	0	0	99	27	23.5004	4.43746	0.1967	0.0024

Table A.4: $\rho = 0.040$ g/cm^3

T	σ_1	$\sigma_{1,err}$	a_2	$a_{2,err}$	$\xi_{\parallel}$	$\xi_{\parallel,err}$	$\xi_{\perp}$	$\xi_{\perp,err}$	q_0	$q_{0,err}$
15.406	690001	0	0.03331	0.00048	6310	130	444.851	6.37026	0.200348	1.2e-05
16.392	690000	0	0.03315	0.00047	6380	130	448.068	6.61609	0.200274	1.2e-05
18.972	690000	0	0.03144	0.00049	6460	150	452.384	7.22815	0.200193	1.2e-05
21.986	690000	0	0.02908	0.0005	6460	150	451.973	7.63915	0.20005	1.3e-05
25.574	690000	0	0.02527	0.00039	6680	130	462.938	6.46533	0.199789	1.1e-05
27.248	690000	0	0.02112	0.00044	7320	200	494.11	9.3954	0.199556	1.5e-05
27.215	690000	0	0.01933	0.00051	7220	230	489.382	10.8045	0.199541	1.9e-05
29.215	690000	0	0.01636	0.00038	7130	170	484.746	8.29757	0.199423	1.6e-05
29.746	690000	0	0.01586	0.00039	7070	160	481.799	7.89653	0.199352	1.6e-05
30.271	690000	0	0.0139	0.00042	6660	150	462.043	7.36033	0.19926	1.9e-05
30.812	690000	0	0.0135	0.00038	6920	150	474.752	7.25497	0.199205	1.8e-05
31.368	690000	0	0.0117	0.00037	6960	150	476.497	7.43684	0.199091	1.9e-05
31.944	690000	0	0.00947	0.00041	6680	160	463.045	7.8197	0.19896	2.4e-05
32.530	690000	0	0.00703	0.00039	7010	180	479.066	8.7121	0.198993	2.8e-05
33.139	218000	71000	0	0	3234.86	569.873	278	33	0.1985	0.00011
33.770	3720	860	0	0	421.222	60.2992	65.9	6.2	0.19713	0.0004
34.422	2310	660	0	0	361.587	62.4413	59	6.9	0.19857	0.00056
35.094	880	230	0	0	216.98	35.7146	41.2	4.5	0.19737	0.00075
38.901	134	57	0	0	98.4087	30.5483	23.7	4.7	0.1939	0.0024

Table A.5: $\rho = 0.050$ g/cm^3

T	σ_1	$\sigma_{1,err}$	a_2	$a_{2,err}$	$\xi_\parallel$	$\xi_{\parallel,err}$	$\xi_\perp$	$\xi_{\perp,err}$	q_0	$q_{0,err}$
26.957	320000	0	0.013	0.00029	5570	110	407.162	5.71691	0.199507	1.4e-05
27.191	320000	0	0.01236	0.00029	5530	110	405.223	5.59765	0.19949	1.4e-05
28.330	320000	0	0.01136	0.00029	5510	110	404.219	5.57091	0.19935	1.5e-05
29.390	320000	0	0.00984	0.00023	5454	93	401.207	4.81156	0.199229	1.3e-05
29.958	320000	0	0.00919	0.0002	5535	85	405.413	4.37691	0.199138	1.2e-05
30.463	320000	0	0.00857	0.00019	5715	90	414.689	4.59485	0.199053	1.3e-05
30.973	320000	0	0.00796	0.00026	5830	130	420.625	6.54517	0.198989	1.8e-05
31.505	320000	0	0.00643	0.00022	5670	100	412.489	5.00557	0.198898	1.7e-05
32.060	320000	0	0.00533	0.00021	5770	110	417.288	5.81941	0.198821	1.9e-05
32.636	320000	0	0.00327	0.00021	5800	120	419.198	5.9428	0.198642	2.5e-05
33.237	44000	10000	0	0	2070	270	202.24	18.2921	0.198005	8.3e-05
33.863	1940	480	0	0	405	56	63.7425	6.17063	0.19883	0.00044
34.515	1220	360	0	0	335	58	55.8112	6.64083	0.19796	0.00062
35.193	281	77	0	0	156	27	32.511	3.86461	0.196	0.0011
36.260	390	150	0	0	216	49	40.852	6.41066	0.1943	0.0012
37.025	116	42	0	0	105	25	24.4932	4.06898	0.1972	0.002
37.818	175	71	0	0	163	41	33.5395	5.74069	0.1968	0.0016

Table A.6: $\rho = 0.075$ g/cm^3

T	σ_1	$\sigma_{1,err}$	a_2	$a_{2,err}$	$\xi_\parallel$	$\xi_{\parallel,err}$	$\xi_\perp$	$\xi_{\perp,err}$	q_0	$q_{0,err}$
17.595	140000	0	0.01495	0.0002	3751	58	307.886	3.35998	0.200234	1.2e-05
17.721	140000	0	0.01499	0.00022	3801	66	310.806	3.78406	0.200189	1.3e-05
18.119	140000	0	0.01529	0.00024	3991	82	321.716	4.63473	0.200146	1.4e-05
18.815	140000	0	0.01466	0.00026	3836	79	312.794	4.55247	0.20014	1.6e-05
20.254	140000	0	0.01322	0.00021	3865	70	314.487	4.00506	0.200156	1.4e-05
21.811	140000	0	0.01239	0.00024	3863	79	314.385	4.50761	0.200047	1.6e-05
23.520	140000	0	0.01218	0.00022	3750	68	307.823	3.94286	0.199945	1.5e-05
25.396	140000	0	0.01112	0.0002	3789	63	310.106	3.62063	0.199806	1.4e-05
27.071	140000	0	0.0104	0.00021	3844	70	313.294	3.99515	0.199607	1.6e-05
29.235	140000	0	0.00863	0.00021	3917	78	317.48	4.43862	0.199362	1.9e-05
29.765	140000	0	0.00721	0.0002	3816	69	311.662	3.96288	0.199269	2e-05
30.292	140000	0	0.00696	0.00023	3777	77	309.411	4.43081	0.199216	2.3e-05
30.833	140000	0	0.00662	0.0002	3974	77	320.735	4.36818	0.199111	2.1e-05
31.394	140000	0	0.00512	0.00018	3895	69	316.193	3.95713	0.198999	2.2e-05
31.965	140000	0	0.00395	0.00017	3840	63	313.055	3.6033	0.198971	2.4e-05
32.557	140000	0	0.00221	0.00017	3788	62	310.008	3.60343	0.198872	3.1e-05
33.169	35500	6100	0	0	1806.43	174.14	184	12	0.198471	6.9e-05
33.801	2160	460	0	0	435.295	55.6974	67.3	5.8	0.19787	0.00036
34.456	950	260	0	0	294.933	49.5859	51.2	5.7	0.19643	0.00062
35.130	510	110	0	0	205.213	28.1574	39.6	3.6	0.19689	0.00066
38.949	130	56	0	0	138.04	38.7615	29.8	5.7	0.2005	0.0019

Table A.7: $\rho = 0.100$ g/cm^3 data from two runs

T	σ_1	$\sigma_{1,err}$	a_2	$a_{2,err}$	$\xi_\parallel$	$\xi_{\parallel,err}$	$\xi_\perp$	$\xi_{\perp,err}$	q_0	$q_{0,err}$
32.384	100000	0	0.00327	0.00017	3397	64	287.059	3.79779	0.198686	2.6e-05
32.528	100000	0	0.00249	0.00016	3296	58	281.009	3.45974	0.198613	2.8e-05
32.678	100000	0	0.00194	0.00016	3313	62	282.024	3.70312	0.198557	3.3e-05
32.826	100000	0	0.00146	0.00015	3323	59	282.627	3.51907	0.198509	3.4e-05
32.977	100000	0	0.00112	0.00015	3401	66	287.31	3.90327	0.198428	4e-05
33.130	55000	11000	0	0	2400	260	224.662	16.7932	0.198289	6.3e-05
33.284	12500	2300	0	0	1180	130	136.3	10.0209	0.19799	0.0001
33.438	3220	620	0	0	556	67	79.848	6.65803	0.19791	0.00021
33.596	2190	520	0	0	493	75	73.3368	7.69605	0.19706	0.00034
33.754	1370	280	0	0	358	48	58.4503	5.45564	0.19766	0.00037
33.916	1540	300	0	0	398	51	63.0511	5.57013	0.19764	0.00031
39.643	320	450	0	0	370	310	59.8522	32.1786	0.1973	0.0051
27.207	100000	0	0.00973	0.00023	3085	54	268.156	3.29302	0.199369	1.7e-05
27.141	100000	0	0.01027	0.00025	3198	62	275.058	3.74941	0.199366	1.7e-05
27.124	100000	0	0.01009	0.00032	3191	81	274.598	4.93477	0.199366	2.3e-05
27.326	100000	0	0.01003	0.00021	3149	51	272.075	3.09381	0.199338	1.5e-05
28.428	100000	0	0.00887	0.00022	3165	56	273.058	3.38657	0.199232	1.7e-05
29.532	100000	0	0.00776	0.0002	3223	54	276.539	3.29577	0.199106	1.7e-05
30.122	100000	0	0.00764	0.00018	3344	55	283.857	3.30547	0.19904	1.6e-05
30.692	100000	0	0.00648	0.0002	3280	62	280.015	3.73363	0.198962	2e-05
31.228	100000	0	0.00534	0.0002	3189	59	274.52	3.56127	0.198876	2.2e-05
31.785	100000	0	0.00436	0.00018	3277	60	279.818	3.63036	0.19874	2.3e-05
32.363	100000	0	0.00317	0.00016	3342	59	283.719	3.56294	0.198635	2.5e-05
32.962	100000	0	0.00073	0.00016	3221	60	276.446	3.63028	0.198425	4.5e-05
33.587	1980	420	0	0	428	59	66.3251	6.35392	0.19765	0.00031
34.237	860	290	0	0	297	60	51.23	7.11998	0.19645	0.00081
34.916	330	100	0	0	179	35	35.8628	4.76945	0.1981	0.0011
35.616	380	150	0	0	221	53	41.5015	6.8907	0.1947	0.0012
36.353	320	130	0	0	207	51	39.6899	6.68646	0.1958	0.0013
37.118	222	81	0	0	180	40	35.9727	5.4619	0.1962	0.0013
37.919	113	49	0	0	125	35	27.8107	5.26894	0.1924	0.0022
38.756	82	44	0	0	122	42	27.2681	6.39424	0.196	0.0028
39.639	42	33	0	0	97	49	23.1822	7.82332	0.1981	0.0048

Table A.8: $\rho = 0.150$ g/cm^3

T	σ_1	$\sigma_{1,err}$	a_2	$a_{2,err}$	$\xi_\parallel$	$\xi_{\parallel,err}$	$\xi_\perp$	$\xi_{\perp,err}$	q_0	$q_{0,err}$
27.525	87000	18000	0.0423	0.0021	1620	110	170.343	7.77738	0.198729	1.6e-05
27.929	82000	17000	0.0405	0.0022	1570	110	166.248	8.21632	0.198716	1.7e-05
27.858	80000	15000	0.041	0.002	1562	95	165.693	7.07886	0.198747	1.5e-05
28.327	83000	18000	0.0378	0.0022	1590	110	167.556	8.37451	0.198668	1.8e-05
29.440	83000	16000	0.032	0.0017	1610	110	168.926	8.46567	0.198518	1.5e-05
30.039	113000	29000	0.0267	0.0021	1800	170	183.187	12.0723	0.198414	1.8e-05
30.576	80000	21000	0.0249	0.0021	1580	150	166.719	11.4014	0.198376	2.1e-05
31.166	124000	39000	0.0169	0.0021	1860	240	187.543	16.7426	0.198279	2e-05
31.775	93000	40000	0.0121	0.0025	1630	290	170.594	21.1476	0.198091	2.7e-05
32.368	58000	85000	0.004	0.0073	1190	800	137.046	59.6131	0.19794	5.3e-05
32.964	6710	690	0	0	371	25	59.9175	2.87128	0.197	0.00019
33.592	3050	400	0	0	263	23	46.967	2.9145	0.19733	0.00034
34.244	1800	320	0	0	204	22	39.2616	2.96896	0.1976	0.00058
34.925	1560	320	0	0	196	25	38.1902	3.3775	0.19756	0.00069
35.632	940	220	0	0	159	23	32.8923	3.34263	0.19594	0.00094
36.374	770	200	0	0	153	24	32.0388	3.48931	0.1969	0.0011
37.143	820	470	0	0	205	72	39.3945	9.37178	0.1994	0.0019
37.943	321	67	0	0	92	13	22.3071	2.25125	0.1979	0.0013
38.780	130	50	0	0	65	17	17.5143	3.10469	0.1956	0.0035
39.657	52	22	0	0	43	13	12.9557	2.78932	0.1775	0.0083

Table A.9: $\rho = 0.200$ g/cm^3

T	σ_1	$\sigma_{1,err}$	a_2	$a_{2,err}$	$\xi_\parallel$	$\xi_{\parallel,err}$	$\xi_\perp$	$\xi_{\perp,err}$	q_0	$q_{0,err}$
16.502	1600	0	0.004239	8.1e-05	959	29	117.369	2.48951	0.200124	3.6e-05
16.617	1600	0	0.004183	8e-05	1015	33	122.191	2.77022	0.200016	3.5e-05
18.830	1600	0	0.004	8.4e-05	949	31	116.49	2.68138	0.199987	3.9e-05
21.820	1600	0	0.003429	6.9e-05	938	28	115.58	2.38494	0.199777	3.5e-05
25.400	1600	0	0.0029	6.7e-05	909	27	112.988	2.37431	0.19948	4e-05
26.877	1600	0	0.002712	6.4e-05	944	29	116.049	2.5198	0.19931	4e-05
29.245	1600	0	0.002186	6.7e-05	968	35	118.129	3.0135	0.199059	5e-05
29.774	1600	0	0.001981	5.8e-05	953	31	116.846	2.66915	0.198989	4.6e-05
30.298	1600	0	0.001652	6.9e-05	895	33	111.767	2.89717	0.198948	6.3e-05
30.838	1600	0	0.001559	6.6e-05	912	34	113.268	2.96453	0.19885	6.2e-05
31.396	1600	0	0.001026	5.8e-05	964	37	117.773	3.19862	0.198767	7.1e-05
31.967	1600	0	0.000845	5.5e-05	876	28	110.07	2.48908	0.198759	7.4e-05
32.557	1600	0	0.000442	7.4e-05	914	44	113.431	3.84225	0.19859	0.00014
33.170	110	170	0.0006	0.0014	180	130	36.2152	16.5913	0.19806	0.00063
33.803	115	56	0	0	220.839	70.1877	41.8	8.7	0.1965	0.0015
34.457	172	87	0	0	292.682	96.3004	51	11	0.2011	0.0012
35.131	68	34	0	0	158.945	51.8422	33.1	7.1	0.1966	0.002
38.940	1.4	1.6	0	0	19.0621	18.6288	7.3	4.6	0.203	0.033

Table A.10: $\rho = 0.250$ g/cm^3

T	σ_1	$\sigma_{1,err}$	a_2	$a_{2,err}$	$\xi_\parallel$	$\xi_{\parallel,err}$	$\xi_\perp$	$\xi_{\perp,err}$	q_0	$q_{0,err}$
27.199	12600	3100	0.035	0.0026	694	41	93.4103	3.82414	0.199138	3.1e-05
27.241	12500	2800	0.0348	0.0024	691	38	93.1028	3.56965	0.199129	2.9e-05
27.302	16300	3800	0.0315	0.0026	734	47	97.1009	4.3985	0.199112	3e-05
27.394	16500	3900	0.0311	0.0026	744	48	98.0957	4.41257	0.19906	3e-05
28.265	16000	3500	0.0284	0.0023	733	46	97.0806	4.23493	0.198901	2.9e-05
29.264	14200	3000	0.0251	0.0021	708	44	94.6652	4.15428	0.198725	2.9e-05
29.800	11100	2300	0.0254	0.0019	674	38	91.4698	3.60295	0.198619	2.9e-05
30.318	18700	5400	0.0163	0.0027	730	77	96.7959	7.08151	0.198681	3.9e-05
30.791	19500	7000	0.0131	0.0029	760	100	99.4213	9.23537	0.198615	4.5e-05
31.281	11600	3300	0.014	0.0024	624	64	86.556	6.23916	0.198437	4.4e-05
31.792	12400	4700	0.0082	0.0026	624	96	86.5608	9.26613	0.198216	5e-05
32.326	10000	18000	0.002	0.01	510	460	75.59	42.7202	0.19784	0.00012
32.887	4000	5800	0	0.0077	330	230	54.9751	25.249	0.1977	0.00034
33.471	3440	620	0	0	300.779	34.3594	51.9	3.9	0.19682	0.00042
34.084	1570	330	0	0	206.111	28.0237	39.8	3.5	0.19676	0.00067
34.724	920	230	0	0	158.007	26.5908	33.1	3.5	0.19447	0.001
35.396	590	130	0	0	136.538	20.1908	29.6	3	0.1986	0.001
36.099	308	100	0	0	92.1367	21.684	22.6	3.4	0.194	0.0021
36.832	249	100	0	0	93.387	25.4175	22.6	4.2	0.1993	0.0026
37.599	69	34	0	0	45.4897	15.8888	13.5	3.3	0.2041	0.0064
38.398	43	47	0	0	59.0831	48.5967	16.3	8.7	0.201	0.011

Table A.11: $\rho = 0.295$ g/cm^3

T	σ_1	$\sigma_{1,err}$	a_2	$a_{2,err}$	$\xi_\parallel$	$\xi_{\parallel,err}$	$\xi_\perp$	$\xi_{\perp,err}$	q_0	$q_{0,err}$
24.968	7500	0	0.0812	0.0019	430	12	66.5975	1.26546	0.198426	6.3e-05
25.898	7500	0	0.0752	0.0017	421	11	65.5953	1.17828	0.198386	6.2e-05
26.409	7500	0	0.0752	0.0018	396	11	62.7484	1.26881	0.198259	6.8e-05
26.930	7500	0	0.0696	0.0018	409	12	64.2314	1.33529	0.198201	7.5e-05
26.924	7500	0	0.0682	0.0015	425	11	66.0387	1.17151	0.198268	5.9e-05
27.433	7500	0	0.0641	0.0015	401	10	63.2944	1.16709	0.198121	6.8e-05
27.879	7500	0	0.0584	0.0016	415	12	64.9256	1.30053	0.198178	7.5e-05
28.361	7500	0	0.0551	0.0015	401	11	63.37	1.20236	0.19806	7.6e-05
28.827	7500	0	0.049	0.0013	373.2	9.6	60.2135	1.08789	0.197979	8e-05
29.204	7500	0	0.0449	0.0014	397	12	62.9398	1.29971	0.197885	8.6e-05
29.634	7500	0	0.0373	0.0012	375	9.6	60.416	1.08909	0.19781	8.6e-05
29.986	7500	0	0.0331	0.0011	379	9.9	60.8728	1.11778	0.197827	9e-05
30.568	7500	0	0.0255	0.0014	347	10	57.2361	1.11388	0.19766	0.00013
30.918	7500	0	0.0174	0.0012	346	9.3	57.0706	1.08275	0.19766	0.00014
31.433	7500	0	0.0106	0.0015	336.5	9.9	55.9546	1.16481	0.19711	0.00023
31.971	7500	0	0	0.0017	331	11	55.2987	1.30668	0.19631	0.00038
32.523	5240	740	0	0	270	24	47.8926	2.9716	0.19687	0.00038
33.965	1890	560	0	0	169	31	34.3893	4.34465	0.1927	0.0013

Appendix B

Powder Averaging

B.1 Powder Average

B.1.1 Intrinsic Line Shapes

There are several possibilities for the intrinsic X-ray line shape arising from the density modulation of a smectic phase. For single-Lorentzian-like line shapes, we will consider here four distinct line shapes which frequently appear in the literature. Note that they all tend to behave like a single Lorentzian in certain limits.

(i) The simplest is the isotropic Lorentzian line shape:

$$S(\mathbf{q}) \propto \frac{1}{1+\xi^2(\mathbf{q}-\mathbf{q}_0)^2} \tag{B.1}$$

(ii) When anisotropic correlation lengths, $\xi_{\|}$ and $\xi_{\perp}$, are involved, an anisotropic Lorentzian is used:

$$S(\mathbf{q}) \propto \frac{1}{1+\xi_{\|}^2(q_{\|}-q_0)^2+\xi_{\perp}^2 q_{\perp}^2} \tag{B.2}$$

(iii) In reality, X-ray smectic fluctuation peaks are better described by an anisotropic Lorentzian with a 4th order correction in the transverse direction (LFC) [46]:

$$S(\mathbf{q}) \propto \frac{1}{1+\xi_{\|}^2(q_{\|}-q_0)^2+\xi_{\perp}^2 q_{\perp}^2+c\xi_{\perp}^4 q_{\perp}^4} \tag{B.3}$$

(iv) Finally an anisotropic Lorentzian raised to the power $1 - \eta_\perp/2$ along the transverse direction (LPC) has been equally useful to describe X-ray smectic peaks [46]:

$$S(\mathbf{q}) \propto \frac{1}{\xi_\parallel^2 (q_\parallel - q_0)^2 + (1 + \xi_\perp^2 q_\perp^2)^{1-\eta_\perp/2}} \tag{B.4}$$

When random fields affect the scattering structure factor, the square of the above line shapes must be considered.

B.1.2 Exact Calculation

Powder averaging is equivalent to having $\mathbf{q}_0$ rotate freely and equivalently to all directions. Therefore,

$$S_{powder}(\mathbf{q}) \propto \sum_{\mathbf{q}_0} S(\mathbf{q}), \tag{B.5}$$

or

$$S_{powder}(\mathbf{q}) \propto \int d\Omega \; S(\mathbf{q}), \tag{B.6}$$

where $S(\mathbf{q})$ is one of those intrinsic line shapes previously given.

Powder averaging the isotropic Lorentzian is, therefore,

$$\begin{aligned} S_{powder}(\mathbf{q}) &\propto \int d\Omega \, \frac{1}{1 + \xi^2 (\mathbf{q} - \mathbf{q}_0)^2} \\ &= \int_{-1}^{1} d\cos\theta \frac{2\pi}{1 + \xi^2 q^2 + \xi^2 q_0^2 - 2\xi^2 q_0 q \cos\theta} \\ &= \frac{\pi}{\xi^2 q_0 q} \ln \left| \frac{1 + \xi^2 (q + q_0)^2}{1 + \xi^2 (q - q_0)^2} \right| . \end{aligned} \tag{B.7}$$

In the limit of $\mathbf{q} \to 0$, the above result becomes

$$S_{powder}(\mathbf{q} \to 0) = \frac{4\pi}{1 + \xi^2 q_0^2} \tag{B.8}$$

as expected. Also note that for this isotropic Lorentzian, $S_{powder}(\mathbf{q} \to \infty) = 0$.

Powder averaging the anisotropic Lorentzian requires a little more calculation.

Starting from the powder averaging equation (Eqn. B.6),

$$\begin{aligned}
S_{powder}(\mathbf{q}) &\propto \int d\Omega \, \frac{1}{1+\xi_{\parallel}^2(q_{\parallel}-q_0)^2+\xi_{\perp}^2 q_{\perp}^2} \\
&= \int_{-1}^{1} d\cos\theta \frac{2\pi}{1+\xi_{\parallel}^2(q\cos\theta-q_0)^2+\xi_{\perp}^2 q^2\sin^2\theta} \\
&= \int_{-1}^{1} d\mu \frac{2\pi}{A+2B\mu+C\mu^2} \qquad \text{(B.9)}
\end{aligned}$$

where

$$\begin{aligned}
A &= 1+\xi_{\parallel}^2 q_0^2+\xi_{\perp}^2 q^2 \\
B &= -\xi_{\parallel}^2 q_0 q \qquad \text{(B.10)} \\
C &= (\xi_{\parallel}^2-\xi_{\perp}^2)q^2 .
\end{aligned}$$

Let us define

$$\begin{aligned}
D &\equiv B^2-AC \\
&= q^2\left[\xi_{\perp}^2(\xi_{\perp}^2-\xi_{\parallel}^2)q^2+\xi_{\perp}^2\xi_{\parallel}^2 q_0^2+\xi_{\perp}^2-\xi_{\parallel}^2\right] \qquad \text{(B.11)}
\end{aligned}$$

and we know the following indefinite integral

$$\begin{aligned}
&\int d\mu \frac{1}{A+2B\mu+C\mu^2} \\
&= \begin{cases} \frac{1}{\sqrt{|D|}}\tan^{-1}\frac{C\mu+B}{\sqrt{|D|}} & \text{if } D<0 \\ -\frac{1}{C\mu+B} & \text{if } D=0 \\ \frac{1}{2\sqrt{D}}\ln\left|\frac{C\mu+B-\sqrt{D}}{C\mu+B+\sqrt{D}}\right| & \text{if } D>0. \end{cases} \qquad \text{(B.12)}
\end{aligned}$$

Therefore, when $D<0$,

$$\begin{aligned}
S_{powder}(\mathbf{q}) &\propto \left[\frac{2\pi}{\sqrt{|D|}}\tan^{-1}\frac{C\mu+B}{\sqrt{|D|}}\right]_{-1}^{1} \\
&= \frac{2\pi}{\sqrt{|D|}}\left\{\tan^{-1}\frac{B+C}{\sqrt{|D|}}-\tan^{-1}\frac{B-C}{\sqrt{|D|}}\right\}. \qquad \text{(B.13)}
\end{aligned}$$

When $D = 0$,

$$S_{powder}(\mathbf{q}) \propto \left[-\frac{2\pi}{C\mu + B}\right]_{-1}^{1} = \frac{4\pi}{A - C}, \tag{B.14}$$

and when $D > 0$,

$$\begin{aligned} S_{powder}(\mathbf{q}) &\propto \left[\frac{\pi}{\sqrt{D}} \ln \left|\frac{C\mu + B - \sqrt{D}}{C\mu + B + \sqrt{D}}\right|\right]_{-1}^{1} \\ &= \frac{\pi}{\sqrt{D}} \ln \left|\frac{A - C + 2\sqrt{D}}{A - C - 2\sqrt{D}}\right|. \end{aligned} \tag{B.15}$$

Note that $\lim_{D\to 0+} S(\mathbf{q}) = \lim_{D \to 0-} S(\mathbf{q}) = S(\mathbf{q})|_{D=0}$. Also it is important to note that as $\xi_\perp \to \xi_\|$, the above result becomes that of the isotropic Lorentzian.

$$\begin{aligned} C &\to 0 \\ D &\to B^2 > 0 \\ S_{powder}(\mathbf{q}) &\to \frac{\pi}{|B|} \ln \left|\frac{A + 2|B|}{A - 2|B|}\right|, \end{aligned} \tag{B.16}$$

which is the same as Eqn. B.7. Its behavior is similar to that of the powder average of the isotropic Lorentzian, i.e., as $\mathbf{q} \to 0$, $B, C, D \to 0$, and we have

$$S_{powder}(\mathbf{q} \to 0) = \frac{4\pi}{1 + \xi^2 q_0^2}, \tag{B.17}$$

and as $\mathbf{q} \to \infty$, $D \to -\infty$ and $S_{powder}(\mathbf{q}) \to 0$, just the same as before.

Though it is possible to calculate the powder average of the LFC line shape analytically, the solution is prohibitively complex to present here in a closed form. For the LPC line shape, it appears to be impossible to deduce an analytic form for the powder average. For such complex line shapes, certain approximations are necessary unless we are seeking a numerical solution.

A Lorentzian-squared line shape is, however, still manageable analytically.

$$S_{powder}(\mathbf{q}) \propto \int d\Omega \, \frac{1}{(1 + \xi^2(\mathbf{q} - \mathbf{q}_0)^2)^2}$$

$$
\begin{aligned}
&= \int_{-1}^{1} d\mu \, \frac{2\pi}{(1+\xi^2 q^2+\xi^2 q_0^2-2\xi^2 q_0 q\mu)^2} \\
&= \frac{2\pi}{2\xi^2 q q_0}\left[\frac{1}{1+\xi^2 q^2+\xi^2 q_0^2-2\xi^2 q q_0 \mu}\right]_{-1}^{1} \\
&= \frac{4\pi}{\{1+\xi^2(q-q_0)^2\}\{1+\xi^2(q+q_0)^2\}}. \qquad \text{(B.18)}
\end{aligned}
$$

Even the anisotropic-Lorentzian-squared is solvable analytically.

$$
\begin{aligned}
S_{powder}(\mathbf{q}) &\propto \int d\Omega \, \frac{1}{\left\{1+\xi_{\|}^2(q_{\|}-q_0)^2+\xi_{\perp}^2 q_{\perp}^2\right\}^2} \\
&= \int_{-1}^{1} d\cos\theta \, \frac{2\pi}{\left\{1+\xi_{\|}^2(q\cos\theta-q_0)^2+\xi_{\perp}^2 q^2\sin^2\theta\right\}^2} \\
&= \int_{-1}^{1} d\mu \, \frac{2\pi}{(A+2B\mu+C\mu^2)^2} \\
&= 2\pi\left[-\frac{C\mu+B}{2DR}-\frac{C}{2D}\int d\mu \frac{1}{R}\right]_{-1}^{1}, \qquad \text{(B.19)}
\end{aligned}
$$

where $R = A + 2B\mu + C\mu^2$ and A, B, C, and D are defined previously.

When it comes to the LFC, the integration becomes a little more complex:

$$
\begin{aligned}
S_{powder}(\mathbf{q}) &\propto \int d\Omega \, \frac{1}{\left\{1+\xi_{\|}^2(q_{\|}-q_0)^2+\xi_{\perp}^2 q_{\perp}^2+c\xi_{\perp}^4 q_{\perp}^4\right\}} \\
&= \int_{-1}^{1} d\cos\theta \, \frac{2\pi}{\left\{1+\xi_{\|}^2(q\cos\theta-q_0)^2+\xi_{\perp}^2 q^2\sin^2\theta+c\xi_{\perp}^4 q^4\sin^4\theta\right\}} \\
&= \int_{-1}^{1} d\mu \, \frac{2\pi}{(A'+2B\mu+C'\mu^2+D'\mu^4)}, \qquad \text{(B.20)}
\end{aligned}
$$

where

$$
\begin{aligned}
A' &= A + c\xi_{\perp}^4 q^4 = 1 + \xi_{\|}^2 q_0^2 + \xi_{\perp}^2 q^2 + c\xi_{\perp}^4 q^4 \\
C' &= C - 2c\xi_{\perp}^4 q^4 = (\xi_{\|}^2 - \xi_{\perp}^2) q^2 - 2c\xi_{\perp}^4 q^4 \\
D' &= c\xi_{\perp}^4 q^4. \qquad \text{(B.21)}
\end{aligned}
$$

The above integration on the right hand side can be also written as

$$\int_{-1}^{1} d\mu \, \frac{2\pi}{D'(\mu-\alpha_1)(\mu-\alpha_2)(\mu-\alpha_3)(\mu-\alpha_4)}, \tag{B.22}$$

where α_i are the roots for the following quartic equation:

$$A' + 2B\mu + C'\mu^2 + D'\mu^4 = 0. \tag{B.23}$$

By expanding the integrand, it becomes

$$\int_{-1}^{1} d\mu \, \frac{2\pi}{D'} \sum_{ij} C_{ij} \frac{1}{(\mu-\alpha_i)^j}, \tag{B.24}$$

where coefficients C_{ij} can be obtained through expansion process. The integration can be performed analytically at this stage. We have calculated the powder average of the LFC using this method.

B.1.3 Approximate Calculation

One very popular approximation method is to treat the spherical surface generated by freely rotating $\mathbf{q}_0$ as an infinite plane. This is a good approximation when $|q-q_0| \ll q_0$ and the intrinsic line shape falls very fast at large $|\mathbf{q}-\mathbf{q}_0|$. In that case, we can write

$$\begin{aligned} S_{powder}(\mathbf{q}) &\propto \int d\Omega \; S(\mathbf{q}) \\ &= \int \frac{dA_{\mathbf{q}_0\ sphere}}{q_0^2} S(\mathbf{q}) \\ &\approx \int \frac{dA_{plane}}{q_0^2} S(\mathbf{q}). \end{aligned} \tag{B.25}$$

Obviously this approximation does not work for the isotropic or the anisotropic Lorentzian because the line shapes decay too slowly as q increases, i.e, the integration diverges.

As an example, we will provide an approximate powder average of an anisotropic Lorentzian squared.

$$
\begin{aligned}
S(\mathbf{q}) &\propto \int \frac{d\mathbf{q}_{\perp}}{\left(1+\xi_{\|}^{2}(q_{\|}-q_{0})^{2}+\xi_{\perp}^{2}q_{\perp}^{2}\right)^{2}} \\
&= \int \frac{dq_{\perp,x}dq_{\perp,y}}{\left(1+\xi_{\|}^{2}(q_{\|}-q_{0})^{2}+\xi_{\perp}^{2}q_{\perp,x}^{2}+\xi_{\perp}^{2}q_{\perp,y}^{2}\right)^{2}} \\
&= \int_{0}^{\infty} \frac{dq_{\perp,x}}{\left(1+\xi_{\|}^{2}(q_{\|}-q_{0})^{2}+\xi_{\perp}^{2}q_{\perp,x}^{2}\right)^{2}} \int_{0}^{\infty} \frac{dq_{\perp,y}}{\left(1+\frac{\xi_{\perp}^{2}q_{\perp,y}^{2}}{\left(1+\xi_{\|}^{2}(q_{\|}-q_{0})^{2}+\xi_{\perp}^{2}q_{\perp,x}^{2}\right)}\right)^{2}} \\
&= \frac{\pi}{4\xi_{\perp}} \int_{0}^{\infty} \frac{dq_{\perp,x}}{\left(1+\xi_{\|}^{2}(q_{\|}-q_{0})^{2}+\xi_{\perp}^{2}q_{\perp,x}^{2}\right)^{\frac{3}{2}}} \\
&= \frac{\pi}{4\xi_{\perp}\left(1+\xi_{\|}^{2}(q_{\|}-q_{0})^{2}\right)^{\frac{3}{2}}} \int_{0}^{\infty} \frac{dq_{\perp,x}}{\left(1+\frac{\xi_{\perp}^{2}q_{\perp,x}^{2}}{1+\xi_{\|}^{2}(q_{\|}-q_{0})^{2}}\right)^{\frac{3}{2}}} \\
&= \frac{\pi}{4\xi_{\perp}^{2}\left(1+\xi_{\|}^{2}(q_{\|}-q_{0})^{2}\right)}
\end{aligned}
\tag{B.26}
$$

It is obvious that in this approximate scheme (integration over cartesian coordinates) powder averaging over one dimension reduces the exponent of a Lorentzian by a factor of two, thus a Lorentzian squared line shape becomes a Lorentzian under powder averaging over a plane.

Bibliography

[1] S. Fishman and A. Aharony, J. Phys. C **12**, L729 (1979).

[2] T. Bellini *et al.*, Phys. Rev. Lett. **69**, 788 (1992).

[3] N. A. Clark *et al.*, Phys. Rev. Lett. **71**, 3505 (1993).

[4] L. Wu *et al.*, Phys. Rev. E **51**, 2157 (1995).

[5] T. Bellini, N. A. Clark, and D. W. Schaefer, Phys. Rev. Lett. **74**, 2740 (1995).

[6] H. Zeng, B. Zalar, G. S. Iannacchione, and D. Finotello, Phys. Rev. E **60**, 5607 (1999).

[7] T. Bellini, L. Radzihovsky, J. Toner, and N. A. Clark (unpublished).

[8] B. Zhou, G. S. Iannacchione, and C. W. Garland, Phys. Rev. E **55**, 2962 (1977).

[9] H. Haga and C. W. Garland, Phys. Rev. E **56**, 3044 (1997).

[10] H. Haga and C. W. Garland, Liquid Crystals **23**, 645 (1997).

[11] G. S. Iannacchione, C. W. Garland, J. T. Mang, and T. P. Rieker, Phys. Rev. E **58**, 5966 (1988).

[12] T. Bellini, N. A. Clark, F. Mantegazza, and G. Natale, Phys. Rev. E **57**, 2996 (1988).

[13] F. Mercuri, A. K. Gosh, and M. Marinelli, Phys. Rev. E **60**, R6309 (1999).

[14] T. Jin and D. Finotello, Phys. Rev. Lett. **86**, 818 (2001).

[15] A. Hourri, T. K. Bose, and J. Thoen, Phys. Rev. E **63**, 051702 (2001).

[16] P. G. de Gennes and J. Prost, *The Physics of Liquid Crystals* (Oxford, New York, 1993).

[17] S. S. Kistler, J. Phys. Chem. **34**, 52 (1932).

[18] http://eande.lbl.gov/ECS/Aerogels/satoc.htm, Lawrence Berkeley National Laboratory.

[19] D. W. Schaefer and K. D. Keefer, Phys. Rev. Lett. **56**, 2199 (1986).

[20] R. Vacher, T. Woignier, J. Pelous, and E. Courtens, Phys. Rev. B **37**, 6500 (1988).

[21] F. Ferri, B. J. Frisken, and D. S. Cannell, Phys. Rev. Lett. **67**, 3626 (1991).

[22] A. Emmerling and J. Fricke, J. Non-Cryst. Solds **145**, 113 (1992).

[23] D. W. Schaefer, Mat. Res. Soc. Bull. **14-4**, 49 (1994).

[24] B. Jerome, Rep. Prog. Phys. **54**, 391 (1991).

[25] B. E. Warren, *X-ray Diffraction* (Dover, New York, 1990).

[26] J. D. Jackson, *Classical Electrodynamics*, 2 ed. (Wiley, New York, 1975).

[27] J. J. Sakurai, *Modern Quantum Mechanics* (Addison-Wesley, Reading, Massachusetts, 1994).

[28] A. Rappaport, Ph.D. thesis, University of Colorado, 1995.

[29] C. W. Garland and G. Nounesis, Phys. Rev. E **49**, 2964 (1994).

[30] L. Radzihovsky and J. Toner, Phys. Rev. B **60**, 206 (1999).

[31] W. L. McMillan, Phys. Rev. A **7**, 1419 (1973).

[32] B. R. Patton and B. S. Andereck, Phys. Rev. Lett. **69**, 1556 (1992).

[33] B. S. Andereck and B. R. Patton, Phys. Rev. E **49**, 1393 (1994).

[34] P. H. Keyes, private communication.

[35] L. Onsager, Phys. Rev. **65**, 117 (1944).

[36] Y. Imry and S.-K. Ma, Phys. Rev. Lett. **35**, 1399 (1975).

[37] T. Nattermann and J. Villain, Phase Transitions **11**, 5 (1988).

[38] J. Z. Imbrie, Phys. Rev. Lett. **53**, 1747 (1984).

[39] K. Huang, *Statistical Mechanics*, 2 ed. (Wiley, New York, 1987).

[40] M. Aizenman and J. Wehr, Phys. Rev. Lett. **62**, 2503 (1989).

[41] D. S. Fisher, Phys. Rev. Lett. **78**, 1964 (1997).

[42] L. Radzihovsky and J. Toner, Phys. Rev. Lett. **78**, 4414 (1997).

[43] L. Radzihovsky and J. Toner, Phys. Rev. Lett. **79**, 4214 (1997).

[44] M. Benzekri, J. P. Marcerou, H. T. Nguyen, and J. C. Rouillon, Phys. Rev. B **41**, 9032 (1990).

[45] Degussa Corp, Silica Division, 65 Challenger Road, Ridgefield Park, NJ 07660. Technical data and properties can be found in the manufacturer's booklet AEROSILS.

[46] B. M. Ocko, Ph.D. thesis, Massachusetts Institute of Technology, 1984.

[47] E. D. Specht, Ph.D. thesis, Massachusetts Institute of Technology, 1987.

[48] R. Pynn, Los Alamos Science **19**, (1990).

[49] B. M. Ocko, private communication.

[50] J. Als-Nielsen *et al.*, Phys. Rev. Lett. **39**, 352 (1977).

[51] H. Yosizawa *et al.*, Phys. Rev. Lett. **48**, 438 (1982).

[52] R. A. Cowley *et al.*, Phys. Rev. B **30**, 6650 (1984).

[53] R. J. Birgeneau, R. A. Cowley, G. Shirane, and H. Yoshizawa, J. Stat. Phys. **34**, 817 (1984).

[54] R. J. Birgeneau *et al.*, Physica **137B**, 83 (1986).

[55] R. A. Cowley *et al.*, Z. Phys. B – Condensed Matter **75**, 303 (1989).

[56] R. A. Pelcovits and A. Aharony, Phys. Rev. B **31**, 350 (1985).

[57] G. Grinstein, S.-K. Ma, and G. F. Mazenko, Phys. Rev. B **15**, 258 (1977).

[58] P. Andelmann and J. F. Joanny, in *Scaling Phenomena in Disordered Systems*, edited by R. Pynn and A. Skjeltorp (Plenum Publishing, unknown, 1985).

[59] Safinya, Ph.D. thesis, Massachusetts Institute of Technology, unknown.

[60] S. Qian, G. S. Iannacchione, and D. Finotello, Phys. Rev. E **57**, 4305 (1998).

[61] G. S. Iannacchione, private communication.

[62] M. J. P. Gingras and D. A. Huse, Phys. Rev. B **53**, 15 193 (1996).

[63] K. K. Chan *et al.*, Phys. Rev. Lett. **54**, 920 (1985).